UNIVERSIDADE DE LISBOA

FACULDADE DE CIÊNCIAS

DEPARTAMENTO DE ENGENHARIA GEOGRÁFICA, GEOFÍSICA E ENERGIA

Atmospheric circulation over Southern Africa and its relationship with regional rainfall

Carlos Afonso Jacob Carlota da Rosa Pereira

Mestrado em Ciências Geofísicas

Especialização em Meteorologia e Oceanografia

Dissertação orientada por:

Doutor Alexandre Miguel Ramos

Doutor João Paulo Martins

2022

Acknowledgments

First, I would like to thank my supervisors, Alexandre Ramos and João Martins, for all the help, advice, discussions and suggestions they gave me along this incredible journey of building my very first thesis. A special thanks to all my colleges from IPMA and FRESAN project, which allowed me to have one of the biggest experiences of my life in southern Angola, leaving me completely in love with the region, its culture, and its people. *Twapandula!* (means "thank you" in Umbundo, a dialect widely spoken in Angola). I would also like to thank my group of high school and college friends who always supported me and cared about the stuff I was doing. Now, a particular thanks to my little dog, who made my days less empty while I was writing.

Por fim, agradeço à minha família todo o apoio que me deram ao longo do meu percurso académico. Sem a ajuda da minha mãe Isabel, do Luís, do avô Henrique e da avó Mária, nada disto teria sido possível. Dedico este trabalho à Pipinha e ao meu pai, que, onde quer que esteja, sei que estará orgulhoso.

This work was developed on the scope of FRESAN project - FED/2017/389-710, financed by the European Union and managed by Camões I.P.

Abstract

Throughout the last decades, southern Africa has become increasingly vulnerable to weather variability, which affects moisture advection and convergence in the lower levels of the atmosphere and impact local rainfall, essential for rudimentary rainfed agricultural systems, in which most of countries' economies rely on. Thus, understanding atmospheric circulation dynamics is crucial, as well as the identification of humidity sources and advection mechanisms that control precipitation across the region. Using ERA5 reanalysis (1980-2020) and 10 weather stations' data (2014-2020), synoptical and climatological analysis over the region were performed, namely regarding atmospheric moisture circulation and geopotential height and rainfall anomalies. Recent literature identifies the Angola Low (AL) and the Mozambique Channel Trough (MCT) as two main summertime low-pressure systems responsible for converting humidity into rainfall. The Zambezi and Limpopo river-valley' associated low-level jets (ZRV LLJ and LRV LLJ) have been identified as major gateways transporting Indian Ocean moisture into central and SW Africa. Both LLJs are controlled by MCT and AL intensities, often conjugated within the same phase (both weak or both strong). Results showed these conjugations of MCT and AL intensities had a higher control on ZRV LLJ than on LRV LLJ, with weaker (stronger) MCT and AL being associated with a stronger (weaker) ZRV LLJ, thus promoting increases (decreases) of rainfalls over SW Africa. At a larger scale, it was shown that El-Niño (La-Niña) phases of ENSO were linked with northward (southward) shifts of the AL system and with decreases (increases) of precipitations across the subcontinent, regardless of SIOD (Subtropical Indian Ocean Dipole) phase. SW Africa region lies in a *border-zone* of weak and non-significant rainfall anomalies. An analysis of two exceptional rainy seasons showed that during the analysed events, large-scale variability and unusual circulation features could have overlapped its influence over both the AL and MCT systems.

Key words: Low-Level Jet; moisture advection; Southern Africa; Angola Low; Mozambique Channel Trough

Resumo alargado

Ao longo das últimas décadas, o sul de África tem experienciado um significativo aumento da sua vulnerabilidade à variabilidade atmosférica da região, na medida em que esta última influencia, direta ou indiretamente, a advecção e a convergência de humidade nos níveis mais baixos da atmosfera, provocando o aumento ou diminuição da quantidade de precipitação nestes locais. De facto, a variável meteorológica de maior importância para o sul de África é a precipitação, visto que as economias e a sociedade dos países aí localizados dependem fortemente de uma agricultura de cariz maioritariamente rudimentar e, por isso, muito dependente da água que provém da chuva. No entanto, as projeções climáticas mais recentes para as próximas décadas apontam para uma diminuição significativa da quantidade de precipitação em grande parte do subcontinente, essencialmente nas regiões do Sudoeste (SW Africano), ou seja, Angola e Namíbia, temendo-se, futuramente, consequências socioeconómicas e humanitárias muito severas. Deste modo, torna-se muito relevante compreender a circulação atmosférica da região, bem como identificar as fontes e mecanismos de transporte de humidade até às áreas de maior vulnerabilidade do sul de África. A literatura científica mais recente indica que durante o verão austral ocorrem dois sistemas de baixa-pressão que dominam estas regiões e são responsáveis por grande parte da conversão de humidade em precipitação: a Depressão de Angola (*Angola Low* ou AL) e um sistema ciclónico no Canal de Moçambique (*Mozambique Channel Trough* ou MCT). Durante esta época do ano, formam-se jatos nos níveis baixos da atmosfera (*Low-Level Jets* ou LLJs) nos vales dos rios Zambezi e Limpopo, servindo como "portas de entrada" à humidade proveniente do Oceano Índico, em direção às regiões centrais e ocidentais do subcontinente. A advecção de humidade por meio destes LLJs, em direção a oeste, é forçada pela circulação atmosférica em torno de um sistema de altas pressões (HP) localizado na região sul do Oceano Índico, denominado por Mascarene HP (ou anticiclone do Índico Sul). No entanto, a presença de uma barreira orográfica importante como é o caso da ilha de Madagáscar, afeta o transporte de humidade até à região dos vales dos rios Limpopo e Zambezi, induzindo variabilidade nos escoamentos associados aos respetivos LLJs. O ajustamento dinâmico deste fluxo (predominantemente de leste) à topografia de Madagáscar, induz uma circulação ciclónica na região do Canal de Moçambique (MC) – o denominado MCT. A humidade advectada até ao SW Africano colide com fluxos de humidade provenientes do Atlântico Sul que, conjuntamente com forçadores orográficos na região do interior de Angola e Namíbia, alimentam um sistema de baixas pressões, essencialmente de origem térmica, que se formam na zona de fronteira entre estes dois países. A convergência de humidade proveniente (maioritariamente) de ambos os oceanos (Índico e Atlântico), alimenta este sistema, que adquire características tropicais e se passa a denominar por AL. O sistema mantém-se quase-estacionário na região devido à orografia do SW de África, na medida em que as cadeias montanhosas existentes ao longo da costa e no interior destes países, promovem escoamentos anabáticos que, por consequência, alimentam processos de convecção profunda, alimentando e fortalecendo a AL. Em conjunto, a AL e o MCT originam uma banda de nuvens (denominada por *Tropical Temperate Troughs*, ou TTTs), com orientação NW-SE (i.e., desde a região do sul de Angola até ao MC), responsável pela maioria das chuvas estivais do subcontinente sul Africano. Muitas das TTTs (incluindo o MCT), são alimentados pelas águas quentes do MC, em particular devido ao calor latente libertado pelas correntes oceânicas aí existentes (como é o caso da Corrente das Agulhas).

O principal objetivo desta tese foi, essencialmente, analisar os mecanismos de transporte e fontes de vapor de água em direção à região do SW Africano, identificando as possíveis causas de variabilidade (a diversas escalas) da precipitação da região e verificando padrões atmosféricos que contribuem para períodos mais secos ou mais húmidos nesses locais. Deste modo, foram utilizados dados meteorológicos mensais da mais recente reanálise do Centro Europeu de Previsão do Tempo a Curto e Médio Prazo (ECMWF), para o período entre 1980 e 2020. Foram também analisados dados de precipitação provenientes de 10 estações meteorológicas espalhadas pelas regiões do sul de Angola e norte da

Namíbia. Estas últimas, relativas ao período 2014-2020. Análises sinóticas e climatológicas à circulação de humidade na atmosfera permitiram identificar o Oceano Índico como principal fonte de humidade para o subcontinente sul-Africano, resultado confirmado pela prevalência de dias chuvosos (secos), na região do SW Africano, quando os ventos sopram maioritariamente de leste (oeste). Na verdade, são os LLJ do Zambezi e do Limpopo que permitem uma significativa advecção de vapor de água desde o Oceano Índico até ao sul de África, sendo a intensidade do transporte controlada pela AL e pelo MCT. Os resultados mostram que existe uma tendência para que a AL e o MCT se conjuguem em fases idênticas, i.e., quando um sistema se apresenta com intensidades menores (mais fraco), o outro também, e vice-versa. Esta situação tem implicações consideráveis nas chuvas da região. Foi verificado que conjugações de AL forte (fraca) e MCT forte (fraco) se relacionam com valores de precipitação abaixo (acima) do normal. Os resultados mostraram também que estas combinações de intensidades entre a AL e o MCT afetam mais expressivamente a intensidade do LLJ do Zambezi do que do Limpopo, com AL forte (fraca) AL e MCT forte (fraco) associados a um Zambezi LLJ fraco (forte) e, consequentemente, escassez (abundância) de precipitação na região do SW Africano.

Os impactos de dois importantes modos de variabilidade de larga-escala - o *El-Niño Southern Oscillation* (ENSO) e o *Subtropical Indian Ocean Dipole* (SIOD) - na precipitação interanual regional, foram também analisados, na medida em que ambos os modos se associam a flutuações nas temperaturas da superfície do oceano (em especial na região do MC) e também, a oscilações nos valores de altura do geopotencial em toda a região do sul de África. Verificou-se, assim, que meses de El-Niño (La-Niña) se associam não só a diminuições (aumentos) de precipitação sobre o subcontinente sul-Africano, como também a desvios meridionais da AL em direção a norte (sul), acompanhados por diminuições (aumentos) de intensidade deste mesmo sistema, independentemente da fase do SIOD. Sobre a região de interesse (SW de África), a influência de ambos os modos de variabilidade nas anomalias de precipitação verificou-se pouco significativa. No entanto, é preciso ter em conta que, em todas as conjugações analisadas (entre ambas as fases do SIOD e do ENSO), o território em estudo localizou-se numa "zona de fronteira" entre anomalias negativas e positivas de precipitação, associadas a um fraco sinal estatístico. Ainda assim, mesmo com fraca significância estatística, os resultados indicaram que SIOD positivos associados a meses de La-Niña apresentam um padrão de precipitação acima do normal para as regiões do SW Africano. Uma análise a dois casos de estudo de eventos extremos de precipitação (um muito chuvoso e o outro, muito seco), permitiu concluir que, nestes casos, a variabilidade de larga escala exerceu um forte domínio na intensidade e dinâmicas dos sistemas sinóticos que ocorreram sobre o subcontinente (nomeadamente a AL e o MCT), não se descartando, de igual forma, a considerável ação de circulações de cariz local que surgiram na região (e.g., o ciclone Idai), perturbando significativamente a advecção de humidade em direção à região de interesse e, consequentemente, a precipitação sobre estes locais.

Por fim, discutiu-se o impacto que a falta de instrumentos meteorológicos *in situ* na região do sul de África, em particular no SW Africano, nomeadamente no que concerne à inexistência de séries temporais longas de diversos parâmetros físicos (precipitação, humidade, temperatura, entre outros…), o que tem contribuído para um maior desconhecimento científico sobre a dinâmica da atmosfera nestes locais. Desta forma, torna-se da maior relevância investir em instrumentos científicos (como estações meteorológicas) ou em campanhas de recolha de dados (como por exemplo, estudar perfis atmosféricos). É também crucial, num contexto de aumento da temperatura média global, compreenderem-se mudanças nos padrões de variabilidade de larga escala (ENSO e SIOD) e os seus respetivos impactos na precipitação do sul de África.

Palavras-chave: Jato de níveis baixos; advecção de humidade; sul de África; Depressão de Angola; Sistema ciclónico do Canal de Moçambique

Table of contents

1. Introduction 1

1.1. Main SW Africa weather dynamics 2

1.2. Low-level jet dynamics and its relationship with moisture transport 6

1.3. The Angola Low as a key feature to rainfall 8

2. Methodology 12

2.1. Weather stations data 12

2.2. ERA5 reanalysis data for the subcontinent 15

2.3. Searching methodology of local geopotential height minimums 16

2.4. Statistics used 18

2.5. Data and computation of large-scale indexes: ENSO and SIOD 18

3. Results and Discussion 20

3.1. Moisture transport towards the Southern African subcontinent 20

3.2. Impacts of Low-Level Jets from Limpopo and Zambezi river-valleys on regional rainfall . 23

3.3. The influence of the Angola Low and the Mozambique Channel Trough intensities, on precipitations across Southern Africa 29

3.4. Large-scale modes of variability and its relationship with regional rainfall 37

3.5. Case-studies over SW Africa 40

3.5.1. Rainy seasons with below-normal precipitation – the case of 2018/19 41

3.5.2. Rainy seasons with above-normal precipitation – the case of 2010/11 44

3.5.3. Influence of large-scale modes of variability on the exceptionality of case-studies 46

4. Conclusions 50

5. References 52

6. Appendix 58

6.1. Precipitation values of hydrological years since 1980/81 58

6.2. Geopotential height intensities: Mozambique Channel Trough vs. the Angola Low 59

6.3. Photographic records of FRESAN missions across southern Angola 59

List of Figures

Figure 1.1 – Spatial distribution of Köppen–Geiger climate subtypes over the African continent. Climate subtypes legend: Af – tropical rainforest; Am – tropical with monsoons; Aw – tropical savannah with dry winters; BWh – hot arid desert; BWk – cold arid desert; BSh – hot steppe desert; BSk – cold steppe desert; Csa – temperate with dry and hot summer; Csb – temperate with dry and warm summer; Cwa – temperate with dry winter and hot summer; Cwb – temperate with dry winter and warm summer; Cfa – temperate with hot summer but no dry season; Cfb – temperate with warm summer but no dry season. The dark square indicates the region of interest, i.e., southwestern Africa. Source: Peel et al. (2007). . 2
Figure 1.2 - Termopluviogram for Southern Angola and Northern Namibia using 1980-2020 monthly averaged data from ERA5 reanalysis. All monthly precipitation and temperature data used in this figure are average values over a box in SW Africa (southern Angola and northern Namibia), represented by the red box on the inset map and covering the area [13º-20ºS; 12º-18ºE] - the latter, indicates the region of interest. Boxplots represent the precipitation variability, for each month, over the 40 years of data. Inside the boxplots, blue stars represent the average precipitation value for that month and the blue line shows the median value. Circles outside boxplots display the outliers. The red line unifies the red dots, where each dot stands for the 1980-2020 average temperature value (over the red box) for each month. 3
Figure 1.3 - Maps of Southern African subcontinent showing 1980-2020 averaged seasonal data for geopotential height (black contours, interpolated across points spaced 0.75ºx0.75º) and wind (grey quivers spaced 1.5ºx1.5º), retrieved at 850[hPa] for the period of **(a)** dry season (April to October) and **(b)** rainy season (November to March). Within the isolines of equal geopotential height, the correspondent value is displayed. The length of the quivers is proportional to its magnitude. Based on Munday & Washington (2017), Barimalala et al. (2021) and Rapolaki (2020), thick black quivers represent the main routes of water vapour transport towards SW Africa, the dotted dark red line schematically illustrates the pattern of a typical austral mid-latitude Rossby wave (explored in the subsection 1.3, below), the dashed orange line defines de SIOCZ, and the dotted violet line defines the Angola-Benguela Front (ABF; see subsection 1.3). Green quivers indicate the location and main direction of both Zambezi and Limpopo LLJs (see subsection 1.2). Both figures for dry and rainy seasons display the main weather features' names (over the regions they usually develop), with HP meaning *high-pressure* and LLJ standing for *low-level jet* (see subsection 1.2, below). The production of this figure was also inspired by van Heerden & Taljaard (1998) work. 5
Figure 1.4 - Profiles of wind speed magnitude overnight in Wangara, Australia. Numbers attached to the profile lines indicate the correspondent night-time. Figure retrieved from Stull (1988)..... 7
Figure 1.5 – Corrected reflectance (True-color) satellite image of Southern African subcontinent's cloud-cover, on December 3rd 2020, retrieved from Suomi National Polar-Orbiting Partnership (Suomi NPP) spacecraft, using the Visible Infrared Imaging Radiometer Suite (VIIRS). VIIRS swaths the Equator at about 13:30 (LT). In the picture, a wide northwest-southeast oriented cloud bands over the region (where TTTs usually form), can be spotted. The latter is delimitated by 2 dotted red lines. Figure source: NASA Worldview..... 9
Figure 1.6 - Surface geopotential height (equivalent to surface topography) and main rivers/lakes over the South African subcontinent, retrieved from ERA5 reanalysis. Dotted red line indicates the Angolan-Namibian plateau (highlands) and cyan-blue thick line represent the region where the AL usually develops. Dark-blue square indicates the FRESAN project region, which corresponds to the area of interest. Green arrows mark both Limpopo (south) and Zambezi (north) LLJs. Dotted black line defines the mountainous range of the East African Rift System (EARS). Dotted violet line defines the Angola-Benguela Front (ABF)..... 10

Figure 2.1 - Map of SW African subcontinent showing the locations of 10 SASSCAL WS (red dots) used in this thesis. These WS are scattered over southern Angola and northern Namibia and are part of a recent installed WS network in the region. 14
Figure 2.2 - Pictures of some of the SASSCAL project WS, whose data was retrieved and used in this work. These WS are placed in **(a)** Namibe, Angola; **(b)** Okangwati, Namibia; **(c)** Tundavala, Angola. Pictures source: SASSCAL project. 14
Figure 2.3 - Monthly mean of ERA5 geopotential height (at 800 [hPa]) over austral Africa in February 2013. Both pink stars indicate the selected local minimums representative of the AL and MCT. As described before, the pink star represents the location of the absolute gh800 minimum, and the red squared box surrounding it, stands for the surrounding area used to determine the average value of gh800 around the absolute minimum. The latter were used to define a searching criterion, to prevent local effects to interfere with the results. Local minima searching methodology was limited to 2 areas: the AL region, represented by the dark square [7.5-22ºS; 10-25ºE,], and the MCT region, represented as the green box, whose domain is [18-29ºS; 34-43ºE]. Dark-red square indicates the region of interest of this thesis and corresponds to an area where ERA5 precipitation data was retrieved for the SW African rainfall analysis – the domain is [13-20ºS; 12-18ºE] 17
Figure 2.4 – Regions of equatorial Pacific Ocean used to perform ENSO indexes. In this work, Niño3.4 index was retrieved, based on the Niño3.4 region (dark squared box between Ninño4 and Niño3 regions). Figure source: NOAA/GCOS. 19
Figure 2.5 – Map of the Indian Ocean with 3 groups of boxes used to calculate large scale modes of variability of SST. Red and blue squares correspond to indexes and areas not contemplated in this thesis. Green squared boxes correspond to both west and east Indian Ocean regions used to compute the SIOD index. Figure source: Jaffrés et al. (2018). 20
Figure 3.1 - Monthly averaged (1980-2020) integrated water vapour transport (IVT), retrieved from ERA5 reanalysis for the rainy season (November to April), over the south African subcontinent. Black quivers are spaced by 2ºx2º and represent the direction and magnitude of IVT. Shaded green colours also represent the magnitude value of IVT. Each panel (a to f) represent the following monthly sequence: **(a)** November, **(b)** December, **(c)** January, **(d)** February, **(e)** March and **(f)** April. On panel (a), the yellow line represents a meridional section of LRV and the blue line, of ZRV. The red line marks the place where the cross-sections presented in Figure 3.2 were made. 22
Figure 3.2 – Same as Figure 3.1, but for zonal specific humidity flux computed on pressure levels. The cross sections were made between 10ºS and 25ºS at a constant longitude of 30ºE (see the red line on Figure 3.1a). The *xx* axis in each panel correspond to latitude. Either Zambezi (ZRV) and Limpopo (LRV) river valleys are identified in the figure with white acronyms. 22
Figure 3.3 – Timeseries (January 2014 – December 2020) of ERA5 IVT_u and SASSCAL WS data. Every month, various cyan dots were plotted, each one representing a monthly rainfall value from a different WS. Cyan line stands for the average of all dot values within each month (i.e., indicates, in every month, the average precipitation of all WS). Dashed dark-blue line represents the monthly average WS rainfall anomalies (based on a 2014-2020 normal, due to the short WS timeseries). IVT_u anomalies (based on a 1980-2010 normal), were plotted as an average value for 2 sections at different locations, but at the same longitude of 30ºE: the LRV region [13ºS-17ºS] (orange line) and the ZRV region [20ºS-24ºS] (green line). Figure 3.1a marks the latter sections with a yellow (LRV) and blue lines (ZRV). Positive anomalies of IVT_u mean a more eastward (or less westward) moisture advection, and negative anomalies of IVT_u, represents a more westward (or less eastward) flux of water vapour. IVT_u anomaly axis is inverted for a clearer graphical visualization. Correlation values (see figure title), were performed between WS rainfall anomalies and IVT_u anomalies from LRV ($RLPP = -0.08$) and ZRV ($RZBZ = -0.50$). 23
Figure 3.4 – Wind roses representing mean daily ERA5 wind data (850[hPa]) for each 1980-2020 NDJFM periods (over the region of interest – see red box in Figure 2.3). Each panel displays a wind

rose that corresponds to **(a)** dry days (daily rainfall below the 25th percentile for the correspondent month), **(b)** normal days (daily rainfall between the 25th and 75th percentile) and **(c)** wet days (daily rainfall above the 75th percentile for the respective month). Percentages shown in the figure axis, correspond to wind speed frequencies, i.e., longer sectors represent higher frequencies of wind from that quadrant. Each sector is divided in 5 coloured wind speed intervals (displayed in the legend). The colour that matches a longer sector division, corresponds to the most frequent wind speed interval registered in the winds coming from that quadrant. 25
Figure 3.5 – Composites of ERA5 precipitation anomaly for all rainy season months of November, December, January, February and March (1980-2020), over the austral African subcontinent, that registered **(a)** weak Zambezi LLJ (IVT_u > 75th percentile), **(b)** strong Zambezi LLJ (IVT_u < 25th percentile), **(c)** weak Limpopo LLJ (IVT_u > 75th percentile) and **(d)** strong Limpopo LLJ (IVT_u < 25th percentile). Each panel (or composite) is computed by averaging all months that present the LLJ characteristics previously described. The number of months (*n*) used to compute the average is presented in the lower left of each panel. Precipitation anomalies were computed with respect to the 1980-2010 normal. Significant rainfall anomalies, using a Student's t-test for a 95% of confidence interval, are represented as dotted areas across each subplot (see subsection 2.4). IVT_u data was retrieved the same way it was done for plotting Figure 3.3 (i.e., using averaged values with respect of both sections presented in Figure 3.1a). 27
Figure 3.6 – Timeseries of rainfall anomalies (1980-2020) over the region of interest (see red box in Figure 2.3), versus IVT_u anomalies from **(a)** Zambezi LLJ and **(b)** Limpopo LLJ, all together, during the rainy seasons (NDJFM period). Blue bars represent months with positive rainfall anomalies and brown bars stand for below-normal precipitation months. Rainfall and IVT_u data were retrieved from ERA5. The Pearson-correlation value between ERA5 precipitation anomalies and Zambezi IVT_u was $R = -0.49$. Performing for Limpopo IVT_u, the result was $R = -0.19$. Precipitation anomalies were computed with respect to the 1980-2010 normal. IVT_u data was retrieved the same way it was done for plotting Figure 3.3 (i.e., using averaged values with respect of both sections presented in Figure 3.1a). Note that the right axis (IVT_u anomalies) is reversed for the sake of clarity, as done in Figure 3.3. 28
Figure 3.7 – Scatter plots of 1980-2020 rainy season months (November to March) geopotential height at 800[hPa] (gh800) for AL and MCT versus both Limpopo and Zambezi IVT_u intensities. Respectively, in each panel, it is shown **(a)** gh800 AL vs. Zambezi IVT_u; **(b)** gh800 MCT vs. Zambezi IVT_u; **(c)** gh800 AL vs. Limpopo IVT_u and **(d)** gh800 MCT vs. Limpopo IVT_u. Geopotential, rainfall and IVT_u data were retrieved from ERA5. Coloured dots indicate if the correspondent month (of each dot) was rainy, normal, or dry. To do this analysis, the 25th and 75th percentiles were computed for each month. Months with values of precipitation >75th percentile, were classified as rainy (blue dots); <25th percentile were classified as dry (red dots) and months with rainfall between the 25th and 75th percentile represented normal months (grey dots). The black line present in each panel corresponds to a linear regression performed using all the dots, being associated with a correlation (R) value displayed in the legend of each graph. Values of gh800 for the AL and MCT were computed via local minima searching methodology presented in subsection 2.3. Rainfall data corresponds to an average over the region of interest (dark-red square in Figure 2.3). 30
Figure 3.8 - Same as Figure 3.5, but for rainy season months that registered **(a)** weak MCT (gh800 MCT > 75th percentile), **(b)** strong MCT (gh800 MCT < 25th percentile), **(c)** weak AL (gh800 > 75th percentile) and **(d)** strong AL (gh800 < 25th percentile). Values of gh800 for the AL and MCT were computed via local minima searching methodology presented in subsection 2.3. Rainfall data corresponds to an average over the region of interest (dark-red square in Figure 2.3). The number of months (*n*) used to compute the average is presented in the lower left of each panel. Precipitation anomalies were computed with respect to the 1980-2010 normal. Significant rainfall anomalies, using a Student's t-test for a 95% of confidence interval, are represented as dotted areas across each subplot (see subsection 2.4). 32

Figure 3.9 - Scatter plot of 1980-2020 rainy season months (November to March) of AL vs. MCT gh800 (ERA5). Red line indicates the correspondent regression line. 33
Figure 3.10 - Same as Figure 3.5, but for rainy season months that registered a conjugation of **(a)** weak MCT (gh800 MCT > 75th percentile) and weak AL (gh800 > 75th percentile); **(b)** strong MCT (gh800 MCT > 75th percentile) and strong AL (gh800 < 25th percentile). 34
Figure 3.11 - Timeseries of ERA5 anomalies (1980-2020) of rainfall over the region of interest (see red box in Figure 2.3), versus ERA5 gh800 anomalies of AL (black line) and MCT (dotted black line), during the rainy seasons (NDJFM periods). Blue bars represent months with positive rainfall anomalies and brown bars stand for below-normal precipitation months Precipitation and gh800 anomalies were computed with respect to the 1980-2010 normal. Geopotential heigh anomalies (gh800) were computed according to the local-minimum searching methodology, presented in subsection 2.3. Note that the right axis of the figure was inverted for a better data visualisation. 35
Figure 3.12 – Monthly climatologies of retrieved ERA5 variables (for 1980-2020 period), over Southern African subcontinent. Green and orange boxplots represent, respectively, the monthly distribution of IVT_u (across the 40-year period) for Zambezi and Limpopo LLJs, with a grey line inside each box indicating the median value. As previously done, both LLJs' data were retrieved with respect to sections presented in Figure 3.1a. Dashed grey line marks IVT_u threshold between eastward ($IVT_u > 0$ [$kgm^{-1}s^{-1}$]) and westward ($IVT_u < 0$ [$kgm^{-1}s^{-1}$]) transport of water vapour. Blue boxplots with stripes, show rainfall monthly distributions, retrieved as an average of values over the region of interest (dark-red square in Figure 2.3). Values of gh800 for the AL (dashed black line with stars) and MCT (dashed dark-red line with triangles) were retrieved, for the rainy season months (Nov-Mar), using the local minimum searching methodology (subsection 2.3). With the disappearance of the AL and MCT during the dry season (Apr-Oct), gh800 values were computed as an average value of the region used to search both low-pressure systems (dark and green square area in Figure 2.3, corresponding, respectively, to AL and MCT regions). 36
Figure 3.13 – Monthly ERA5 data (for all December, January, and February 1980-2020) of AL latitude and gh800 anomalies, as well as of rainfall over the study region, according to combinations of both modes of variability (SIOD and ENSO), using Niño3.4 and SIOD indexes. All 4 combinations are associated with 2 boxplots: one representing the latitude distribution of the AL (cream colour) and the other one representing gh800 anomaly of the AL (blue, orange, green or red, depending on the aggregation of modes). The relative frequency of months with rainfall below the 25th percentile and above the 75th percentiles, for each combination, is displayed in grey boxes. The *n* stands for the number of months used in each combination. Green area delimits the latitudes of the region of interest (FRESAN project). 38
Figure 3.14 - Same as Figure 3.5, but for rainy season months that registered a conjugation of **(a)** positive SIOD and El-Niño conditions (Niño3.4 > 0.4[ºC]); **(b)** positive SIOD and La-Niña conditions (Niño3.4 < -0.4[ºC]); **(c)** negative SIOD and El-Niño conditions (Niño3.4 > 0.4[ºC]) and **(d)** negative SIOD and La-Niña conditions (Niño3.4 < -0.4[ºC]). 39
Figure 3.15 - ERA5 monthly anomalies (over the subcontinent) of 3 fields: precipitation (coloured shading), gh800 (dark-red contours) and IVT (dark-grey quivers), for **(a)** December 2018, **(b)** January 2019, **(c)** February 2019 and **(d)** March 2019. Dark-grey quivers are spaced 1.6ºx1.6º and gh800 (black contours) are interpolated across points spaced 0.75ºx0.75º. Dashed contours represent negative gh800 anomalies. Red line on panel (a) represent the section made to produce Figures 3.16 and 3.18. 42
Figure 3.16 - Meridional cross-sections (made at 30ºE, following the red line on Figure 3.15) of ERA5 zonal specific humidity (qu) anomalies for **(a)** December 2018, **(b)** January 2019, **(c)** February 2019 and **(d)** March 2019. Positive anomalies of qu mean a reduction of westward humidity transport intensity or even a change of the zonal direction of the LLJs (the transport become eastward). Negative

anomalies of qu, mean an intensification of the westward humidity transport across the LLJs. Either Zambezi (ZRV) and Limpopo (LRV) river valleys are identified in the figure with white acronyms. 43
Figure 3.17 – Same as Figure 3.15, but for the 2010/11 rainy season. 44
Figure 3.18 – Same as Figure 3.16, but for the 2010/11 rainy season. 45
Figure 3.19 – Timeseries of retrieved ERA5 variables, for 1980-2020 rainy season months (Nov-Mar), over the southern African region. In each panel, it is observed timeseries of **(a)** rainfall anomalies over the study region (SW Africa), where brown (blue) bars indicate below (above) normal precipitation months; **(b)** gh800 anomalies for weak and strong AL (black bars), as well as weak and strong MCT (orange bars); **(c)** IVT_u anomalies for Zambezi LLJ; **(d)** same as panel (c) but for Limpopo LLJ; **(e)** Nino3.4 index, where red bars represent El-Niño months (i.e. Niño3.4 > 0.4[ºC]) and blue bars, La-Niña months (i.e. Niño3.4 < -0.4[ºC]); **(f)** SIOD index, where red bars represent positive SIOD months and blue bars, negative SIOD months. The classification criteria used to distinguish strong and weak AL and MCT was the same used previously in subsection 3.3. SIOD and Niño3.4 computations are detailed in subsection 2.5. All anomalies were computed using 1980-2010 normal. Shaded grey areas indicate both case-studies of the present section, i.e., 2010/11 and 2018/19 exceptional rainy seasons. 47
Figure 3.20 – Schematization of what was learned from the section 3. 49
Figure 6.1 – Timeseries of accumulated precipitation (from ERA5), for every hydrological year, since 1980/81 (blue line). A hydrological year was defined as starting in each October 1st of the previous year and ending on September 30th of the actual year (e.g., in 1990/91 season, the hydrological year started in October 1st 1990 and ended in September 30th 1991). Rainfall data was retrieved for the area of interest (dark-red square in Figure 2.3). Dotted black line indicates the average value (1980-2010) of accumulated precipitation. Orange arrows corresponds to case-study years, analysed in subsection 3.5 of this thesis. 58
Figure 6.2 – Similar description to Figure 3.9. Red dots correspond to the exceptionally dry rainy season of 2018/19, analysed in subsection 3.5.1. Blue dots are related with the abnormally wet rainy season of 2010/11, studied in subsection 3.5.2. 59
Figure 6.3 – Panoramic view of a meeting between FRESAN team and native populations of Onkokwa (south of Angola). This meeting took place in a "meeting room" named *Jambo*. These local communities are part of a predominant southwestern Africa ethnic group named *Hereros*. The tribe shown in the picture is named *Macahones* (a subgroup of *Herero* ethnicity). Photo taken by the author, in April 2022. 59
Figure 6.4 – Picture of a meeting between FRESAN team and *Macahones* tribe (similar to Figure 6.3), but in an experimental agricultural field located in Onkokwa (southern Angola). Photo taken by the author, in April 2022. 60
Figure 6.5 – Picture of Huíla plateau's big cliffs (where altitudes reach ~2000[m]). Orographic-induced cumulus and cumulonimbus clouds above the plateau are depicted, which are responsible for significant rainfalls over this region, essentially in the rainy season. This image was taken in a West-to-East perspective (i.e., the mountain range is in the East, and, behind this perspective, there is the arid Namib desert and the Atlantic Ocean, where these stormy-cloud developments do not occur). Location: Namibe (southern Angola). Photo taken by the author, in April 2022. 61
Figure 6.6 – Similar description as Figure 6.5. This picture shows a better perspective of the aridity and dominance of clear skies over the desert region, contrasting with the cumulonimbus clouds development down in the mountains placed in the background. This photo was taken in the Namib desert, on the way to the mountains (temperate and rainier region). Location: Namibe (southern Angola). Photo taken by the author, in April 2022. 62
Figure 6.7 – Weather station located in the Namib desert, near the village of Tombwa, in Angola. This WS was installed and is managed by the FRESAN team. Photo taken by the author, in April 2022.. 63

List of Tables

Table 2.1 - List of IDs, locations, coordinates, altitudes, and the respective dates these WS started reporting (beginning of timeseries), for each one of the 10 SASSCAL WS used in this work. To observe, in a map, the exact location of all WS, see Figure 2.1. 13
Table 2.2 - Monthly averaged ERA5 retrieved variables (in single levels) for the period of 1980-2020 and its respective description and physical units. 15
Table 2.3 – Monthly averaged ERA5 retrieved variables (in pressure levels) for the period of 1980-2020 and its respective description, physical units, and correspondent pressure level(s). 16

List of acronyms and abbreviations

ABF	Angola-Benguela (oceanic) Front
AL	Angola Low; Angola Low pressure (system)
C3S	European Commission's Copernicus Climate Change Service
CI	Confidence interval
E	East; eastern
EARS	East-African Rift System
ECMWF	European Centre for Medium-Range Weather Forecasts
ENSO	El-Niño Southern Oscillation
ERA5	ECMWF 5th reanalysis generation (1979-present)
EU	European Union
FAO	United Nations' Food and Agriculture Organization
FRESAN	Acronym for the project "Fortalecimento da Resiliência e Segurança Alimentar de Angola"
GCOS	Global Climate Observing System (from NOAA)
gh800	Geopotential height at 800[hPa]
INAMET	Instituto Nacional de Meteorologia e Geofísica (de Angola)
IPMA	Instituto Português do Mar e da Atmosfera
IVT	Vertically Integrated Water Vapour Transport [$kg \cdot m^{-1} \cdot s^{-1}$]
HP	High pressure (system)
ITCZ	Intertropical Convergence Zone
LLJ	Low-level jet
LRV	Limpopo River Valley
MC	Mozambique Channel
MCT	Mozambique Channel Trough
N	North; northern
NDJFM	Time period between November and March (austral rainy season)

NE	Northeast; north-eastern
NMS	Namibia's Meteorological Service
NOAA	National Oceanic and Atmospheric Administration
NW	Northwest; north-western
PDF	Probability density function
SASSCAL	Acronym for the project "Southern African Science Service Centre for Climate Change and Adaptive Land Management"
S	South; southern
SE	Southeast; south-eastern
SIOCZ	South Indian Ocean Convergence Zone
SIOD	Subtropical Indian Ocean Dipole
SST	Sea surface temperature
SW	Southwest; southwestern
TTT	Tropical Temperate Troughs
W	West; western
WS	Weather station
ZRV	Zambezi River Valley
UN	United Nations

List of symbols

$\overrightarrow{V_g}$	Geostrophic wind (vector) [$m \cdot s^{-1}$]
u_g	Zonal component of the geostrophic wind [$m \cdot s^{-1}$]
v_g	Meridional component of the geostrophic wind [$m \cdot s^{-1}$]
V	Magnitude of mean wind velocity [$m \cdot s^{-1}$]
f	Coriolis acceleration [s^{-1}]
Φ	Geopotential [$m^2 \cdot s^{-2}$]
p	Atmospheric pressure [Pa]
ρ	Density (of air) [$kg \cdot m^{-3}$]
g	Earth's surface gravity acceleration [$m \cdot s^{-2}$]
z	Height [m]
IVT_u	Zonal component of Vertically Integrated Water Vapour Transport [$kg \cdot m^{-1} \cdot s^{-1}$]
q	Specific humidity [$kg \cdot kg^{-1}$]
$\dot{q_u}$	Zonal specific humidity transport [$kg \cdot kg^{-1} \cdot m \cdot s^{-1}$]
R	Pearson's correlation coefficient (0-1) [dimensionless]
n	Number of data samples; dataset length

1. Introduction

In most of African continent, essentially in semiarid regions (i.e., areas surrounding deserts), most of the economies rely on agriculture, an activity profoundly dependent on water resources, due to the scarcity of better land management and technology (Branca et al., 2013; Sultan & Gaetani, 2016). In addition to this problem, as expressed in Wheeler & von Braun (2013) and Sarr (2012), these areas are identified as climate *hot spots*, due to their vulnerability to climate change and, consequently, sensible to hazardous weather and climate conditions (such as extreme rainfall, floods, or severe droughts). These in turn are the cause of diseases, malnutrition, food insecurity, and migration phenomena, as the stability of food systems might be at risk under warming climates. This means that most of vulnerable areas show a high social and economic exposure to oscillations on climate patterns and extreme weather events (Liu et al., 2015).

Southwest (SW) Africa is not an exception to this problem. As explained in Sultan & Gaetani (2016), the region is known to be particularly exposed to climate variability due to its high reliance on rain-fed agriculture and limited economic and institutional capacity to respond to unpredictable severe climate events, most of them still poorly understood. Recent literature covering SW Africa regions, projects a widespread warming, a generalised precipitation reduction, increased aridity, and a significatively loss of biodiversity over the subcontinent, essentially in the western parts, such as Namibian and Angolan territories ("southern Africa subcontinent", in this context, means the part of the African continent laying below the Equator – from 0º to approximately 40ºS). However, increasing river floods are also projected for the region (Collins et al., 2013; IPCC, 2021). Thus, a better knowledge on how global warming will modify the rain cycles and dynamics over SW Africa is crucial to develop better policies and take actions to mitigate serious climate-related effects.

To better understand the climate variability in Africa, it is useful to get an insight about Africa's climate zones distribution. Following the description presented in Peel et al. (2007), the African continent is divided in 3 main Köppen–Geiger climate categories. The most dominant climate type is arid (B), covering ~57% of the territory, followed by tropical (A), representing ~31%, and temperate (C), found in ~12% of Africa. Each climate type is divided in several subtypes. Figure 1.1 shows the way these climate subtypes are spatially distributed over the continent. It is possible to see that mid-latitude regions (~30ºN and ~30ºS) are dominated by drier climates (B types) as A types are mainly found over the equatorial regions. However, in the south of Africa, temperate climates (C types) also appear, often related to highlands.

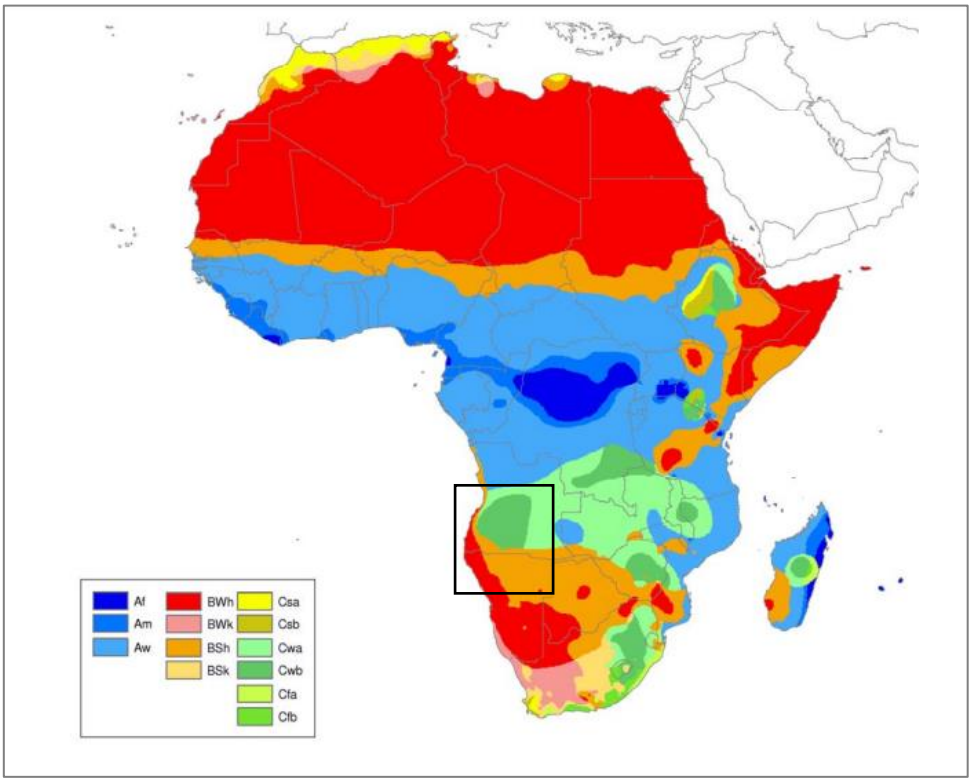

Figure 1.1 – Spatial distribution of Köppen–Geiger climate subtypes over the African continent. Climate subtypes legend: Af – tropical rainforest; Am – tropical with monsoons; Aw – tropical savannah with dry winters; BWh – hot arid desert; BWk – cold arid desert; BSh – hot steppe desert; BSk – cold steppe desert; Csa – temperate with dry and hot summer; Csb – temperate with dry and warm summer; Cwa – temperate with dry winter and hot summer; Cwb – temperate with dry winter and warm summer; Cfa – temperate with hot summer but no dry season; Cfb – temperate with warm summer but no dry season. The dark square indicates the region of interest, i.e., southwestern Africa. Source: Peel et al. (2007).

Thus, SW Africa can be characterized by B type climates (arid or semiarid), essentially over Namibia and southern Angola, with a close-to-shoreline narrow band oriented northward (reaching northern Angolan coastal regions). Temperate climates (C type) are verified mainly in the Angolan plateaus (over central parts of the country), also covering places such as Zambia and southern Democratic Republic of the Congo. Type A climates (tropical), not only represent a characteristic of northern Angola, but also of small areas over central-west Zambia.

1.1. Main SW Africa weather dynamics

Most of SW Africa climate is characterized by a *dry season* that lasts from April/May to October (austral winter) and a *rainy season* occurring between November and March/April (austral summer). As displayed in Figure 1.2, over southern Angola and northern Namibia, throughout the *dry season*, it typically rains less than 20[mm/month]. Nonetheless, in the *rainy season*, values of precipitation above 100[mm/month] are frequently recorded. It is noteworthy that from January and February, the distributions are skewed towards higher precipitation amounts, suggesting the occurrence of less frequent but relatively strong events. Temperature shows a weak seasonal cycle, with mean temperatures in the summer being slightly higher than in winter.

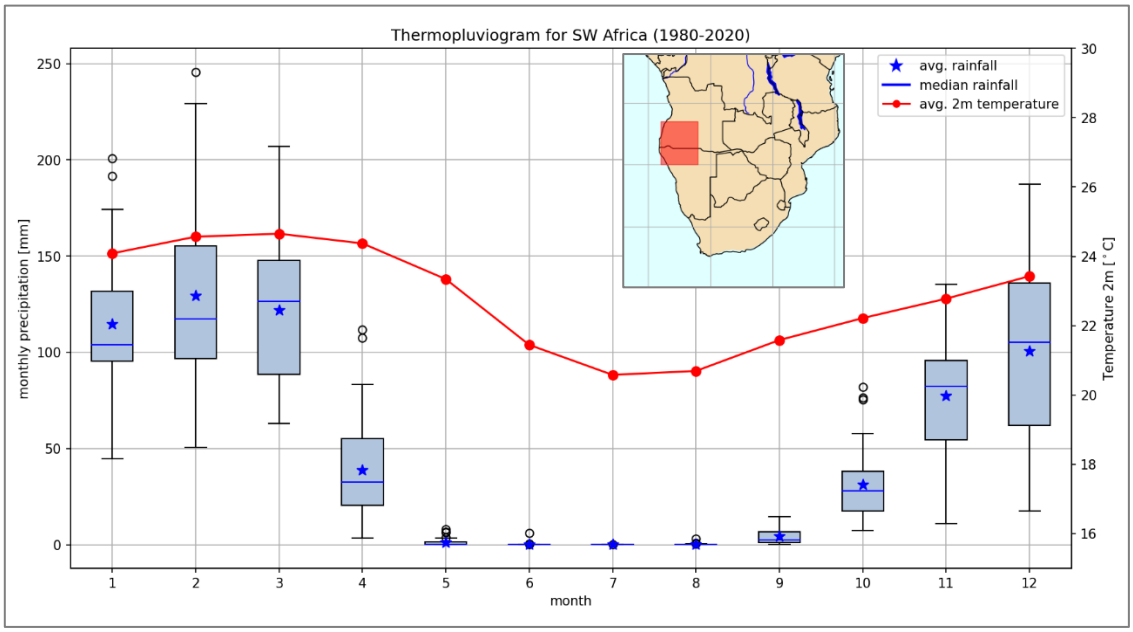

Figure 1.2 - Termopluviogram for Southern Angola and Northern Namibia using 1980-2020 monthly averaged data from ERA5 reanalysis. All monthly precipitation and temperature data used in this figure are average values over a box in SW Africa (southern Angola and northern Namibia), represented by the red box on the inset map and covering the area [13º-20ºS; 12º-18ºE] - the latter, indicates the region of interest. Boxplots represent the precipitation variability, for each month, over the 40 years of data. Inside the boxplots, blue stars represent the average precipitation value for that month and the blue line shows the median value. Circles outside boxplots display the outliers. The red line unifies the red dots, where each dot stands for the 1980-2020 average temperature value (over the red box) for each month.

In fact, as shown in Figure 1.3a, during the *dry season*, dynamical air circulations persist around two semipermanent synoptic anticyclonic features, i.e., high pressures (HP) – the Mascarene High (South Indian Ocean) and the St. Helena High (South Atlantic) – inducing an almost constant pattern of easterly winds over the subcontinent. Both HP systems shift west and intensify throughout this season, while a branch of these HP regimes forms over southern Botswana, originating an HP system named Kalahari HP (or Botswana Anticyclone), also promoting a winter easterly flow pattern over SW Africa (Barry & Chorley, 2003; Huntley et al., 2019). These subsidence systems appear approximately at the same latitude, representing a surface manifestation of a strengthened downward limb of the southern hemisphere's Hadley Cell over southern Africa in the winter season (Tyson & Crimp, 1998). As stated, in Barry and Chorley (2003) and Huntley et al. (2019), such HP regimes do not allow moisture convergence to occur at lower levels in the atmosphere. In fact, with the Intertropical Convergence Zone (ITCZ) away from southern Africa (as it migrates northward during this time of year, following the position of maximum surface heating associated with the meridional displacement of the overhead position of the sun), little water vapour transport occurs towards the subcontinent and, consequently, little rainfall and clouds are produced. Nonetheless, during this season, coastal steep orography together with the St. Helena HP influence, enhance a subsidence pattern on the easterly flow, and increase static stability of the lower troposphere over the Atlantic off the Angolan-Namibian coast which, together with low sea surface temperatures (SST) due to the cold upwelled waters from the Benguela current (extending parallel to the shoreline), contribute to generate layers of stratocumulus clouds and persistent fog over these places, in a phenomenon locally called *cacimbo* (Huntley et al. 2019; Lima 2019; Lima et al. 2019; Patricola & Chang, 2017; Richter 2004).

Over the *rainy season*, summer rainfall occurring across SW Africa results by low-level transport of water vapour, mainly from 3 sources: Atlantic Ocean, Indian Ocean, and deep tropical regions over equatorial Africa (see thick black arrows displayed in Figure 1.3b) (Barimalala et al., 2021; Munday & Washington, 2017; Rapolaki et al., 2020). Over the Indian Ocean, easterly low-level moisture fluxes are generally influenced by the Mascarene semipermanent HP and by the north-eastern monsoon offshore Somali coastline. From the Atlantic Ocean, westerly humidity fluxes are influenced by a summertime semipermanent low-pressure system centred near the Angola-Namibian border (named Angola Low, or AL – explored in detail on subsection 1.3). Some humidity fluxes towards northern Namibia and southern Angola are also induced by St. Helena HP. Indian and Atlantic Ocean low-level moisture fluxes clash with each other, enhancing the convective power of the ITCZ over the subcontinent (which is placed south of the equator in this time of year), promoting cloud formation and precipitation – the regions where these collisions of low-level moisture fluxes occur, are part of the ITCZ, and are known as the South Indian Ocean Convergence Zone, or simply SIOCZ (Barimalala et al., 2018, 2021; Barry & Chorley, 2003; Huntley et al., 2019). The permanence of an easterly wind regime over the subcontinent allows moisture transport towards continental southern Africa. However, Madagascar island serves as a topographic barrier to this easterly flow, which ends up being shifted southwards by dynamical adjustments, generating a cyclonic circulation over the Mozambique Channel (MC), named Mozambique Channel Trough (or MCT). This cyclonic feature is prominent in austral summer and is usually placed south of the MC (Barimalala et al., 2019). The MCT is sustained by oceanic-atmospheric interactions, such as relatively warmer SSTs over the MC. As defined in Behera & Yamagata (2001), upper-ocean SST variability of Indian Ocean is evaluated by an index named Subtropical Indian Ocean Dipole (SIOD), defined as the difference between SST anomalies from 2 sectors of the Indian Ocean: western ([27º-37ºS; 55º-65ºE]) and eastern ([18º-28ºS; 90º-100ºE]). Positive SIOD indicate warmer-than-normal SSTs over the MC and vice-versa for negative SIOD phases. Nevertheless, positive SIOD, associated with well above average SST events (marine heatwaves) seem to be linked with lighter winds, westward-than-normal Mascarene HP system influence, and weaker MCTs, inducing above-normal rainfalls across south-central Africa (Barimalala et al., 2019, 2021; Behera & Yamagata, 2001; Mawren et al., 2022).

In short, during austral summer, the MCT, together with the main synoptic easterly flow (induced by Mascarene HP and partially shifted by Madagascar's orography), originates an easterly transport of moisture towards continental southern Africa. However, these fluxes end up colliding with a wide mountain range, entraining into its valleys, creating favourable conditions to generate *low-level jets* (Munday et al., 2021). This process is detailed below.

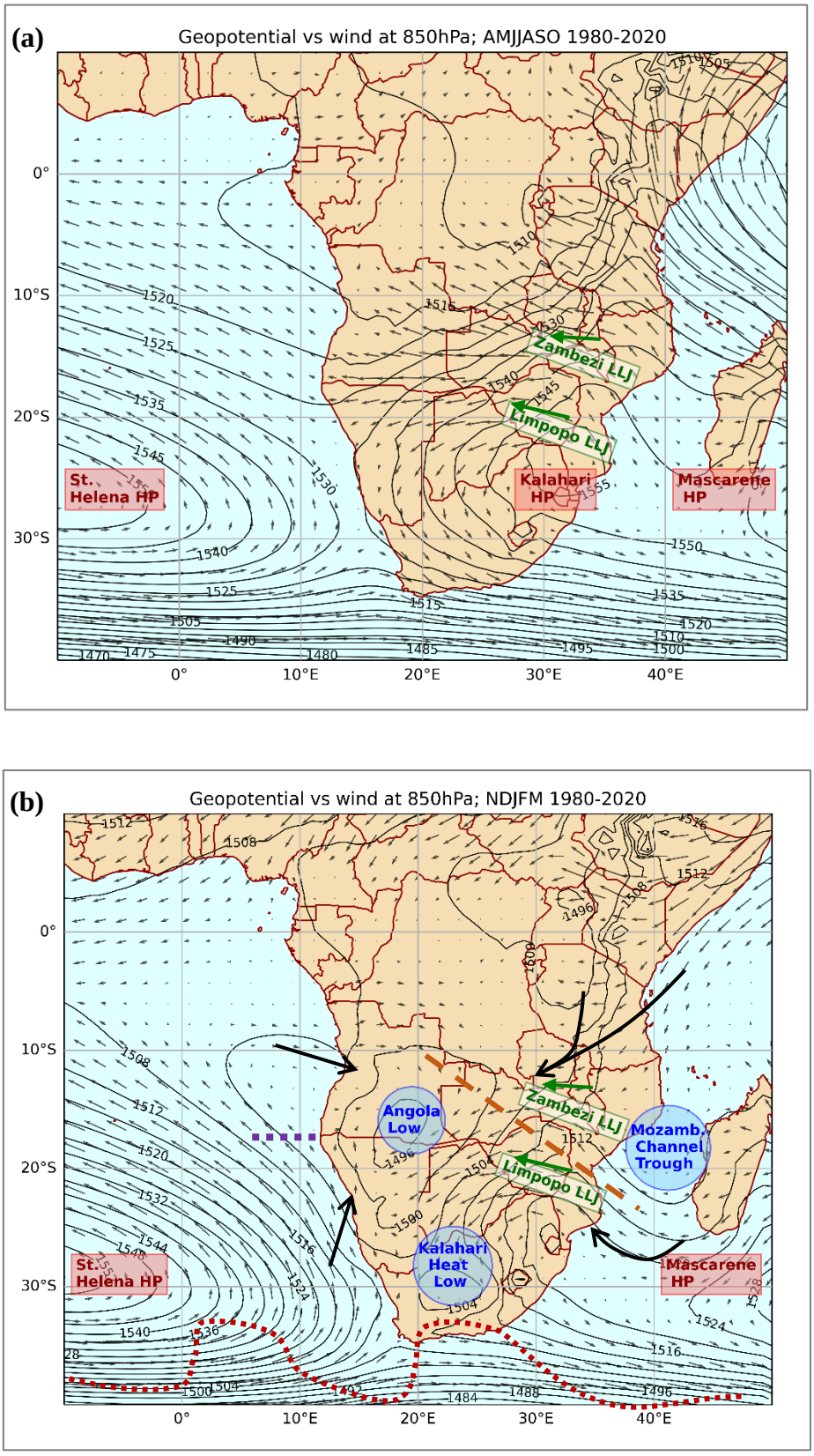

Figure 1.3 - Maps of Southern African subcontinent showing 1980-2020 averaged seasonal data for geopotential height (black contours, interpolated across points spaced 0.75ºx0.75º) and wind (grey quivers spaced 1.5ºx1.5º), retrieved at 850[hPa] for the period of **(a)** dry season (April to October) and **(b)** rainy season (November to March). Within the isolines of equal geopotential height, the correspondent value is displayed. The length of the quivers is proportional to its magnitude. Based on Munday &

Washington (2017), Barimalala et al. (2021) and Rapolaki (2020), thick black quivers represent the main routes of water vapour transport towards SW Africa, the dotted dark red line schematically illustrates the pattern of a typical austral mid-latitude Rossby wave (explored in the subsection 1.3, below), the dashed orange line defines de SIOCZ, and the dotted violet line defines the Angola-Benguela Front (ABF; see subsection 1.3). Green quivers indicate the location and main direction of both Zambezi and Limpopo LLJs (see subsection 1.2). Both figures for dry and rainy seasons display the main weather features' names (over the regions they usually develop), with HP meaning *high-pressure* and LLJ standing for *low-level jet* (see subsection 1.2, below). The production of this figure was also inspired by van Heerden & Taljaard (1998) work.

1.2. Low-level jet dynamics and its relationship with moisture transport

Transport of humidity can occur via thin sheets of meandering fast-moving air (behaving as a *jet*), within the first kilometre above surface (usually z~300[m]), peaking maximum velocities of ~10-20[ms^{-1}] (Algarra et al., 2019; Stull, 1988). Since it was firstly named by Means (1952), these atmospheric phenomena acquired the designation of *low-level jet*s (LLJs). Together with atmospheric rivers, this process represents one of the most significant ways to transport water vapour internally in the troposphere (Algarra et al., 2019; Payne et al., 2020; Ramos et al., 2016, 2019). LLJs usually reach their maximum velocities during night-time (near pre-dawn hours, as shown in Figure 1.4), and are considered as super-geostrophic phenomena (i.e., LLJs' wind speed becomes higher than the geostrophic wind originated within the same atmospheric conditions). Thus, some LLJs are usually referred to as *nocturnal jets*, which are common boundary-layer phenomena. They are caused by strong wind shears triggered by vigorous friction at the surface during the day. At dusk, as the turbulence inside the boundary-layer decreases (i.e., it becomes more stable, sometimes forming a *stable boundary-layer*), inertial oscillations are induced by these strong wind shears and by the Coriolis force (i.e., wave-like undulations of the wind speed around the geostrophic value are generated). Thus, at some point during the night, these inertial oscillations of the wind speed reach their maximum value (i.e., wind becomes *super-geostrophic*) (Blackadar, 1957; Stull, 1988). In other words, the reduced influence (or even absence) of the surface friction in the wind field aloft, can induce a higher-than-normal wind velocities, forming jet-like features with *super-geostrophic* wind speeds. In Figure 1.4, typical nigh-time mean wind profiles of the boundary-layer are presented, where wind speed maxima are found some hundreds of meters above the surface.

As also described in Stull (1988), LLJs can occur as a dynamic response to several factors, such as baroclinicity associated with weather patterns or sloping terrains, fronts, land-sea thermal contrasts, mountain/valley constraints or inertial oscillations. Most of the response to generated pressure gradients is given by quasi-geostrophic adjustments of the flow.

Holton (2004) describes these dynamical responses to pressure gradients with an equation for geostrophic wind ($\overrightarrow{V_g}$), in isobaric coordinates (equation 1.1):

$$\overrightarrow{V_g} = f^{-1}\vec{k} \times \nabla\Phi \tag{1.1}$$

Where $\nabla\Phi$ stands for geopotential gradient, the letter f represents the Coriolis parameter, and $\vec{k}$ is the unit vector. The previous equation can be split in a 2-equation system (in cartesian coordinates) for both components of geostrophic wind ($u_g; v_g$) (equation 1.2), where $\left(\frac{\partial p}{\partial x}; \frac{\partial p}{\partial y}\right)$ stands for, respectively, zonal, and meridional pressure gradients induced by horizontal thermal contrasts.

$$\begin{cases} v_g = \frac{1}{f}\frac{\partial p}{\partial x} \\ u_g = -\frac{1}{f}\frac{\partial p}{\partial y} \end{cases} \tag{1.2}$$

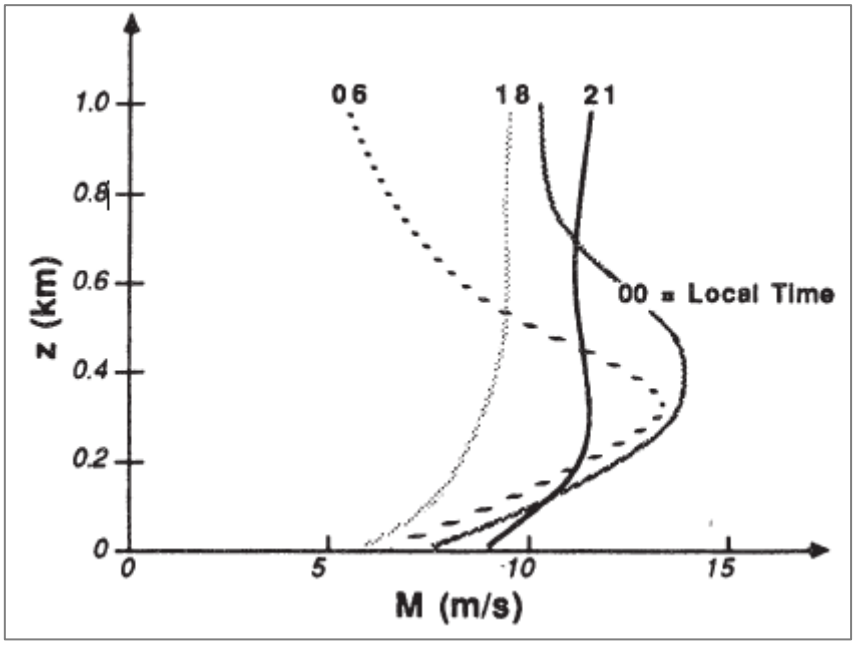

Figure 1.4 - Profiles of wind speed magnitude overnight in Wangara, Australia. Numbers attached to the profile lines indicate the correspondent night-time. Figure retrieved from Stull (1988).

However, some of the existing LLJs are also induced by mechanical adjustment to obstacles (such as, e.g., river valleys), other than simply generated by thermal-induced pressure gradients. Bernoulli's equation can be applied in these situations of channelling of the flow when it clashes with a valley or orographic depression (Munday et al. 2021). As explained in Cimbala & Çengel (2007), Bernoulli's equation, when applied in a permanent incompressible flow, is given by:

$$\frac{p_1}{\rho} + \frac{{V_1}^2}{2} + gz_1 = \frac{p_2}{\rho} + \frac{{V_2}^2}{2} + gz_2 \tag{1.3}$$

Where the pairs (p_1, p_2), (V_1, V_2) and (z_1, z_2) represent, respectively, the pressure (in [Pa]), the velocity (in [m/s]) and the height (in [m]) of the fluid (in this case, the air flow), before and after the narrowing of the channel. Density of the fluid is represented by ρ (in $[\mathrm{kg} \cdot \mathrm{m}^{-3}]$) and the gravity acceleration is given by g $[\mathrm{m} \cdot \mathrm{s}^{-2}]$. Using equation 1.3, it is possible to demonstrate that:

$$V_2 > V_1$$

In other words, the flow accelerates after passing a valley, generating a significatively fast wind speed at low levels in the troposphere (an orographically induced LLJ).

In fact, LLJs have been observed and characterized in every continent of the world, over places such as California (Burk & Thompson, 1996; Douglas, 1995), the Caribbean (Sáenz & Durán-Quesada, 2015), Amazon and central Brazil (Guedes do Nascimento et al., 2016; Oliveira et al., 2018), Chile (Garreaud

& Muñoz, 2005), the Iberian Peninsula (Rijo et al., 2018; Soares et al., 2017), China (Miao et al., 2018) or off the coast of the Arabian Sea (Ranjha et al., 2013, 2015). In southern Africa, strong LLJs exist along the coast of Angola and Namibia (Lima et al., 2019; Patricola & Chang, 2017), however, 2 main mountain valleys are associated with intense nocturnal LLJs responsible for a considerable transport of water vapor from the Indian Ocean towards the southwestern part of the subcontinent: the Limpopo River valley low-level jet (or LRV LLJ) and the Zambezi River valley low-level jet (or ZRV LLJ). Both LLJs are mainly induced by horizontal thermal contrasts (mechanism explained via equations 1.1 and 1.2) and by the Bernoulli effect (equation 1.3), particularly when dominant easterly winds clash with the river valleys (increasing their velocities) (Barimalala et al., 2018; Munday et al., 2021; Spavins-Hicks et al., 2021). These valleys are located within a large mountain range, covering most of eastern Africa, named East African Rift System, or EARS (from South Africa up to Somalia, as seen in a dotted black line in Figure 1.6). This set of complex orography contains several other river valleys associated with LLJs, which are responsible for water vapor transport towards the interior of the continent. This transport is the main mechanism for rainfall generation in these regions (Munday et al., 2021), which, as discussed before, represents a crucial element for the economy, society, and biodiversity of such areas. With this in mind, the scope of this thesis is to perform a deeper analysis on the role of LRV and ZRV LLJs and their implications on southern African rainfall.

1.3. The Angola Low as a key feature to rainfall

In fact, both LLJs allow an advection of humidity, in the lower troposphere, towards SW Africa, however, water vapour convergence is an important mechanism for local rainfall generation – it is where a semipermanent low-pressure system over Angola plays a key role. In SW Africa, an understudied atmospheric low-pressure system (named Angola Low, or simply AL) is responsible for most of daily to seasonal austral summertime rainfall (mainly convective) and moisture variability over the region, influencing humidity convergence at low levels in the atmosphere (Desbiolles et al., 2020; Pascale et al., 2019). Recent works using numerical climate models highlight the critical role played by convective precipitation and moisture convergence when producing climate change scenarios for Africa (Senior et al., 2021). This semipermanent cyclonic feature is often placed in the region of SE Angola, northern Namibia, and western Botswana, at about 13-14ºS, between November and March (i.e., late austral spring and summer) (Howard & Washington, 2018; Munday & Washington, 2017). It is characterized as an 850[hPa] geopotential minimum (see Figure 1.3b) (Munday & Washington, 2017) or a 700[hPa] relative vorticity minimum (Crétat et al., 2019a) over these places. In the end of the XX century, a series of theoretical studies about the dynamics of heat lows concluded that AL is a thermal low formed by dry and warm easterly continental air originated in the interior of Africa (as it is affected by topographic effects and interactions with the warm continental surface) (Reason, 1996). However, recent research on this system revealed that the AL starts as a thermal-induced low-pressure system during austral spring, transitioning, throughout the summer, into a deep tropical depression, feed by moisture convergence that originates instability and strengthens the AL system (Howard & Washington, 2018; Munday & Washington, 2017).

AL circulation dynamics, together with other southern African cyclonic features, such as the MCT, manages to converge easterly moisture fluxes from Indian Ocean with westerly moisture fluxes from Atlantic Ocean (Barimalala et al., 2018; Desbiolles et al., 2020; Rouault et al., 2003). This process strengthens the AL even further and forms a wide set of northwest-southeast tropical-extratropical cloud band systems, named Tropical Temperate Troughs (TTTs). TTTs correspond to one of the most important synoptical rainfall mechanisms of the south African subcontinent and are responsible for 30-60% of wet days over the region (Hart et al., 2013; Macron et al., 2014). As explained in Macron et al.

(2014), Munday & Washington (2019) and Reason & Smart (2015), these TTTs are formed and intensified by the passage of abnormally large west-to-east baroclinic extratropical Rossby waves (over southern hemisphere mid-latitudes – see dotted red line representing these waves in Figure 1.3b), which interact with tropical convective systems developing over southern Africa. Most of the TTTs are induced by latent heat energy provided by the warmer waters of the Agulhas current, interacting with storm tracks in the Southern Ocean, St. Helena and Mascarene highs, and with the AL and MCT. However, such interactions remain poorly understood, even though some studies point out ENSO (El-Niño Southern Oscillation) as a key driver of these waves' variability (Howard & Washington, 2019; James et al., 2020; Lyon & Mason, 2007). Strong wind-shears generated by LLJs and by the main easterly flow over the subcontinent might produce instabilities and mechanical turbulence, enhancing cloud bands over the region as well as excessive rainfall (Mulenga et al., 2003; Spavins-Hicks et al., 2021; Stull, 1988). In this way, wide cloud-bands appear diagonally from AL region down to southern MC, embedded in the SIOCZ (Cook, 2000; Desbiolles et al., 2020; James et al., 2020; Macron et al., 2014). These cloud-bands are often spotted over austral Africa during the rainy season, as seen in the example of Figure 1.5.

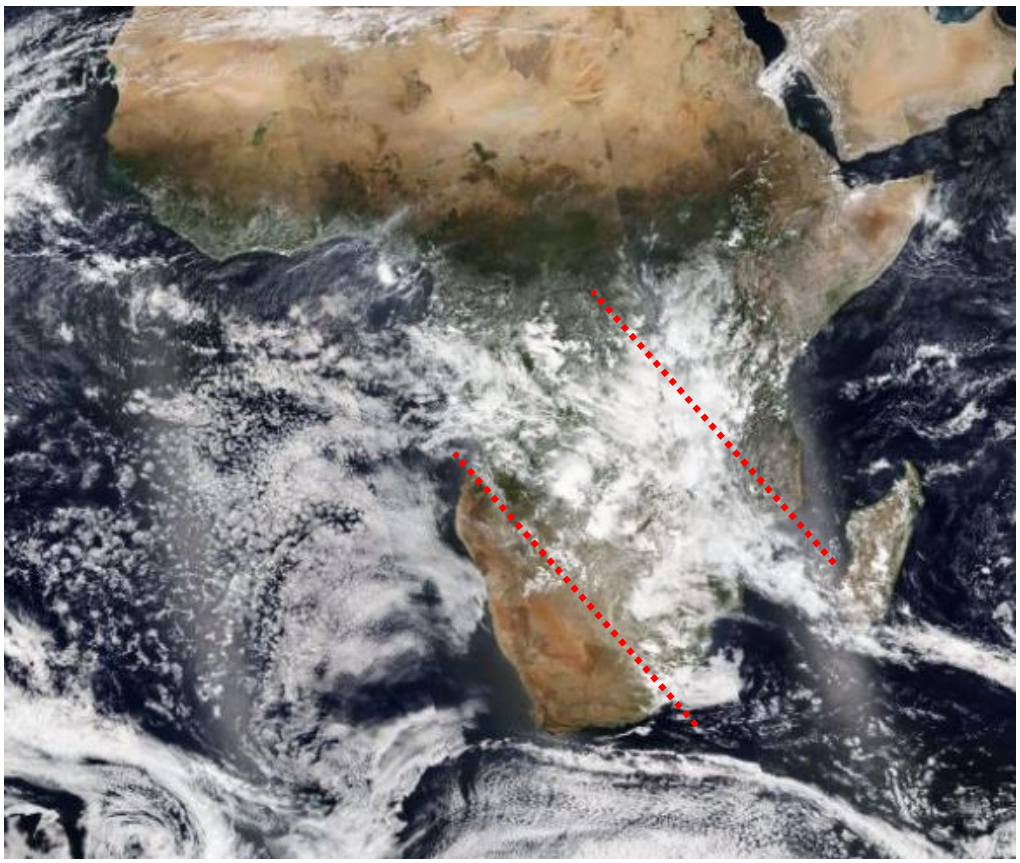

Figure 1.5 – Corrected reflectance (True-color) satellite image of Southern African subcontinent's cloud-cover, on December 3rd 2020, retrieved from Suomi National Polar-Orbiting Partnership (Suomi NPP) spacecraft, using the Visible Infrared Imaging Radiometer Suite (VIIRS). VIIRS swaths the Equator at about 13:30 (LT). In the picture, a wide northwest-southeast oriented cloud bands over the region (where TTTs usually form), can be spotted. The latter is delimitated by 2 dotted red lines. Figure source: NASA Worldview.

Stronger phases of AL have been associated with an intense NW and NE transport of humidity from the Indian Ocean towards SW Africa, joining moisture transport from the Atlantic Ocean (Howard & Washington, 2018; Munday & Washington, 2017), however, convergence of water vapour fluxes from both oceans do not entirely explain the semipermanent regime of the AL (throughout most of the austral summer). In fact, the AL system tends to stay *quasi-stationary* over south-eastern Angola and north-eastern Namibia. The reason for this type of regime is due to the existent steep orography covering most of the Angola-Namibian interior regions with mountainous escarpments rising above 1000 [m], and an extensive interior plateau of 1000–1500 [m] high (e.g., Bié Plateau, Huíla Highlands, Otjihavera mountain ranges – see dotted red area in Figure 1.6), promoting, through dynamical adjustments, anabatic wind flows over these mountainous places, inducing uplifting of air and thus, serving as dynamical barrier for low-level moisture convergence, feeding the AL system (Crétat et al., 2019; Desbiolles et al., 2020; Howard & Washington, 2018; Huntley et al., 2019; Munday & Washington, 2017).

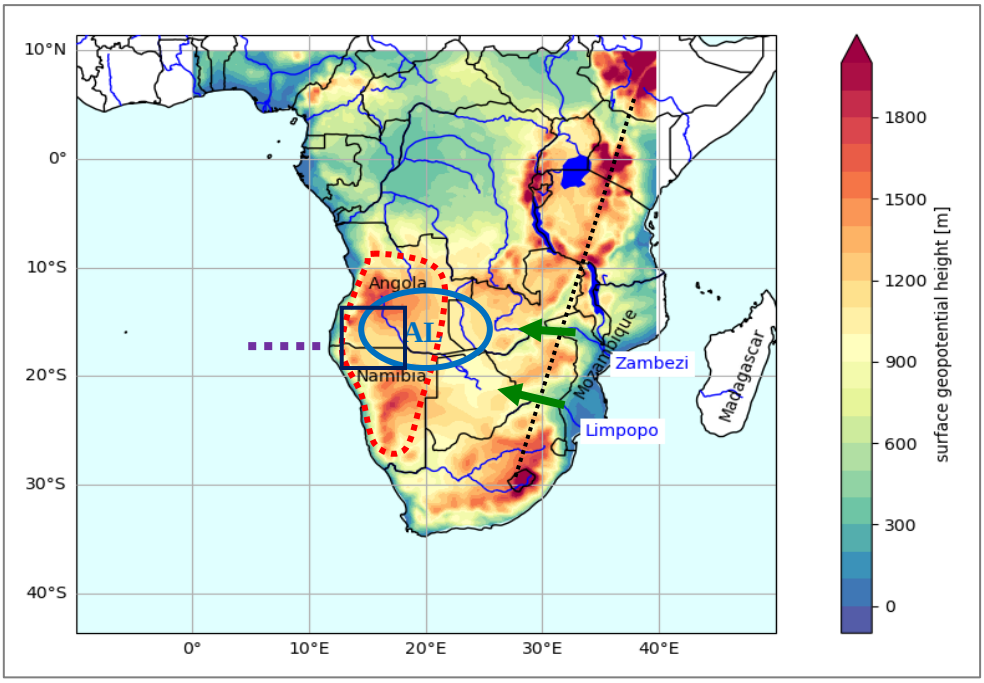

Figure 1.6 - Surface geopotential height (equivalent to surface topography) and main rivers/lakes over the South African subcontinent, retrieved from ERA5 reanalysis. Dotted red line indicates the Angolan-Namibian plateau (highlands) and cyan-blue thick line represent the region where the AL usually develops. Dark-blue square indicates the FRESAN project region, which corresponds to the area of interest. Green arrows mark both Limpopo (south) and Zambezi (north) LLJs. Dotted black line defines the mountainous range of the East African Rift System (EARS). Dotted violet line defines the Angola-Benguela Front (ABF).

The AL can also be intensified (or weakened) by other factors, such as the sea surface temperature (or SST). In fact, as explained in Imbol Koungue et al. (2019), in an oceanic region offshore SW African coast (near Angola-Namibia border), two water masses – one from the south (i.e., colder), advected by the Benguela current, and other from the north (i.e., warmer), transported by the Angola current - converge, creating a thermal oceanic front, named *Angola-Benguela Front* (ABF). The ABF is represented in Figure 1.3b and in Figure 1.6 as a violet dotted line. This oceanic front can play an

important role on weather and climate variability over Angola and Namibia regions. In fact, every few years, El Niño-like phenomenon promotes anomalous warming of the ocean surface over the Benguela current region – an event known as *Benguela Niño* (Caldeirinha, 2017; Imbol Koungue et al., 2019). Actually, Desbiolles et al. (2020) concluded that the increasing of mesoscale SST variability over the ABF region is associated with a significant AL intensification and, consequently, with above-normal rainfall over SW Africa. That work also emphasised the influence of SST anomalies over the ABF on latent heat fluxes in the region. As explained there, sharp SST gradients and increased baroclinicity regimes over the ABF, affects the southward low-level air flows over of these places (and over regions north of the ABF), nonetheless, such processes are still poorly understood and require future investigation. In this context, Reason and Smart (2015) also linked some severe precipitation events off the Angolan coast and across northern Namibian regions with high SSTs over SE Atlantic Ocean, especially during austral summer.

The present thesis is integrated on a project funded by the European Union (EU), named FRESAN ("Fortalecimento da Resiliência e Segurança Alimentar em Angola" or "Strengthening Resilience and Food Security in Angola"). FRESAN project is managed by Camões I.P. (Portuguese international institution dedicated to the worldwide promotion of the Portuguese language, Portuguese culture, and international aid, on behalf of the Government of Portugal). With the help of the Portuguese Institute for the Sea and Atmosphere (IPMA) and Angola's Instituto Nacional de Meteorologia e Geofísica (INAMET), part of the project aims, in the next few years, to install weather stations and water facilities (e.g., small dams, storage reservoirs, wells, pumping devices) across southern Angola, in order to help these populations to adapt to future regional climate changes over the region. Some photographic records of one of the FRESAN missions realized in April 2022 are presented in subsection 6.3 (see Appendix). The region of interest is presented in Figure 1.6 as a dark-blue square, i.e., the focus was given to the southwestern region of Africa, namely southern Angola and northern Namibia, as they represent regions of interest of the FRESAN project.

In this way, the main purposes of this work are, respectively:

- Study main synoptic mechanisms of humidity transport towards the region of interest (SW Africa).
- Identify sources of precipitation variability over the subcontinent (in particular, SW Africa) and comprehend synoptic atmospheric circulation patterns associated with wetter or drier periods across the region.
- Understand the way large-scale weather patterns affect the main synoptic atmospheric circulation, and its implications on rainfall variability across the subcontinent.

The remaining thesis is organized as it follows. In section 2, the methodology used to explore weather features and their influence on regional SW African rainfall is presented. In section 3, the results of this thesis are shown and discussed. Final conclusions are presented in section 4.

2. Methodology

During the preparation of this thesis, it was particularly hard to work with *in situ* data from this African region, mainly due to the absence of a good weather station network with a reasonable temporal extent and spatial resolution. To understand the reasons behind this problem, it is important to have some background historical context.

In fact, until the end of XX century and after the colonial era, SW Africa, namely Angola and Namibia, were severely affected by civil wars where most of the existing weather and hydrological stations were destroyed. As an example, over Angola, in 1974, at least 500 weather stations (WS) covered the entire country. By 2002 (when the Angolan civil war ended), only 7 WS remained operational (i.e., ~2% of initial WS) (Cain et al., 2015). Also, during the civil war period, observational "climate posts" available in Angola dropped from 225 in 1974, to zero in 2010 (Huntley et al., 2019). This lack of WS coverage over the region (either automatic or conventional) during the early 2000s, contrasts with the late 1960s, when the country had a significatively good WS coverage (Luetkemeier et al., 2018). As a result, nowadays, there is still a critical lack of climate data across SW Africa. Due to this, some funding programs (such as FRESAN), developed by external entities (mainly countries from the EU), have been investing in weather and climate recording over SW Africa, installing or repairing WS across those places. During the period of 2012-2016, a series of new WS were installed in southern Angola and northern Namibia regions by the scope of a program named "Southern African Science Service Centre for Climate Change and Adaptive Land Management" (or SASSCAL), managed and funded by Germany's Federal Ministry of Education and Research, in cooperation with the University of Hamburg and with local meteorological services, such as Angola's INAMET or Namibia's Meteorological Service (NMS) (Luetkemeier et al., 2018; Posada et al., 2016).

2.1. Weather stations data

As stated before, since 2012, a wide range of weather stations became operational in the SW African region as part of the SASSCAL program, enhancing the quality of WS network over the region. The WS network placed in Angolan territory is equipped with Austrian ADCON Telemetry® thermometers (at ~2[m] height), rain gauges, anemometers, and barometers, providing weather data (temperature, precipitation, relative humidity, surface pressure…) with good temporal resolutions (mainly hourly values). The Namibian WS network is similar, but the instruments used were delivered by the North American company R.M. Young®. The data is stored in a *data logger* placed in the WS, recording data over time, and reporting it through an antenna installed in the WS. The energy needed to send information from the *data logger* to the database is provided by solar panels. Even though this WS network is still scarce over the region, monthly precipitation data from 10 SSASCAL WS disposed over southern Angola and northern Namibia were used in this work, which added confidence to some of the obtained results with ERA5 reanalysis. Retrieved monthly data covered the period between the beginning of each station's data report and December 2020. Table 2.1 presents a list of 10 WS, its respective locations, altitudes, and temporal ranges. Figure 2.1 displays the exact location of the 10 WS in SW Africa. Figure 2.2a-c are pictures of some of these WS.

Table 2.1 - List of IDs, locations, coordinates, altitudes, and the respective dates these WS started reporting (beginning of timeseries), for each one of the 10 SASSCAL WS used in this work. To observe, in a map, the exact location of all WS, see Figure 2.1.

Station ID	Location	Geographic coordinates	Altitude [m]	Beginning of timeseries
31214	Omatako Ranch, Namibia	20.57ºS; 17.80ºE	1496	01/2012
31212	Ogongo, Namibia	17.67ºS; 15.29ºE	1111	02/2012
64243	Okapya, Namibia	17.65ºS; 15.46ºE	1138	02/2012
857336	Humpata, Angola	15.02ºS; 13.37ºE	1880	10/2014
857332	Bibala, Angola	14.76ºS; 13.36ºE	1061	10/2014
857331	Namibe, Angola	15.19ºS; 12.15ºE	11	10/2014
858128	Tundavala Observatory, Angola	14.81ºS; 13.40ºE	2300	03/2015
361101	Parque Nacional do Bicuar, Angola	15.36ºS; 14.76ºE	1243	03/2015
46943	Ondjiva, Angola	17.06ºS; 15.70ºE	1119	04/2015
74714	Okangwati, Namibia	17.43ºS; 13.27ºE	1081	04/2016

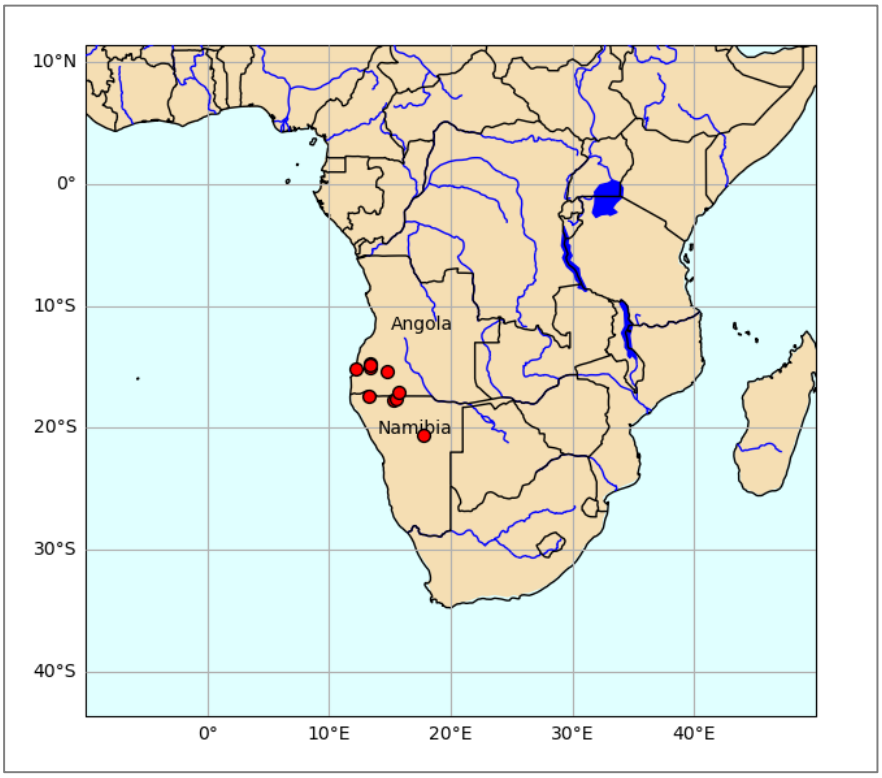

Figure 2.1 - Map of SW African subcontinent showing the locations of 10 SASSCAL WS (red dots) used in this thesis. These WS are scattered over southern Angola and northern Namibia and are part of a recent installed WS network in the region.

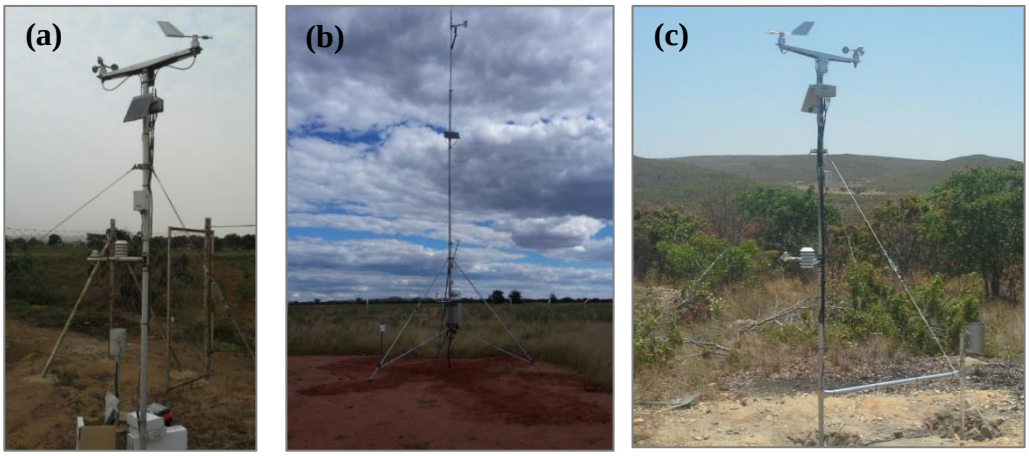

Figure 2.2 - Pictures of some of the SASSCAL project WS, whose data was retrieved and used in this work. These WS are placed in **(a)** Namibe, Angola; **(b)** Okangwati, Namibia; **(c)** Tundavala, Angola. Pictures source: SASSCAL project.

2.2. ERA5 reanalysis data for the subcontinent

To overcome the lack of WS records and weather profiles, monthly averaged data from ECMWF's most recent *state-of-the-art* reanalysis (ERA 5th generation or ERA5) was retrieved, either in single or in pressure levels, for the period of 1980-2020. In fact, ERA5 provides hourly data on various atmospheric, land-surface and sea-state parameters based on different observations, such as conventional WS, satellite data, or radiosondes, assimilated via a 4D-Var data assimilation scheme (C3S; Hersbach et al. 2020). The latter was developed under the Copernicus Climate Change Service (C3S) and replaces ERA-Interim reanalysis, which was progressively becoming outdated and completely stopped by end of August 2019 (Hersbach et al. 2020). ERA5 resolution is 0.25ºx0.25º (corresponding to, approximately, 30x30[km]). To better understand the rainfall drivers of SW Africa region, ERA5 data was used for the entire Southern African subcontinent, i.e., for the domain [10ºN-40ºS; 10ºW-50ºE]. Variables retrieved from ERA5, and its technical descriptions, are displayed in Table 2.2 for single levels and, in Table 2.3, for pressure levels.

Table 2.2 - Monthly averaged ERA5 retrieved variables (in single levels) for the period of 1980-2020 and its respective description and physical units.

Variable	Physical units	Resumed description
Integrated eastward and northward water vapour transport (IVT)	$\mathrm{kg \cdot m^{-1} \cdot s^{-1}}$	Horizontal flow of water vapour, per metre, for a column of air extending from the surface of the Earth to the top of the atmosphere.
Total precipitation	$\mathrm{mm \cdot day^{-1}}$	Accumulated liquid and frozen water (rain and snow), that falls to the Earth's surface. It is the sum of large-scale precipitation and convective precipitation.
Geopotential height at surface / Orography	$\mathrm{m^2 \cdot s^{-2}}$	Gravitational potential energy of a unit mass, at a particular location, relative to mean sea level. At the surface of the Earth, this parameter shows the variations in geopotential (height) of the surface and is often referred to as the orography.

Vertically integrated water vapour transport (IVT) retrieved from ERA5 is computed by integrating the product between specific humidity q and wind speed $\vec{V}$, from the surface of the Earth up until the top of the atmosphere (i.e., the sum of $q \cdot \vec{V}$, throughout 37 available pressure levels) (equation 2.1):

$$\mathrm{IVT} = \int_{p=1000[hPa]}^{p=1[hPa]} q_p \cdot \vec{V}_p \frac{dp}{g} \tag{2.1}$$

In equation 2.1, the subscript p refers to the pressure level, q_p stands for que specific humidity at the pressure level p, $\vec{V}_p$ is the wind speed vector. Its respective zonal and meridional components are hereafter referred to as $(\vec{u}_p; \vec{v}_p)$. Negative values of zonal IVT ($\mathrm{IVT_u}$) means a *westward* transport. Positive values of $\mathrm{IVT_u}$, stands for an *eastward* transport. Even though the IVT represents a vertical integration of all water vapour transport from the surface until the top of the atmosphere, most of the humidity is transported at lower levels in the troposphere ($\lesssim 700$[hPa]), i.e., approximately at the same

levels as the Zambezi and Limpopo LLJs. In this way, further ahead in this thesis and, to facilitate the analysis, IVT_u values are assumed to quantify the amount of water vapour transported across these valleys.

Table 2.3 – Monthly averaged ERA5 retrieved variables (in pressure levels) for the period of 1980-2020 and its respective description, physical units, and correspondent pressure level(s).

Variable	Physical units	Pressure level(s) [hPa]	Resumed description
u, v components of mean wind	$m \cdot s^{-1}$	1000-500	Horizontal speed of air, in metres per second.
Geopotential height	$m^2 \cdot s^{-2}$	800	Gravitational potential energy of a unit mass, at a particular location (in this case, 800 [hPa]), relative to mean sea level.
Specific humidity	$kg \cdot kg^{-1}$	1000-500	Mass of water vapour per kilogram of moist air.

Orography (Table 2.2) and geopotential height (Table 2.3) datasets were converted from [$m^2 \cdot s^{-2}$] to [m], by dividing the original dataset by g. To understand the dynamics of humidity within Zambezi and Limpopo river valleys, zonal specific humidity transport ($\dot{q_u}$) was computed using ERA5 monthly data for the subcontinent. Thus, by calculating the product between specific humidity (q) and zonal mean wind component (u), it was possible to perform cross-sections of $\dot{q_u}$ along both LLJs, as presented later in this work (section 3). Zonal specific humidity transport ($\dot{q_u}$) dataset was converted from [$kg \cdot kg^{-1} \cdot m \cdot s^{-1}$] to [$g \cdot g^{-1} \cdot m \cdot s^{-1}$], by multiplying the final dataset by 1000.

For some results and further analysis, hourly ERA5 data of u, v components of wind at 850 [hPa] were also retrieved for the period of 1980-2020, over the region of interest (SW Africa).

2.3. Searching methodology of local geopotential height minimums

The determination of the positions and intensities of the main Southern African synoptic low-pressure systems, over time, is essential to understand rainfall variability across the region of interest. In this work, as stated in the Introduction (subsection 1.3), AL and MCT represent the main low-pressure systems responsible for injecting moisture into the subcontinent and converting it into rainfall. As also described previously on section 1, AL and MCT systems are characterized, during the austral rainy season, as minimums of geopotential height over the regions where they usually form. Therefore, 1980-2020 ERA5 monthly geopotential height fields at 800[hPa] (gh800) were retrieved for areas where, typically, the centre of the AL and MCT are spotted, in order to determine both AL and MCT positions and intensities. The searching regions, for AL and MCT, were defined as, respectively, [7.5-22ºS; 10-25ºE] and [18-29ºS; 34-43ºE] - both represented, respectively, with a black and green square in Figure 2.3.

However, in some cases, gh800 absolute minimums did not correspond to the real position of the AL or the MCT, due to some local orographic effects that still affect the geopotential height field, even at

800[hPa]. This way, the algorithm tried to find the gh800 minimum on AL and MCT regions based on the average value of gh800 over a small 1ºx1º box (red box in Figure 2.3), surrounding the correspondent absolute gh800 minimum (pink stars in Figure 2.3). In other words, if the gh800 absolute minimum was an isolated value originated by local effects, it would be "diluted" on the average value of the small red box (surrounding values). Therefore, it would not be selected as an absolute minimum over the searching area, preventing misleading results. This condition was applied considering that the AL and MCT conserve, within the surroundings of its absolute minimum gh800 value, a close-to-minimum gh800 field.

As an example of this methodology, Figure 2.3 shows a map of gh800 field for February 2013, where gh800 local-minimum computations were performed, with the pink stars indicating the selected local minimums, representative of the location of the AL and the MCT. After testing this methodology for different fields of geopotential height (750, 800 and 850[hPa]) and generating several figures similar to Figure 2.3, the algorithm returns, on geopotential heights of 800 [hPa], minima locations that are more similar to those determined empirically (by visual inspection of the fields), probably due to the local mountain ranges effect on geopotential heights below this value (geopotential fields at heights below 800[hPa] become less smooth). The latter was an explanation for choosing 800[hPa] as an acceptable geopotential height field to study the region.

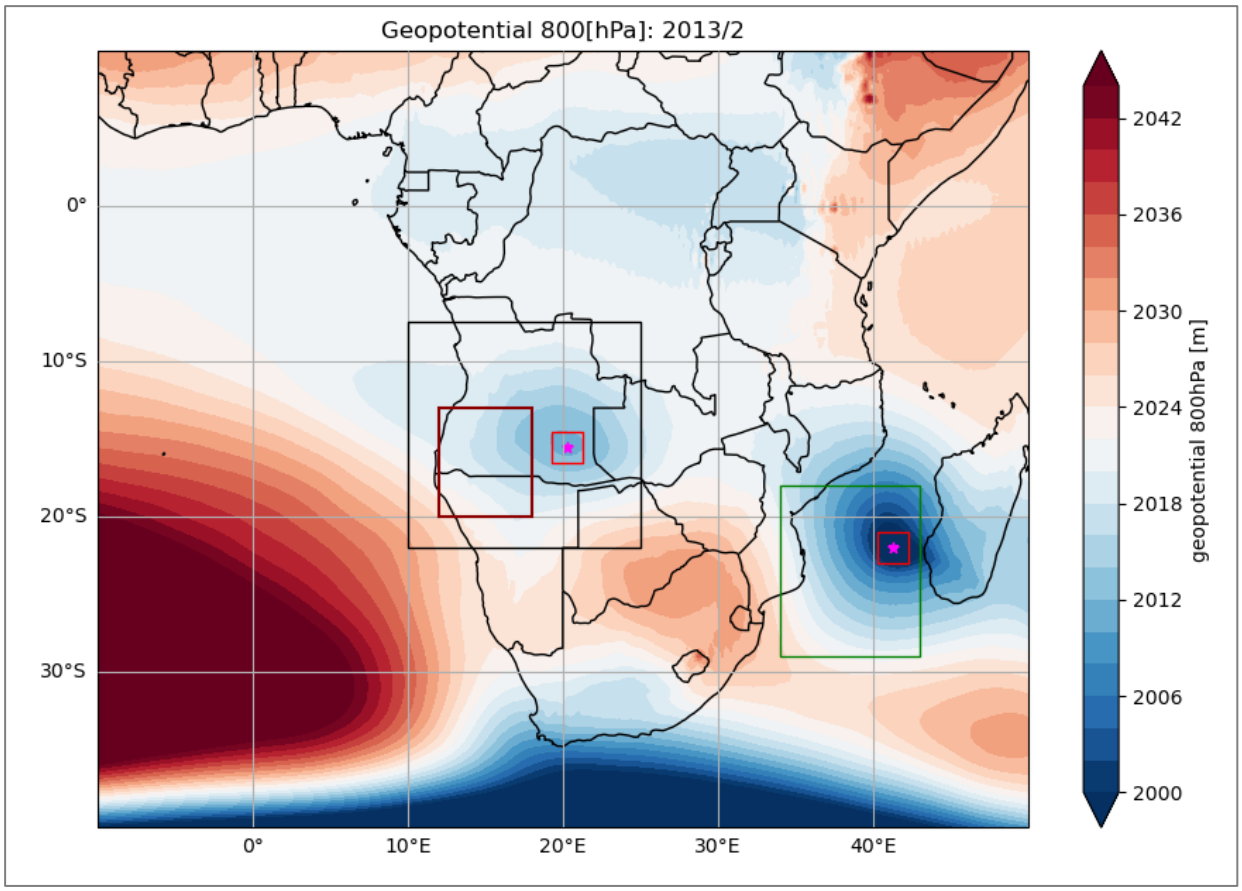

Figure 2.3 - Monthly mean of ERA5 geopotential height (at 800 [hPa]) over austral Africa in February 2013. Both pink stars indicate the selected local minimums representative of the AL and MCT. As described before, the pink star represents the location of the absolute gh800 minimum, and the red squared box surrounding it, stands for the surrounding area used to determine the average value of gh800 around the absolute minimum. The latter were used to define a searching criterion, to prevent local effects to interfere with the results. Local minima searching methodology was limited to 2 areas: the AL region,

represented by the dark square [7.5-22ºS; 10-25ºE,], and the MCT region, represented as the green box, whose domain is [18-29ºS; 34-43ºE]. Dark-red square indicates the region of interest of this thesis and corresponds to an area where ERA5 precipitation data was retrieved for the SW African rainfall analysis – the domain is [13-20ºS; 12-18ºE].

2.4. Statistics used

With the aim of understanding some temporal behaviours and relationships between variables, both data sources' variables (ERA5 reanalysis and WS) were evaluated using a few statistical parameters. One of those parameters is the Pearson correlation coefficient (also known as *R*), which explains how well data fits the linear relationship between the datasets under comparison. Thus, *R* is mathematically defined by the next equation (equation 2.2) and varies between -1 and 1:

$$R = \frac{\sum_0^i (x_i - \bar{x})(y_i - \bar{y})}{\sqrt{\sum_0^i (x_i - \bar{x})^2} \cdot \sqrt{\sum_0^i (y_i - \bar{y})^2}} \tag{2.2}$$

With (x_i, y_i) representing, respectively, the i^{th} element of the dataset x and y (with length i). $(\bar{x}, \bar{y})$ corresponds, respectively, to a pair of mean values of both x and y datasets.

Statistical significance of the obtained results was computed using a hypothesis testing named Student's t-test. As explained in Kim (2015), a Student's t-test is a type of statistical hypothesis test used to determine if there is a significant difference between the means of two groups (or samples). In this work, each t-test used only one sample to determine its significance, i.e., a one-sample t-test was performed. One-sample t-tests are often used to compare a sample mean to a specific value (Gerald, 2018). In this case, the targeted value is 0, as it represents a border between positive and negative anomalies. Therefore, it is important to verify if the sample mean differs from 0. This way, using this testing methodology, 95% confidence intervals were computed for each grid point of the precipitation anomaly composites over the Southern African subcontinent. Confidence intervals (CIs) were calculated via equation 2.3, where $\bar{x}$ corresponds to the sample mean, t_{95} stands for the t-test value associated with a 95% confidence level (retrieved from a pre-determined t-test table), s represents the sample standard deviation and n, the sample size (or length).

$$\mathrm{CI} = \bar{x} \pm t_{95} \frac{s}{\sqrt{n}} \tag{2.3}$$

Consequently, CIs containing 0 were considered non-significative (as the t-test could not guarantee a negative or positive anomaly over that sample location). Most of data samples used in this testing process, presented short lengths ($n < 52$), not favouring robust estimates of the standard deviation values. This fact justifies the use of a Student's t-test to compute the statistical confidence of the results (Wilks, 1995).

2.5. Data and computation of large-scale indexes: ENSO and SIOD

The key patterns of rainfall over the region of interest are generally influenced by the large-scale main modes of atmospheric variability. In the literature, two main sources of variability across Southern Africa that might influence rainfall patterns across the region have been identified: ENSO (El-Niño Southern Oscillation) and SIOD (Subtropical Indian Ocean Dipole) (Crétat et al., 2019; Hoell & Cheng, 2018; Reason, 2002).

In this work, an index to evaluate monthly ENSO phases was computed. This index was the Niño3.4 index, characterized by a 5-month running mean of SST anomalies over the most widely used region to evaluate ENSO - the Niño 3.4 region, defined as the area [5ºN-5ºS; 170ºW-120ºW] (see dark squared box in Figure 2.4). To define an El-Niño (La-Niña) year, 5-month running means of SST anomalies over the defined area need to be 0.4°C higher (lower) than the average (Trenberth, 1997). This way, when Niño3.4 index is higher (lower) than 0.4[ºC] (-0.4[ºC]), an El-Niño (La-Niña) phase of ENSO is happening. Niño3.4 index timeseries was determined using ERA5 SST monthly data, for the 1980-2020 period with respect to the 1981-2010 reference.

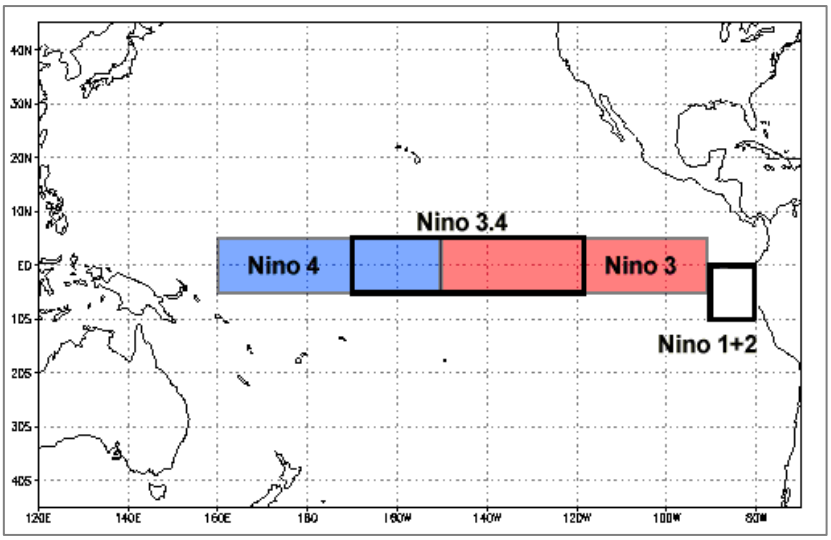

Figure 2.4 – Regions of equatorial Pacific Ocean used to perform ENSO indexes. In this work, Niño3.4 index was retrieved, based on the Niño3.4 region (dark squared box between Ninño4 and Niño3 regions). Figure source: NOAA/GCOS.

Similarly, SIOD indexes were also derived to complement the analysis. As previously mentioned, SIOD is one of the main Indian Ocean's modes of SST variability, being defined as the difference between SST anomalies from 2 distinct regions of the Indian Ocean: western ([27º-37ºS; 55º-65ºE]) and eastern ([18º-28ºS; 90º-100ºE]) (Behera & Yamagata, 2001). Both areas are represented as green squares in Figure 2.5. Positive (negative) SIOD indicated warmer (colder)-than-normal SSTs over the MC. Thus, similarly to Niño3.4, to compute the SIOD index, monthly averaged SST data from ERA5 was retrieved for both mentioned areas. After calculating monthly averaged anomalies of SST for both regions (with respect to the 1981-2010 normal), it was possible to compute the SIOD index timeseries, by subtracting, in each month, the average SST anomaly value between both regions, as it is explained by the equation 2.4:

$$\mathrm{SIOD_i} = \Delta\mathrm{SST_{i,west}} - \Delta\mathrm{SST_{i,east}};\ \Delta\mathrm{SST_i} = \mathrm{SST_i} - \overline{\mathrm{SST}} \qquad (2.4)$$

With $\Delta\mathrm{SST_i}$ representing the average SST anomaly during the month i (with respect to the climatology, $\overline{\mathrm{SST}}$). $\mathrm{SST_i}$ corresponds to the average value of SST for month i. $\mathrm{SIOD_i}$ stands for the average SIOD index over month i.

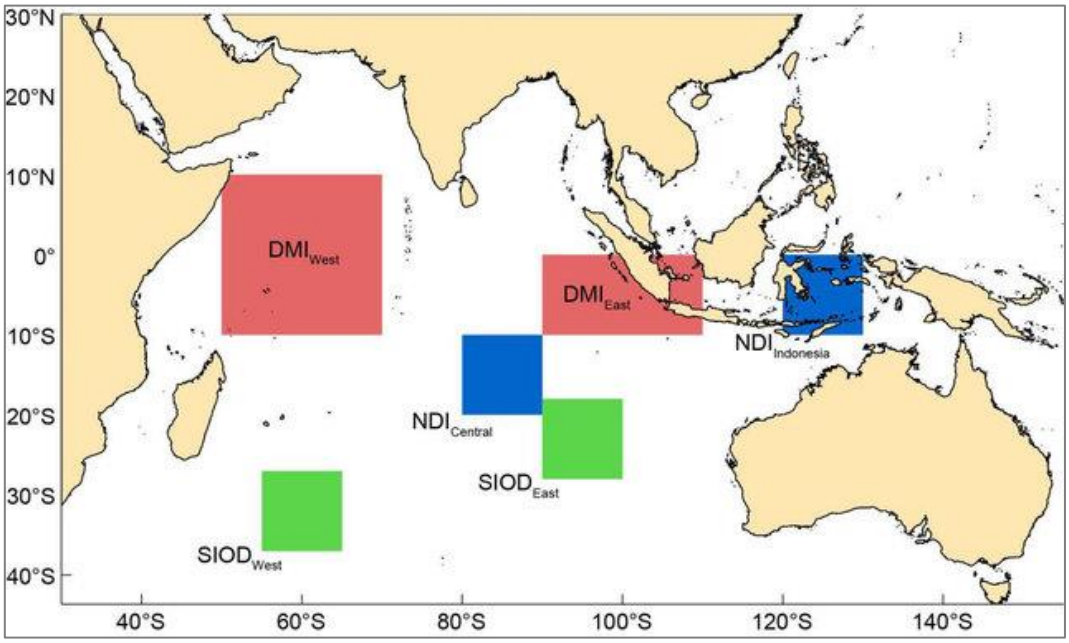

Figure 2.5 – Map of the Indian Ocean with 3 groups of boxes used to calculate large scale modes of variability of SST. Red and blue squares correspond to indexes and areas not contemplated in this thesis. Green squared boxes correspond to both west and east Indian Ocean regions used to compute the SIOD index. Figure source: Jaffrés et al. (2018).

3. Results and Discussion

This section presents an outcome of a research work aiming the study of moisture transport and rainfall over SW Africa, via atmospheric circulation mechanisms. As already explained in the Introduction of this thesis, weather features such as the AL, MCT and the LRV and ZRV low-level jets, play crucial roles on rainfall and moisture variability over the region of interest, located in SW Africa (dark-red square in Figure 2.3). Thus, the results are divided in the following way: first, a climatological analysis on both Zambezi and Limpopo LLJs and its relationship with moisture transport occurred over the subcontinent, was done. Then, the relevance of the AL, MCT and both LLJs on SW Africa rainfall was investigated. After that, the implications of large-scale variability patterns (e.g. ENSO - El-Niño Southern Oscillation; SIOD - Subtropical Indian Ocean Dipole) on these atmospheric features' dynamics and intensities, as well as on regional precipitation, were studied. To finalize, a synoptic analysis was performed on 2 case-studies of abnormally dry and wet rainy seasons over the study region. The discussion of the results was also presented along the subtopics of this section.

3.1. Moisture transport towards the Southern African subcontinent

As pointed out earlier (section 1), "invisible streams" of water vapour over the Limpopo and Zambezi river valleys are responsible for carrying high amounts of moisture towards the subcontinent – this enhances its importance on precipitation values across the region, including SW Africa. This way, along this subsection, a climatologic synoptic analysis was performed on both Zambezi and Limpopo river valley LLJs, to understand their mean spatial and temporal behaviour. As seen in Figure 3.1 and Figure 3.2, composites of 1980-2020 ERA5 monthly averaged data for vertically integrated water vapour transport (IVT) and zonal humidity transport (on pressure levels), respectively, over the rainy season (November to April), are presented. These months were selected as they represent the rainiest months of the year (as seen in precipitation climatologies for the region, shown in Figure 1.2).

It is possible to see that, in the beginning of this season (November), significant amounts of humidity from tropical Indian Ocean enter central and southern Africa via ZRV, primarily due to the induced circulation around the Mascarene HP. It becomes clear that, in early austral summer (December), as the latter decreases its intensity, conditions are created for the NE monsoon, along Somali coast, begin to inject high amounts of water vapour in ZRV and LRV. Then, all of this water ends up transported via both river-valley LLJs towards SW Africa (namely, southern Angola and northern Namibia) (see Figure 3.1a,b). As expected, during this period, an intense humidity transport activity in both river valleys is verified. This is expressed in the cross-sections of Figure 3.2 –a,b.

In January, NE monsoon reaches its maximum of IVT towards east Africa, however, as the ITCZ reaches its maximum southward seasonal shift, during this month, an intensification of the MCT west of Madagascar is observed, responsible for shifting most of the tropical NE monsoon humidity back to the Indian Ocean, not allowing it to pass through both river valleys. Nonetheless, ZRV and LRV receives humidity from an easterly flux of IVT produced by both Mascarene HP and MCT which, together with a dynamical adjustment induced by the presence of Madagascar topography, penetrates, south-easterly, through both river valleys (Figure 3.1c). Thus, Figure 3.2c shows, in January, a large westward flux of water vapour within the valleys, with LRV being the most efficient conveyor of humidity.

NE monsoon and the MCT starts to decrease its intensity by February, allowing moisture from tropical Indian Ocean being transported, again, towards eastern and central Africa mainly via ZRV (Figure 3.1d). However, LRV, mostly receiving humidity from the SE, still plays a major role on zonal humidity transport towards SW Africa (Figure 3.2d).

By March, the ITCZ begins its seasonal shift towards the equator. Figure 3.1e shows a pronounced easterly IVT from the Indian Ocean, still clashing with both ZRV and LRV south-easterly, due to the presence of Madagascar's landmass. In this month, Figure 3.2e illustrates that (contrary to January and February), zonal water vapour transport is higher in ZRV than in LRV. This reflects the meridional ascendence of the ITCZ by this time of year, as the ZRV is located further north than LRV.

During April, as the ITCZ continues its northward path, most of the easterly IVT advection happens north of Madagascar, mostly entering in ZRV, as the SW monsoon starts to appear, with southwesterly humidity transport off the coast of Somalia (Figure 3.1f). The cross-section in Figure 3.2f shows a significant decrease of westward humidity transport in LRV and a maintenance of the entrance of water vapour in ZRV. Throughout April and in the following months (not shown), higher amounts of zonal humidity transport migrate northward (tracking the ITCZ) and starts to enter in other associated orographic LLJs, north of ZRV.

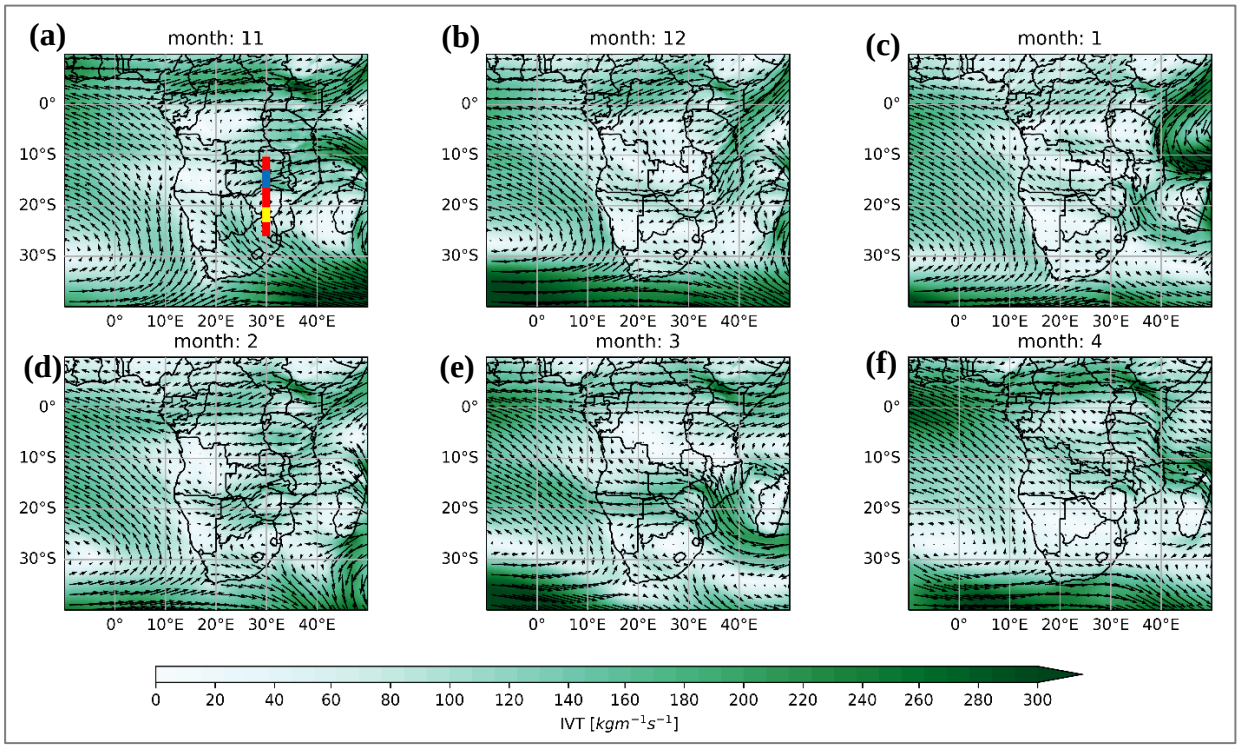

Figure 3.1 - Monthly averaged (1980-2020) integrated water vapour transport (IVT), retrieved from ERA5 reanalysis for the rainy season (November to April), over the south African subcontinent. Black quivers are spaced by 2ºx2º and represent the direction and magnitude of IVT. Shaded green colours also represent the magnitude value of IVT. Each panel (a to f) represent the following monthly sequence: **(a)** November, **(b)** December, **(c)** January, **(d)** February, **(e)** March and **(f)** April. On panel (a), the yellow line represents a meridional section of LRV and the blue line, of ZRV. The red line marks the place where the cross-sections presented in Figure 3.2 were made.

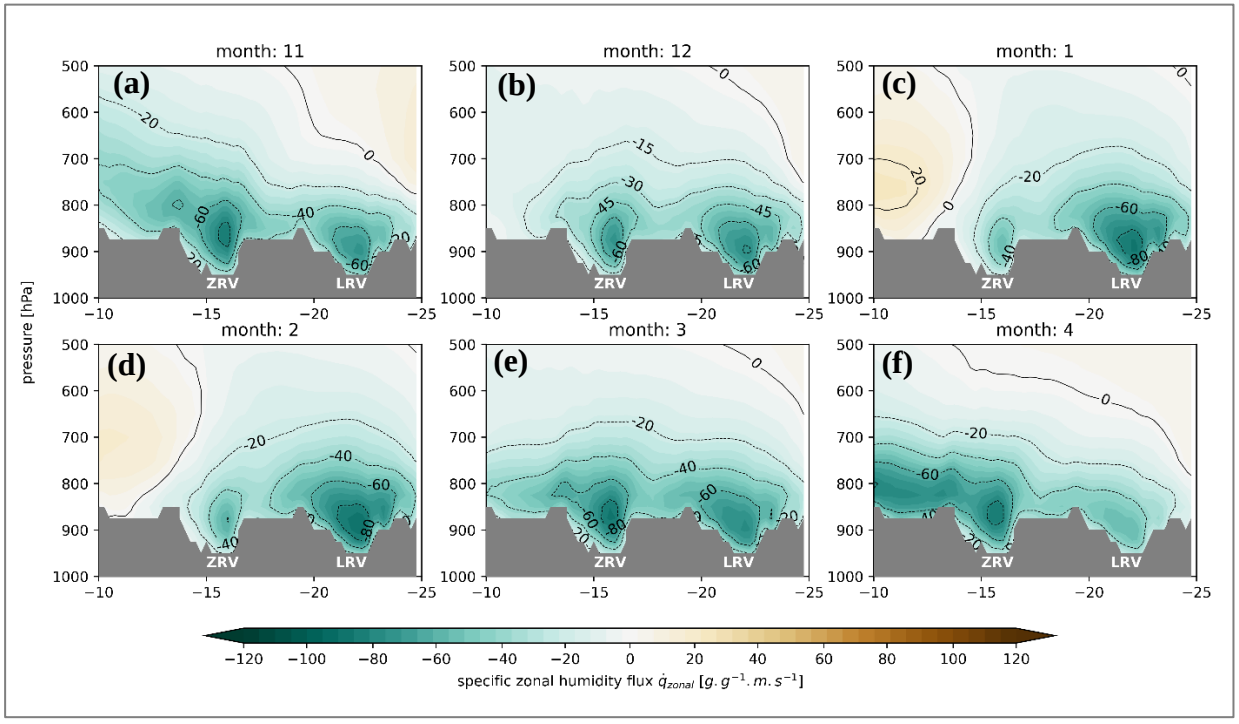

Figure 3.2 – Same as Figure 3.1, but for zonal specific humidity flux computed on pressure levels. The cross sections were made between 10ºS and 25ºS at a constant longitude of 30ºE (see the red line on Figure 3.1a). The *xx* axis in each panel correspond to latitude. Either Zambezi (ZRV) and Limpopo (LRV) river valleys are identified in the figure with white acronyms.

3.2. Impacts of Low-Level Jets from Limpopo and Zambezi river-valleys on regional rainfall

By the previous subsection, it became clear that LRV and ZRV play a fundamental role on moisture transport from the Indian Ocean towards central and western parts of Southern African subcontinent, essentially during austral summer. Now, it is important to comprehend the relationship between both LLJs water vapour transport and the precipitation occurred over SW Africa region (the region of interest for this work). To perform such analysis, as a first approach to this research, all the available rainfall data from 10 WS (from SASSCAL project), scattered over southern Angola and northern Namibia (as explained in subsection 2.1 of this thesis), were extracted. As also previously stated, SASSCAL WS started recording climate data between 2012 and 2016 (Table 2.1). However, out of 10 WS, solely 3 WS (placed in northern Namibia) started their time series in 2012. Recalling that, across southern Angola, SASSCAL project only installed WS during the year of 2014. For a higher consistency, available WS data since 2014 is considered (i.e., timeseries for all variables will start in January 2014 and finish in December 2020). To compare monthly precipitation data from all WS with Zambezi and Limpopo water vapour transports, zonal IVT (IVT_u) monthly data (from ERA5 reanalysis) was retrieved over a small meridional section in both river valley regions and its respective anomalies (with respect to a 1980-2010 normal) were plotted for the same period as WS data. Both meridional sections are represented in Figure 3.1a. Figure 3.3 displays the 2014-2020 monthly timeseries of all 10 WS rainfall (and its respective anomalies), as well as IVT_u anomalies from both Limpopo and Zambezi river-valley LLJs.

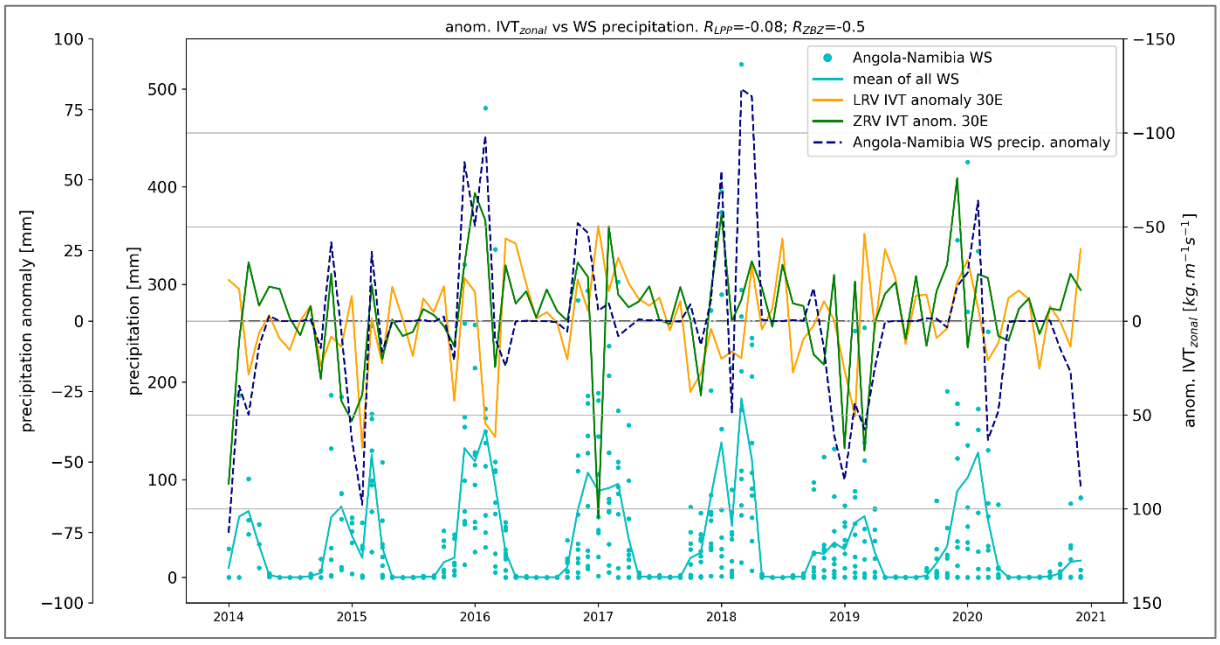

Figure 3.3 – Timeseries (January 2014 – December 2020) of ERA5 IVT_u and SASSCAL WS data. Every month, various cyan dots were plotted, each one representing a monthly rainfall value from a different WS. Cyan line stands for the average of all dot values within each month (i.e., indicates, in every month, the average precipitation of all WS). Dashed dark-blue line represents the monthly average WS rainfall anomalies (based on a 2014-2020 normal, due to the short WS timeseries). IVT_u anomalies (based on a 1980-2010 normal), were plotted as an average value for 2 sections at different locations, but at the same longitude of 30ºE: the LRV region [13ºS-17ºS] (orange line) and the ZRV region [20ºS-24ºS] (green line). Figure 3.1a marks the latter sections with a yellow (LRV) and blue lines (ZRV). Positive anomalies of IVT_u mean a more eastward (or less westward) moisture advection, and negative anomalies of IVT_u, represents a more westward (or less eastward) flux of water vapour. IVT_u anomaly axis is inverted for a clearer graphical visualization. Correlation values (see figure title), were performed between WS rainfall anomalies and IVT_u anomalies from LRV ($R_{LPP} = -0.08$) and ZRV ($R_{ZBZ} = -0.50$).

The time series of anomalies of rainfall and IVT_u over both river valleys (Figure 3.3) and its respective values of R ($R_{LPP} = -0.08$ and $R_{ZBZ} = -0.50$) shows that the ZRV water vapour flux anomaly can explain much better the variation of precipitation anomalies registered in the WS network (over southern Angola and northern Namibia), than the LRV. In fact, observing each temporal behaviour, it is possible to understand that the green line (anomalies of IVT_u in the ZRV) better fits the oscillations of the dashed dark-blue line (WS rainfall anomalies) than the orange line (anomalies of IVT_u in the LRV). However, the highest negative rainfall anomalies (2015 and 2019) were registered when both river valley recorded negative IVT_u anomalies. Above-normal precipitation was reported when both river valleys recorded positive IVT_u anomalies (e.g. 2020) or when ZRV had, uniquely, very high IVT_u values (well-above average; e.g. 2016).

As already stated, fluxes of air from the east, during the rainy season (austral summer), carry high amounts of humidity from the Indian Ocean (enhanced by LLJs from ZRV and LRV), an essential ingredient for rainfall to occur. Thus, it is expected, at a daily timescale, to experience wetter days when mean winds over SW Africa blow from the east (Indian Ocean) than when they blow from the west (Atlantic Ocean). To understand these dynamics of wet and dry days, during austral rainy season, according to mean wind direction, it was retrieved, for the region of interest, hourly ERA5 data of rainfall and mean wind components (u,v) (at 850[hPa]) for all 1980-2020 rainy seasons (NDJFM), and, after converting it to a daily timescale (i.e., ERA5 hourly data become ERA5 daily data), wind roses were produced to verify daily mean wind frequency distributions across the study region. Precipitation and wind data were retrieved for the dark-red area in Figure 2.3 (subsection 2.3). Each wind rose corresponds to one of 3 rainfall categories for each day, based on two precipitation percentiles (25^{th} and 75^{th}) calculated with respect to ERA5 1980-2020 daily data for the respective month (January, February, or March).

- A dry day presented daily precipitation values below the 25^{th} percentile (of the correspondent month).
- A normal day had daily precipitation values between the 25^{th} and 75^{th} percentiles.
- A wet day corresponded to daily precipitation values above the 75^{th} monthly percentile.

Figure 3.4 presents the obtained wind roses (with respect to the direction of the mean wind at 850[hPa]) for each 3 rainfall categories.

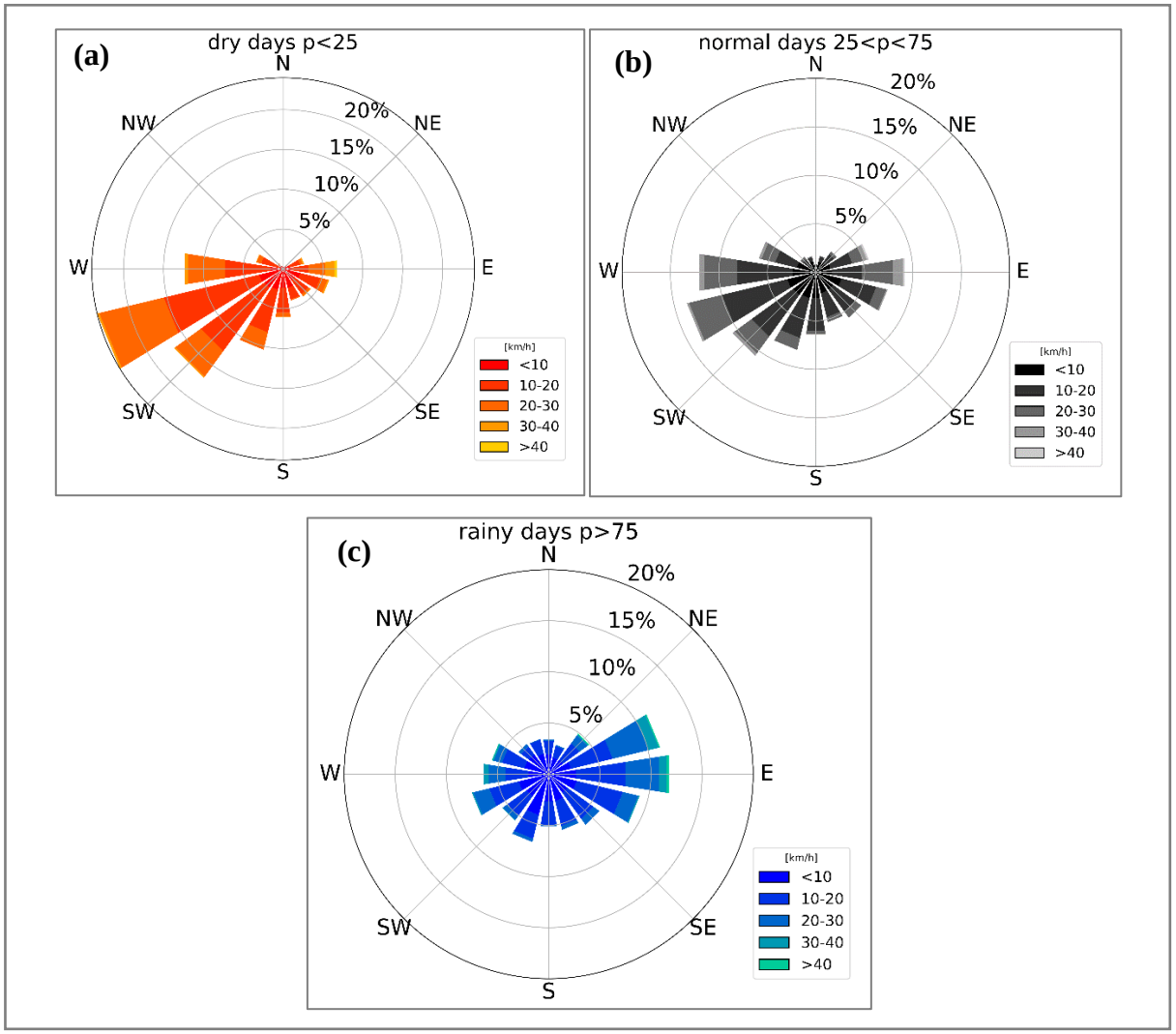

Figure 3.4 – Wind roses representing mean daily ERA5 wind data (850[hPa]) for each 1980-2020 NDJFM periods (over the region of interest – see red box in Figure 2.3). Each panel displays a wind rose that corresponds to **(a)** dry days (daily rainfall below the 25th percentile for the correspondent month), **(b)** normal days (daily rainfall between the 25th and 75th percentile) and **(c)** wet days (daily rainfall above the 75th percentile for the respective month). Percentages shown in the figure axis, correspond to wind speed frequencies, i.e., longer sectors represent higher frequencies of wind from that quadrant. Each sector is divided in 5 coloured wind speed intervals (displayed in the legend). The colour that matches a longer sector division, corresponds to the most frequent wind speed interval registered in the winds coming from that quadrant.

Looking at wind frequency distributions shown in the Figure 3.4, the existence of a prevalent east-west wind regimes is noticeable, with mean wind at 850[hPa] presenting, on average, either westward or eastward wind directions, rather than northward or southward directions (i.e., E or W sectors usually presents higher wind frequencies than N or S sectors). In fact, the latter figure shows a tendency for W and SW winds (from the Atlantic Ocean) to be associated with drier days (daily rainfall below the 25th percentile). Rainy days (daily values above the 75th percentile), are preferably linked with NE, E and SE wind regimes (i.e., winds mainly from the Indian Ocean). Days classified as "normal" (between 25th and 75th daily precipitation percentiles), typically have a southerly component, but are more related with W/SW wind directions than with easterly ones.

In fact, Figure 3.3 already gave an idea about the influence of both river valley LLJs in several locations across southern Angola and northern Namibia, however, a greater spatial view of the influence of both Limpopo and Zambezi river valleys on regional rainfall was equally important to achieve in this analysis.

In this way, monthly averaged data (from ERA5) of IVT_u and precipitation for austral Africa were used, covering the period of 1980-2020 and counting only with rainy season months (November to March). Using the 40-year-long IVT_u timeseries for both ZRV and LRV LLJs, the 25^{th} and the 75^{th} percentile (of this timeseries) were computed. Noting that any negative IVT_u value presented in both timeseries correspond to a westward water vapour transport, it is noteworthy that the lower the IVT_u value (i.e., more negative), the more efficient (stronger) the LLJ is on transporting water vapour towards SW Africa. Less negative (or positive) IVT_u values represent a weaker LLJ intensity (tendentially eastward) and, therefore, less capability on transporting water vapour to the region of interest. In this way, all the IVT_u values below (above) the 25^{th} (75^{th}) percentile were classified as strong (weak) LLJ months.

To comprehend the effects of stronger (or weaker) phases of Zambezi and Limpopo LLJ on rainfall across austral Africa (particularly over SW Africa), 4 composites of precipitation anomaly for the rainy season months (1980-2020) were determined, with respect of Limpopo and Zambezi LLJ intensity. Figure 3.5 shows these 4 composites for each one of the Zambezi and Limpopo LLJ phases.

Effectively, as displayed in Figure 3.5, on average, months associated with a weaker intensity of Zambezi LLJ, present well above-normal rainfalls over the MC region, namely central-eastern countries such as Botswana, Mozambique or Madagascar, which experienced positive precipitation anomalies, contrary to SW African regions, which registered, on average, direr conditions, with below-normal rainfalls (Figure 3.5a). The opposite state of the Zambezi LLJ, i.e., stronger phase (Figure 3.5b), indicates an inversion of the pattern showed in Figure 3.5a, with above-normal precipitation values observed across central-southern Angola and over the Namibian territory. Drier conditions appear over the east-coastal countries and MC region.

When observing the Limpopo LLJ intensity behaviour, it is possible to identify that weaker phases of this LLJ are not correlated with strong and statistically significative anomalies (either positive or negative) over austral Africa, however, it is possible to recognize below-normal anomalies in the northern parts of the MC and across SW Angola and Namibia (Figure 3.5c). Finally, as seen in Figure 3.5d, stronger Limpopo LLJ phases are linked with well above-normal rainfalls over central-eastern austral Africa and northern Madagascar. Statistically significative drier conditions appear over northern Angola and Democratic Republic of the Congo.

A timeseries of 40 years (1980-2020) of monthly anomalies of IVT_u values for ZRV and LRV was produced in the same way it was done in Figure 3.3 (i.e., using a mean anomaly value of IVT_u for the blue and yellow sections presented in Figure 3.1, representing, respectively, Zambezi and Limpopo LLJ) – this plot is presented in Figure 3.6, jointly with precipitation anomalies over the region of interest. In Figure 3.6a, it is verified that a stronger Zambezi LLJ (negative anomalies) is linked with above-normal rainfalls across the region of interest. The opposite situation is also observed, with months of a weaker Zambezi IVT_u (positive anomalies) being generally related with below-normal rainfalls across SW Africa. The correlation value between both timeseries was $R = -0.49$. Inspecting Figure 3.6b, even though it is not trivial to establish a clear relationship between weaker or stronger Limpopo LLJ states and SW African rainfall (lower R value, with $R = -0.19$), drier conditions across the region of interest seem to be sparsely linked with weaker Limpopo LLJ states.

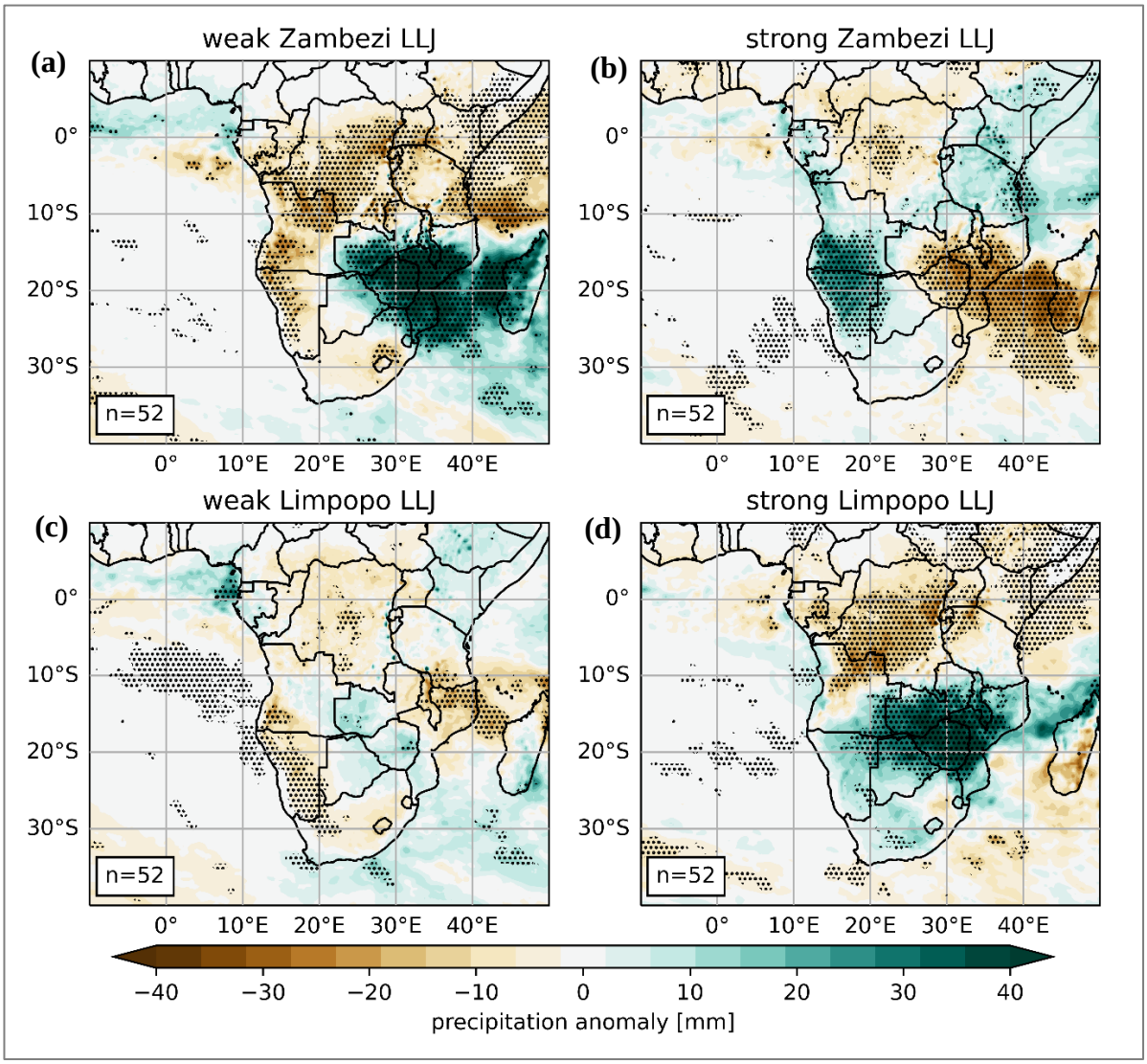

Figure 3.5 – Composites of ERA5 precipitation anomaly for all rainy season months of November, December, January, February and March (1980-2020), over the austral African subcontinent, that registered **(a)** weak Zambezi LLJ ($IVT_u > 75^{th}$ percentile), **(b)** strong Zambezi LLJ ($IVT_u < 25^{th}$ percentile), **(c)** weak Limpopo LLJ ($IVT_u > 75^{th}$ percentile) and **(d)** strong Limpopo LLJ ($IVT_u < 25^{th}$ percentile). Each panel (or composite) is computed by averaging all months that present the LLJ characteristics previously described. The number of months (*n*) used to compute the average is presented in the lower left of each panel. Precipitation anomalies were computed with respect to the 1980-2010 normal. Significant rainfall anomalies, using a Student's t-test for a 95% of confidence interval, are represented as dotted areas across each subplot (see subsection 2.4). IVT_u data was retrieved the same way it was done for plotting Figure 3.3 (i.e., using averaged values with respect of both sections presented in Figure 3.1a).

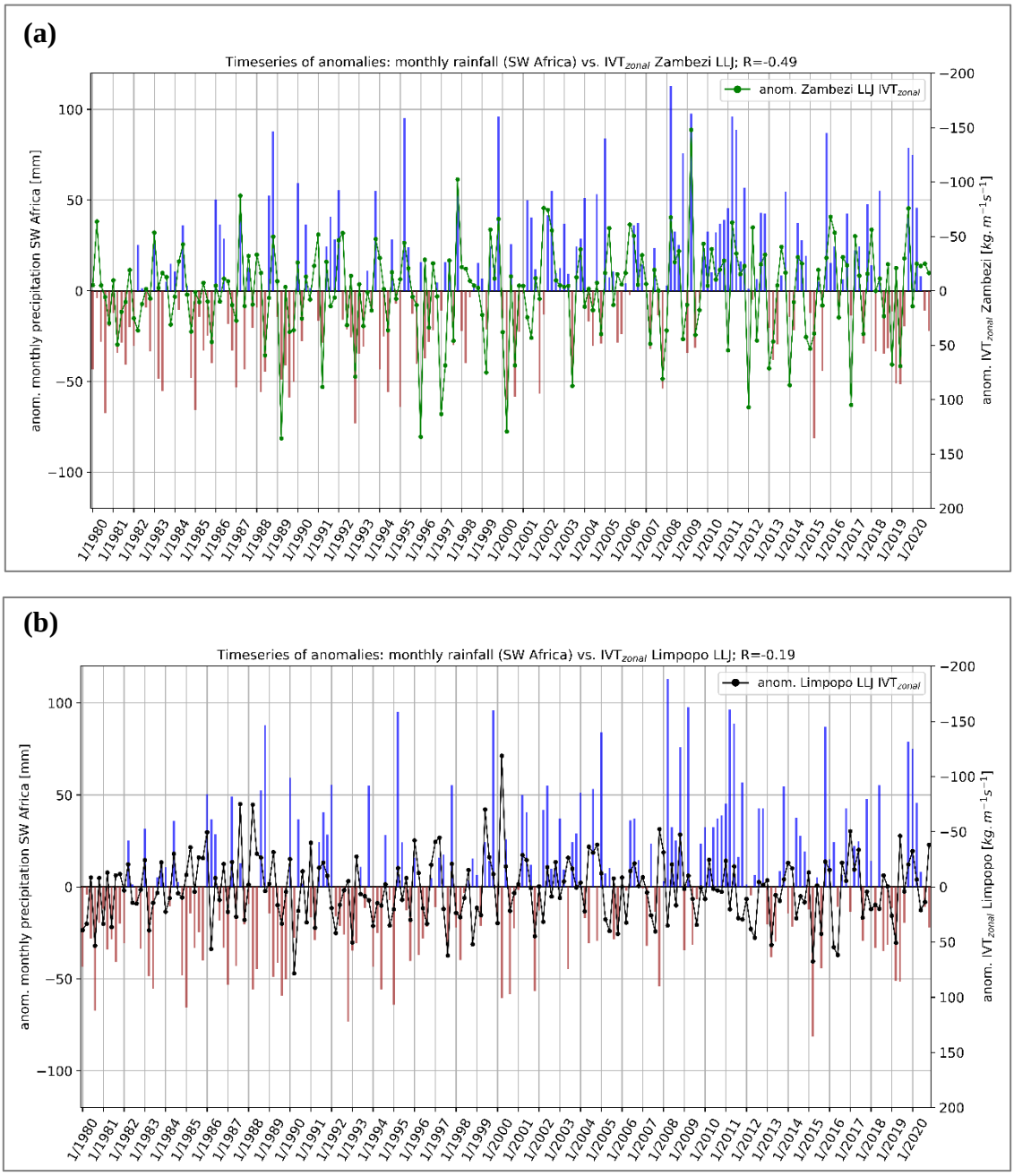

Figure 3.6 – Timeseries of rainfall anomalies (1980-2020) over the region of interest (see red box in Figure 2.3), versus IVT_u anomalies from **(a)** Zambezi LLJ and **(b)** Limpopo LLJ, all together, during the rainy seasons (NDJFM period). Blue bars represent months with positive rainfall anomalies and brown bars stand for below-normal precipitation months. Rainfall and IVT_u data were retrieved from ERA5. The Pearson-correlation value between ERA5 precipitation anomalies and Zambezi IVT_u was $R = -0.49$. Performing for Limpopo IVT_u, the result was $R = -0.19$. Precipitation anomalies were computed with respect to the 1980-2010 normal. IVT_u data was retrieved the same way it was done for plotting Figure 3.3 (i.e., using averaged values with respect of both sections presented in Figure 3.1a). Note that the right axis (IVT_u anomalies) is reversed for the sake of clarity, as done in Figure 3.3.

These results highlight the importance of both the Zambezi and Limpopo river valleys as essential drivers and distributors of water vapour across the subcontinent, including SW Africa. Through Figure 3.3, Figure 3.5 and Figure 3.6, it was possible to verify that, generally, when ZRV and LRV present weaker (stronger) IVT_u values, below (above) normal rainfall is registered over SW Africa, either if ERA5 or WS data are used. Nonetheless, in Figure 3.3, better R values were computed between ZRV

IVT_u anomalies and WS precipitation anomalies ($R = -0.58$), than when compared with LRV IVT_u ($R = -0.08$). In Figure 3.5, the composite of precipitation anomalies using ZRV LLJ, present stronger signals over the region of interest and, in Figure 3.6, 1980-2020 timeseries of ZRV LLJ anomalies is better correlated with rainfall anomalies over the study region ($R = -0.49$), than LRV LLJ ($R = -0.19$). Such results might indicate that ZRV LLJ plays a major role on SW African rainfall, even though the influence of LRV LLJ on such precipitation variability should not be discarded, as it is able to enhance or reduce the amount of available moisture across those regions and, as well, intensify (or weaken) drought (or flooding) events.

Verifying precipitation anomaly trends across the timeseries of Figure 3.6, a slight tendency for rainfall increases across the region of interest is noticeable. Part of this region is located over a region of complex topography, which, accordingly to Thoithi et al. (2021), plays a key role on enhancing rainfall gradients across the region (i.e., it can exacerbate wetter or drier conditions). Later in subsections 3.3 and 3.4, it will be possible to confirm that most of rainfall anomalies (either negative or positive), across western parts of Angola, match the existent orography.

From SW Africa perspective, and as demonstrated by Figure 3.4, a strong relation exists between easterly mean winds (i.e., air movements from the interior of the subcontinent, as well from the Indian Ocean) and above-average rainfalls across the region. When mean winds have a strong westerly component (i.e., when they come from the Atlantic Ocean), below-normal precipitations are usually recorded. In addition, even though it does not represent exact scientific evidence, it is interesting to refer some testimonies of local native populations from southern Angola, which reported, by experience, drier days when the wind was blowing from the west, and rainy days when the wind was moving from the east (see pictures of this interaction, on the scope of FRESAN project, in subsection 6.3 – Figure 6.3 and Figure 6.4). These reports match the results of Figure 3.4. Altogether, these results can prove the importance of the wind direction on rainfalls over SW Africa, as they are responsible for transporting humidity, specially form the Indian Ocean, via both LRV and ZRV, yet the latter seem to detain a major importance on precipitations over the region.

3.3. The influence of the Angola Low and the Mozambique Channel Trough intensities, on precipitations across Southern Africa

Regardless of the importance of the LLJs on regional rainfall across the Southern Africa, both AL and MCT are the main synoptic drivers of mean winds over the subcontinent, together with both HP systems (Mascarene and St. Helena). Therefore, as previously argued, the effects of the MCT and AL cannot be discarded, as both systems play a key role on converting humidity to rainfall, as well as generating circulation patterns that might be favourable (or not) to the strength of water vapour transport within both river valleys. To analyse the effects of the intensity of the AL and the MCT on the strength of both Zambezi and Limpopo LLJs, a timeseries of geopotential height at 800[hPa] (gh800) for both AL and MCT were retrieved, with respect to rainy season months (November to March). To obtain AL and MCT gh800 data, the local-minimum searching methodology (described in subsection 2.3) was performed.

Using both timeseries of AL and MCT gh800, it was possible to perceive both systems' intensity and its relationship with ZRV and LRV LLJs capacity of water vapour transport. To perform a study under such association between these atmospheric systems, scatter plots of AL and MCT gh800 versus ZRV and LRV IVT_u were produced and displayed in Figure 3.7. In order to join precipitation variable to this analysis, each scatter point was coloured according to the percentile threshold of precipitation occurred over the region of interest (dark-red square in Figure 2.3).

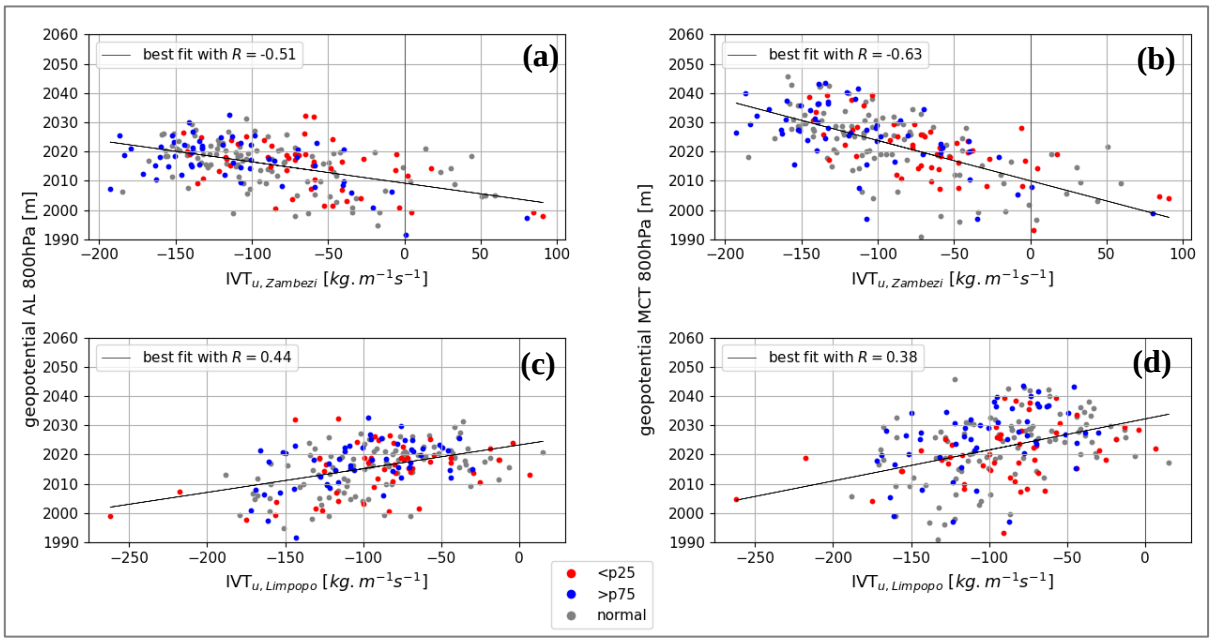

Figure 3.7 – Scatter plots of 1980-2020 rainy season months (November to March) geopotential height at 800[hPa] (gh800) for AL and MCT versus both Limpopo and Zambezi IVT_u intensities. Respectively, in each panel, it is shown **(a)** gh800 AL vs. Zambezi IVT_u; **(b)** gh800 MCT vs. Zambezi IVT_u; **(c)** gh800 AL vs. Limpopo IVT_u and **(d)** gh800 MCT vs. Limpopo IVT_u. Geopotential, rainfall and IVT_u data were retrieved from ERA5. Coloured dots indicate if the correspondent month (of each dot) was rainy, normal, or dry. To do this analysis, the 25th and 75th percentiles were computed for each month. Months with values of precipitation >75th percentile, were classified as rainy (blue dots); <25th percentile were classified as dry (red dots) and months with rainfall between the 25th and 75th percentile represented normal months (grey dots). The black line present in each panel corresponds to a linear regression performed using all the dots, being associated with a correlation (R) value displayed in the legend of each graph. Values of gh800 for the AL and MCT were computed via local minima searching methodology presented in subsection 2.3. Rainfall data corresponds to an average over the region of interest (dark-red square in Figure 2.3).

This way, inspecting Figure 3.7 and looking at correlation values (R), it is clear that Limpopo LLJ is less associated with both low-pressure systems (AL and MCT) than the Zambezi LLJ. Limpopo LLJ shows weak positive R values when correlated with gh800 values of AL ($R = 0.44$) or MCT ($R = 0.38$) – see Figure 3.7c,d. Zambezi LLJ is generally anticorrelated with both AL ($R = -0.51$) and MCT gh800 ($R = -0.63$) – see Figure 3.7a,b.

Dynamically, as shown in Figure 3.7a, the weaker the AL state (i.e., higher gh800), the stronger the Zambezi LLJ. As seen by the distribution of the coloured dots, when the AL presents a weaker state and the ZRV transport of humidity is strong and effective, the rainfalls over SW Africa are, generally, higher-than-normal. When the opposite situation occurs, i.e., when the AL is at a stronger state (lower gh800) and the Zambezi LLJ weakens (even though the distribution of red dots is not very clear), it seems to exist a tendency for drier conditions across the region of interest.

Figure 3.7b compares the MCT intensity with the Zambezi LLJ strength. The result showed the best anticorrelation of all panels of Figure 3.7 (with $R = -0.63$), indicating that, usually, weakening of the MCT (higher gh800) is followed by a strengthening of the water vapour transport (IVT_u) through the ZRV, contributing to above-normal rainfall months over SW Africa (as seen by the coloured dots). When the opposite situation occurs, a reduction of blue dots and the prevalence of red dots (i.e., drier conditions across the region of interest), is seen. These results show that the MCT and the AL control

ZRV LLJ intensity, with acceptably good anticorrelations, i.e., weaker (stronger) AL and MCT phases seem to be related with stronger (weaker) westward IVT_u in the Zambezi LLJ.

When investigating the effects of the AL and the MCT on Limpopo LLJ, the result is not so clear as it happens with the Zambezi LLJ (as reflected by the relatively lower absolute R values). Analysing Figure 3.7c,d, some tendencies for a strengthening of the Limpopo LLJ as both the AL and the MCT strengthen are apparent. However, when looking at the distribution of the coloured dots, generally, a division (by the regression line) between rainy and drier months is observed. This allowed to confirm the previous results shown in both Figure 3.3 and Figure 3.5, where ZRV seem to present a higher importance on humidity transport over the subcontinent, reflecting higher amounts of rainfall across the SW African areas.

Although the previous results illustrated the role of the AL and the MCT as key drivers of both Zambezi and Limpopo LLJs, spatial coverage of its influence on regional rainfall remained unknown. Thus, the same rainfall analysis done using the strength of Zambezi and Limpopo LLJs (Figure 3.5) was performed, but this time, applied to the strength of the AL and MCT. Both systems' gh800 timeseries were retrieved and computed the same way it was done previously (to construct Figure 3.7), with the AL and the MCT being classified as "strong" when gh800 values were below the 25th percentile (lower values of gh800) and "weak" when these values were above the 75th percentile (higher values of gh800). Hence, using ERA5 rainfall anomalies for the Southern African subcontinent (1980-2020) and selecting the rainy season months with "strong" or "weak" AL and MCT, it was possible to construct a figure with 4 averaged composites of precipitation anomalies for austral Africa (each one for each classification of the AL and MCT, as seen in Figure 3.8).

According to Figure 3.8a, when MCT presents higher gh800 values (i.e., MCT is in a weaker state), above normal precipitation values are registered across coastal areas of Angola, including the entire southern region, as well as over northern Namibia and central parts of the subcontinent (Figure 3.8a). In fact, weaker MCT states promote anomalous anticyclonic circulations over the MC, enhancing humidity transports via ZRV LLJ, towards SW Africa. Also, the incapability of a weaker MCT to convert humidity in rainfall, promotes the conservation of most of water vapour from Indian Ocean, which ends up being advected towards SW Africa and allowing higher amounts of available humidity in the atmosphere, an important ingredient for precipitations to occur over the region. Weak MCT phases are also associated with less convective processes and, consequently, below normal rainfalls over the MC region occur.

The opposite state of the MCT (stronger phase) is associated with the opposite rainfall pattern: wetter conditions over the MC region and drier spells across SW Africa (but mainly not statistically significative) and over Congo region (Figure 3.8b). Stronger MCT states are associated with anomalous cyclonic dynamics over the MC. This flow pattern shifts the oceanic water vapor away from the subcontinent. Thus, small amounts of humidity enter both LLJs, promoting fewer moisture transport and, consequently, less rain over SW Africa.

Looking at the effects of AL intensity on rainfall over the subcontinent, it is possible to note, on Figure 3.8c, that weaker AL phases are related with well above-normal precipitations across Angolan coastal regions and drier conditions over the entire central and southern regions of the subcontinent, with high statistical confidence. This result might be justified by a tendency of weaker AL states to be related to northward latitudinal shifts of this low-pressure system, allowing moisture to be advected towards Angola (discussed later, in subsection 3.4).

The opposite AL state (stronger) relates to an opposite precipitation anomaly scenario: wet spells over central Southern Africa and northern Namibia, as well as drier periods across the Angolan coastal strip (including the southern region), as seen in Figure 3.8d. This might also be justified by the tendency of stronger AL states to be related with southward shifts of this system, not allowing humidity to be advected towards western Angola, but towards central Namibia. Tendencies between AL intensity and its meridional movements are explored, later, in subsection 3.4, where a coherent relationship was found between northward (southward) shifts of the AL and its weaker (stronger) intensity.

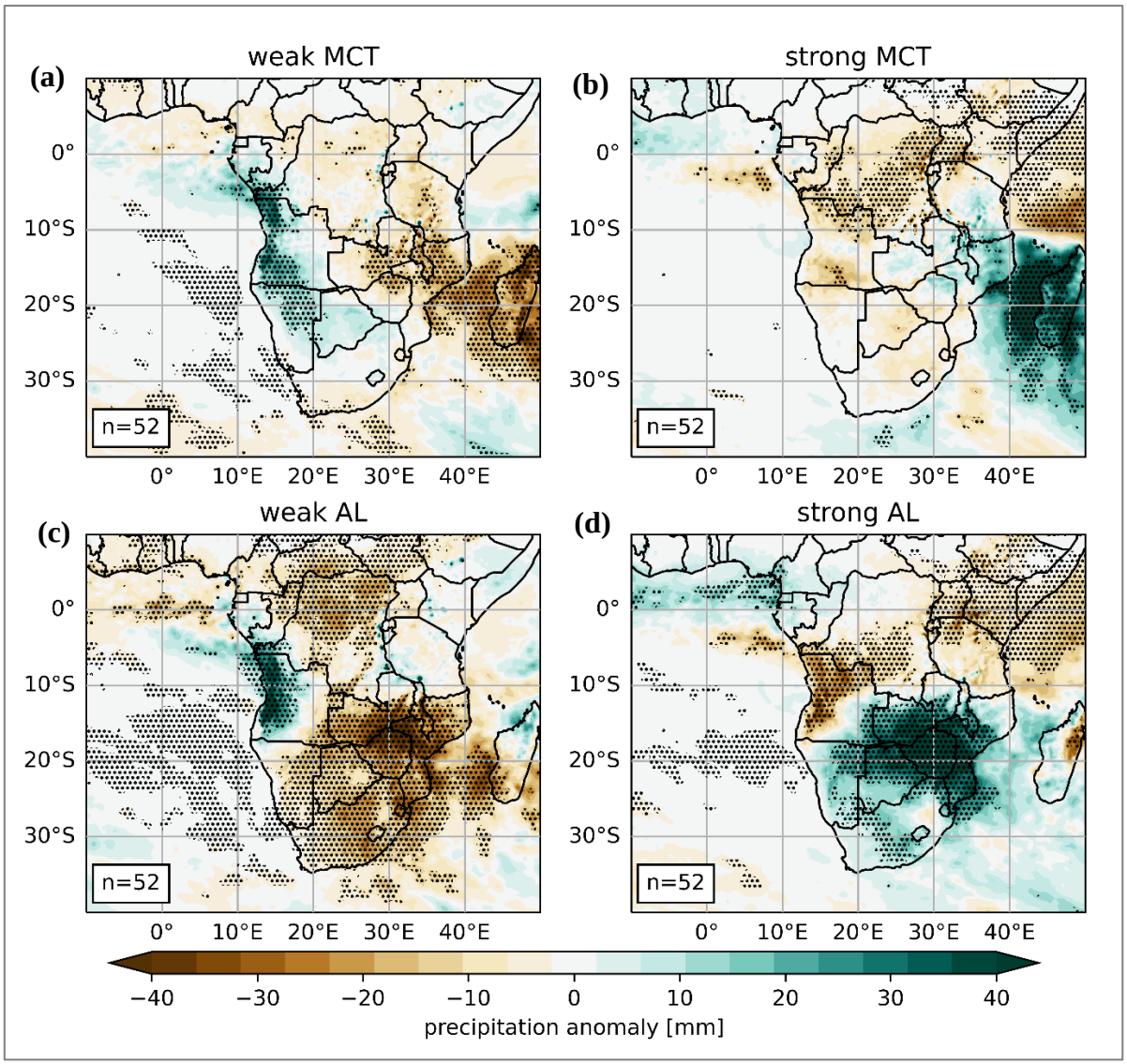

Figure 3.8 - Same as Figure 3.5, but for rainy season months that registered **(a)** weak MCT (gh800 MCT > 75th percentile), **(b)** strong MCT (gh800 MCT < 25th percentile), **(c)** weak AL (gh800 > 75th percentile) and **(d)** strong AL (gh800 < 25th percentile). Values of gh800 for the AL and MCT were computed via local minima searching methodology presented in subsection 2.3. Rainfall data corresponds to an average over the region of interest (dark-red square in Figure 2.3). The number of months (*n*) used to compute the average is presented in the lower left of each panel. Precipitation anomalies were computed with respect to the 1980-2010 normal. Significant rainfall anomalies, using a Student's t-test for a 95% of confidence interval, are represented as dotted areas across each subplot (see subsection 2.4).

The result showed in Figure 3.8 converges with Barimalala et al. (2019) findings, which showed that weaker (stronger) MCTs were related with above (below) normal rainfalls over SW Africa. In fact, below normal rainfalls over the MCT region usually happens when the MCT is in a weaker state (Figure 3.8a). In addition, inspecting Figure 3.8c, it is possible to see weaker AL states linked with below-normal precipitations over the MC, suggesting that weaker MCT states are somehow related with weaker AL phases. This is confirmed by the result in Figure 3.9, where weaker (stronger) MCT states tend to be associated with weaker (stronger) AL phases, i.e., different phases of AL and MCT are not common. This relationship between AL and MCT gh800 intensities present a relatively good correlation value of $R = 0.63$.

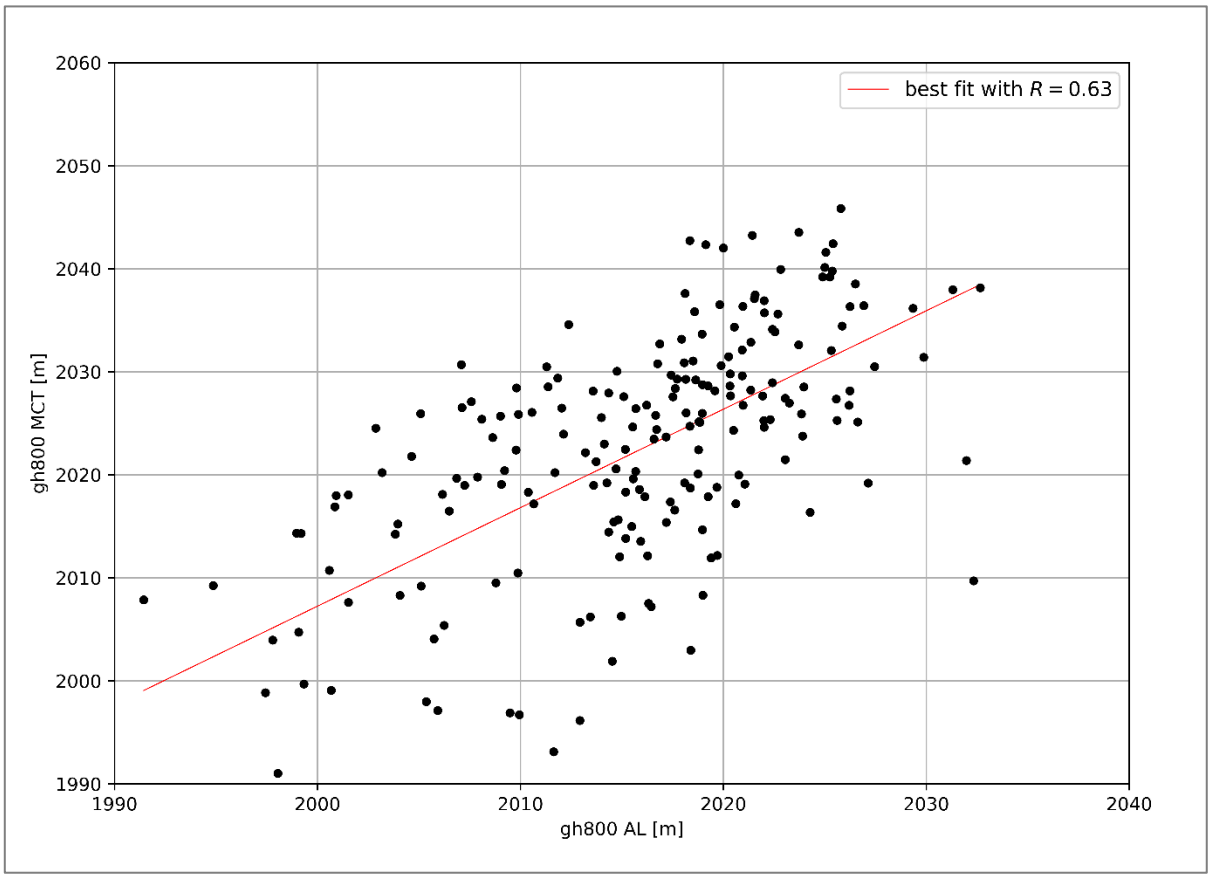

Figure 3.9 - Scatter plot of 1980-2020 rainy season months (November to March) of AL vs. MCT gh800 (ERA5). Red line indicates the correspondent regression line.

The result presented is in line with Munday & Washington (2017), which concluded that weaker AL states were related with weaker MCT phases. However, Barimalala et al. (2019) and Pascale et al. (2019) ended up concluding a different MCT vs. AL relationship, suggesting that weaker MCT phases were associated with stronger AL states. The discussion regarding this contrast of results is still underway, even though these authors identified constraints in the models used to sustain their conclusions. While it was shown that *state-of-the-art* models (i.e., those from CMIP5) used by Munday & Washington (2017) did not provide a realistic representation of the MCT, Barimalala et al. (2019) and Pascale et al. (2019) based their conclusions on simulations from idealized regional models.

Although the relationship between both AL and MCT intensities and its respective influence on rainfall over Southern Africa, are still a matter of scientific debate, composites of precipitation anomalies (similar to what was done in Figure 3.5 and Figure 3.8), were performed accordingly to the results of Figure 3.9. This way, 2 composites of rainfall anomalies were computed with respect to the 2 most-common conjugations of AL vs MCT phases, i.e., weaker AL states jointly with weaker MCT states, and stronger AL phases jointly with stronger MCT phases. Figure 3.10 displays these composites.

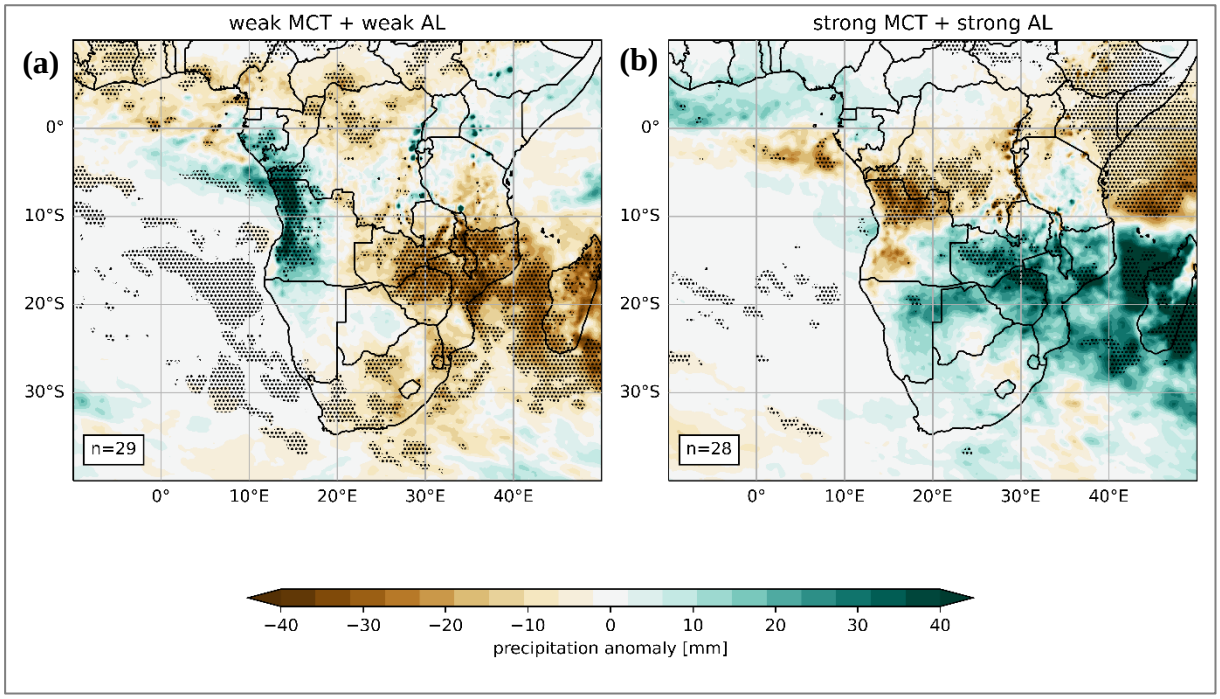

Figure 3.10 - Same as Figure 3.5, but for rainy season months that registered a conjugation of **(a)** weak MCT (gh800 MCT > 75th percentile) and weak AL (gh800 > 75th percentile); **(b)** strong MCT (gh800 MCT > 75th percentile) and strong AL (gh800 < 25th percentile).

In fact, as Figure 3.10 suggests, conjugations of both weaker (stronger) AL and MCT are related with above (below) normal rainfalls over the region of interest. As previously discussed, weaker MCT states promote larger moisture transport, from Indian Ocean, via Zambezi LLJ. Weaker AL states are related with northward shifts of the AL and vice-versa (explored in subsection 3.4). This conjugation allows humidity, mostly carried out by Zambezi LLJ, to reach southern Angola and produce above-normal rainfalls (Figure 3.10a), either via synoptic or orographic mechanisms.

The opposite situation (shown in Figure 3.10b), illustrates drier conditions across the region of interest, however, caution is needed due to the lack of statistical confidence. The registered pattern might be related to the intensification of the MCT, which promotes an abnormally cyclonic circulation in the MC, not allowing humidity to be advected towards SW Africa. This situation, jointly with a southward AL that shifts most of humidity towards central Namibia, promotes below-normal rainfalls over southern Angola.

To verify the temporal behaviour of both AL and MCT states along the previous 40 years (1980-2020), a timeseries of ERA5 gh800 anomalies for both low-pressure systems was plotted, alongside with rainfall anomalies over the region of interest. Positive (negative) gh800 anomalies relates with weaker

(stronger) AL and MCT. The result can be seen in Figure 3.11, with AL and MCT gh800 anomaly signals generally following each other. The latter shows that ERA5 provides a similar relation between AL and MCT intensities as the one described by Munday & Washington (2017) (i.e., tendentially, both systems are weak or strong). It is also notable that, through Figure 3.11, stronger AL and MCT are related with drier rainy season periods (e.g. 1989-90, 1996-97 or 2000-01 periods). Weaker AL and MCT are related with wetter rainy seasons (e.g. 1991-92, 2001-02 or 2016-17).

Nonetheless, some rainy seasons fail to match the AL vs. MCT gh800 relationship, such as the rainy seasons of 2010/11 (both strong AL and MCT produced well above-average rainfalls) and 2018/19 (with different MCT and AL phases inducing a very dry spell). Moreover, Hoell & Cheng (2018) found wet extremes across the subcontinent related with an anomalous lower-tropospheric cyclonic dynamics, forced by large-scale variability, increasing convergence and moisture fluxes over the region. This explains the exceptional rainfall season of 2010/11, where widespread areas of negative gh800 anomalies were found across Southern Africa. Both 2010/11 and 2018/19 exceptional rainy seasons (very wet and very dry, respectively), are studied, in detail, in subsection 3.5.

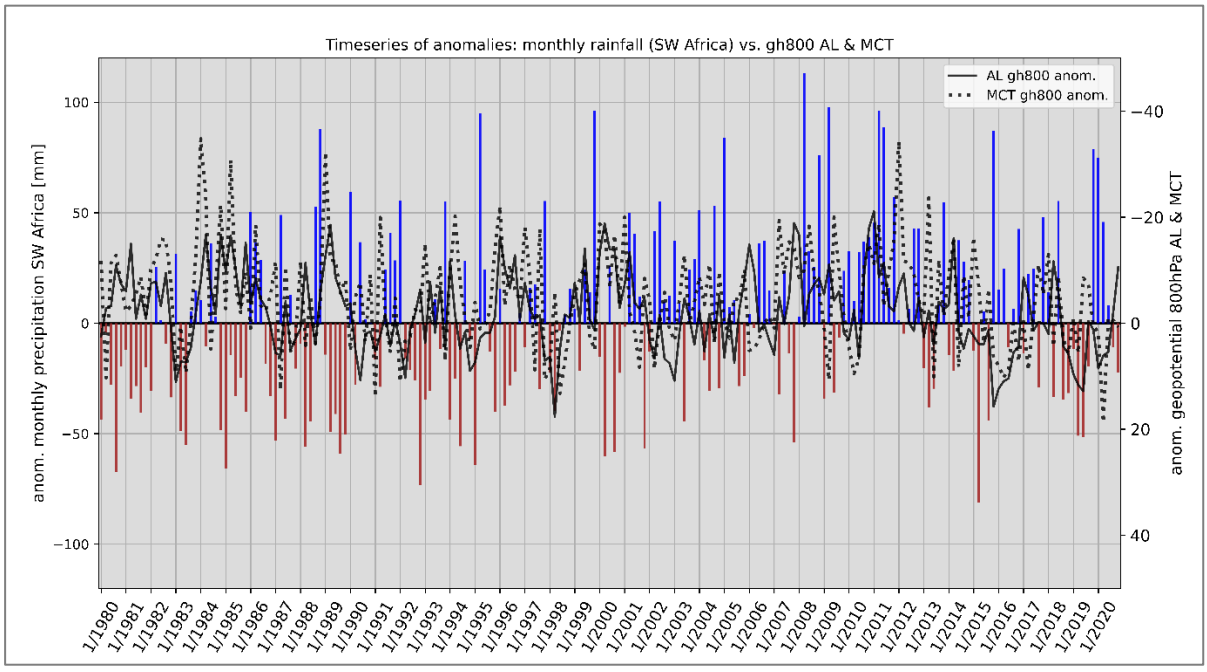

Figure 3.11 - Timeseries of ERA5 anomalies (1980-2020) of rainfall over the region of interest (see red box in Figure 2.3), versus ERA5 gh800 anomalies of AL (black line) and MCT (dotted black line), during the rainy seasons (NDJFM periods). Blue bars represent months with positive rainfall anomalies and brown bars stand for below-normal precipitation months Precipitation and gh800 anomalies were computed with respect to the 1980-2010 normal. Geopotential heigh anomalies (gh800) were computed according to the local-minimum searching methodology, presented in subsection 2.3. Note that the right axis of the figure was inverted for a better data visualisation.

To finalize and summarize the influence of both Zambezi and Limpopo LLJs, as well as both low-pressure systems (AL and MCT) on regional rainfall across Southern Africa, monthly distributions and climatologies of the analysed variables were computed for the 1980-2020 period, using ERA5 monthly data. In Figure 3.12, a plot of monthly rainfall distributions (over the region of interest) and IVT_u for both Zambezi and Limpopo LLJs, together with monthly climatologies of gh800 for both AL and MCT, is shown. This allows to characterize most of the weather features responsible for producing rainfall across South African subcontinent.

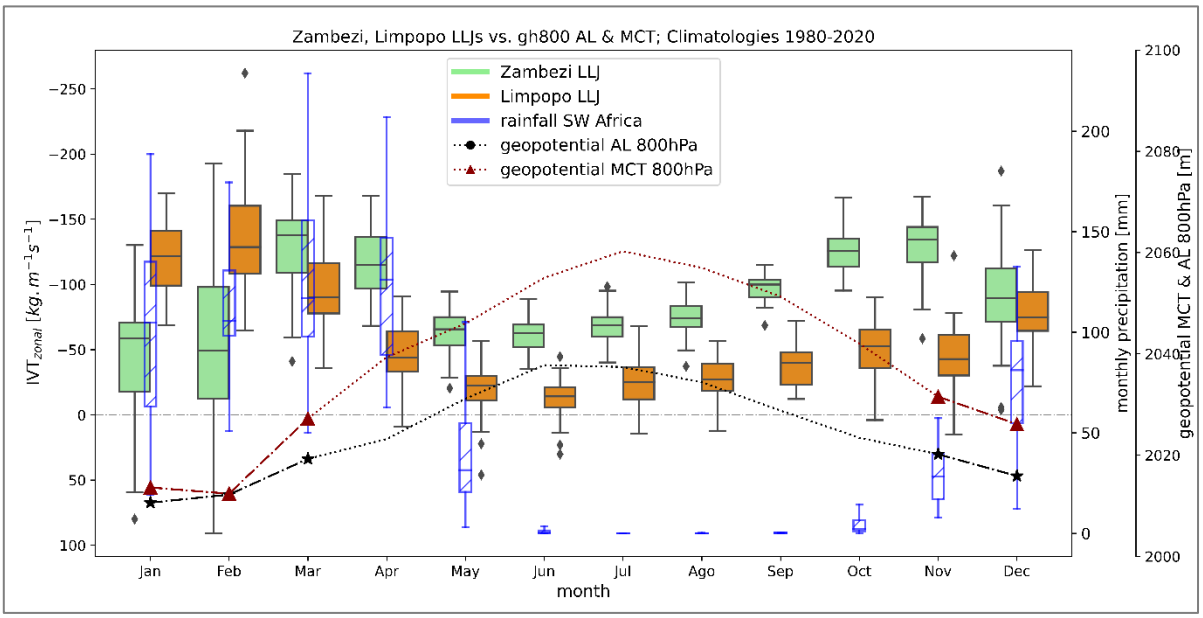

Figure 3.12 – Monthly climatologies of retrieved ERA5 variables (for 1980-2020 period), over Southern African subcontinent. Green and orange boxplots represent, respectively, the monthly distribution of IVT_u (across the 40-year period) for Zambezi and Limpopo LLJs, with a grey line inside each box indicating the median value. As previously done, both LLJs' data were retrieved with respect to sections presented in Figure 3.1a. Dashed grey line marks IVT_u threshold between eastward ($IVT_u > 0$ [$kgm^{-1}s^{-1}$]) and westward ($IVT_u < 0$ [$kgm^{-1}s^{-1}$]) transport of water vapour. Blue boxplots with stripes, show rainfall monthly distributions, retrieved as an average of values over the region of interest (dark-red square in Figure 2.3). Values of gh800 for the AL (dashed black line with stars) and MCT (dashed dark-red line with triangles) were retrieved, for the rainy season months (Nov-Mar), using the local minimum searching methodology (subsection 2.3). With the disappearance of the AL and MCT during the dry season (Apr-Oct), gh800 values were computed as an average value of the region used to search both low-pressure systems (dark and green square area in Figure 2.3, corresponding, respectively, to AL and MCT regions).

Through Figure 3.12 (and Figure 3.2 as well), a monthly alternance of low-level humidity transport intensity between both river valleys is observed, with ZRV presenting higher IVT_u values than LRV by November and March, and LRV displaying higher IVT_u values than ZRV by January and February. As stated in Barimalala et al. (2018, 2021), this is a consequence of 3 main factors, operating together: the seasonal oscillations of the ITCZ, the presence of Mascarene HP system, and the continental blocking of Madagascar on the mean easterly winds. As referred in Schneider et al. (2014), the ITCZ is characterized as a zonal tropical belt of deep convective clouds, oscillating back and forth around the equator. It migrates towards the hemisphere that warms relative to the other, retrieving large amounts of humidity from the ocean (in this case, from the Indian Ocean). The continuous action of the Mascarene HP promotes a westward flux, containing high amounts of water vapour, towards the subcontinent – it explains a great humidity flux registered in both river valleys during austral summer, a period where the ITCZ reaches its maximum southward shift.

Analysing Figure 3.12, during the dry season (May to September), both Zambezi and Limpopo LLJs are defined by a weak zonal transport of humidity, with ZRV, on average, presenting higher IVT_u values than LRV. Limpopo LLJ usually reaches null values during dry season months (i.e., the LLJ completely disappears) and Zambezi LLJ maintains a weak (but not null) humidity transport towards western parts of the subcontinent. Jointly, the AL and MCT regions present high values of gh800 values, reaching maximums during the peak of the dry season (in July), reflecting the dominance of HP systems (St.

Helena HP and Mascarene HP) at both AL and MCT latitudes. During these months, null or close-to-zero values of precipitation are registered.

However, from September/October, as the austral summer approaches, low-pressure systems establish over the subcontinent, as gh800 values over the AL and MCT regions start to decrease, reaching its minimum gh800 values (higher intensity) during January. The reduction of gh800 values is followed by an increasing of zonal moisture transport towards SW Africa via Zambezi and Limpopo LLJs, as well as by a rising of rainfall values in the region of interest. As the ITCZ moves southward and then northwards, crossing ZRV latitude twice (by October/November and by March/April), the associated LLJ presents 2 maximums of IVT_u, around November and March and a relative minimum in February.

January and February are associated with a very large ZRV IVT_u monthly variability, as seen by the length of boxplot's whiskers in Figure 3.12. During these months, ZRV LLJ weakens and, in some cases, disappears or changes to an eastward direction ($IVT_u > 0$ [$kgm^{-1}s^{-1}$]). This is a result of Madagascar's landmass presence, which perturbs mean wind fluxes towards Southern Africa. As discussed in section 1 and pointed out in Barimalala et al. (2018), the MCT is more vigorous, by January and February, in the MC, due to the perturbation caused by this island. This process favours a south-easterly wind regime (south of the MC) that ends up clashing with the East African Rift System (EARS), over the LRV region, injecting high amounts of humidity in the subcontinent via this LLJ (and not via Zambezi LLJ) (as seen in Figure 3.1 and Figure 3.2). Therefore, Limpopo LLJ shows a relative IVT_u minimum in November and reaches its maximum intensity by February, as well as its maximum variability. All these oscillations of IVT_u between both LLJs are accompanied by high precipitation values over SW Africa, reaching maximums values around February. During these months, very high rainfall variabilities are also registered.

By March, as the ITCZ starts to move northward, AL and MCT gh800 start to increase, and the south-easterly winds (still coming from the southern part of the MC) with the help of MCT cyclonic circulation, reaches the ZRV with large amounts of water vapour. From April onwards, the ITCZ keeps its northward path, bringing much more humidity to ZRV than LRV (as also seen in Figure 3.1 and Figure 3.2). ZRV being placed north of the LRV explains why, over the late rainy season and dry season months, ZRV presents higher IVT_u values than the LRV. The latter practically disappears during the dry season. This process is followed by a dramatic fall in precipitation values as austral winter comes and HP systems regain their major influence across the subcontinent (dry season starts).

In summary, due to: (1) ZRV placed north of the LRV; (2) the Madagascar island blocking and shifting southward part of the easterly humidity flux induced by Mascarene HP and (3) most of the retrieved humidity (from the Indian Ocean) depending on the seasonal position of ITCZ; in Figure 3.12, alternances of IVT_u maximums and minimums over both LLJs are seen. The occurrence of both MCT and AL during austral summer (where low gh800 values persist), jointly with both LLJs monthly alternance, allow great amounts of moisture to converge and precipitate across the subcontinent (and over SW Africa, as well). This explains higher precipitation values (and larger rainfall variability) across the region of interest, as shown in Figure 3.12.

3.4. Large-scale modes of variability and its relationship with regional rainfall

Rainfall over the subcontinent, essentially across SW Africa, not only is controlled by the MCT and AL dynamics, but also by the position of these low-pressure systems. In fact, MCT and AL can change its latitudinal position, at least, in a monthly timescale, influencing regional rainfalls. A recent study

performed by Crétat et al. (2019) related AL meridional displacements and intensities with ENSO phases (El-Niño or La-Niña). This article served as a starter to an analysis about the effects of large-scale variability on the AL latitudinal shifts, intensities, and associated rainfall across the region of interest. Hence, 2 modes of large-scale variability were analysed: ENSO and SIOD (detailed in subsection 2.5).

The analysis made in this subsection aimed at understanding the relationship between both ENSO and SIOD modes of variability, the meridional displacement and intensity of the AL, and its impacts on rainfall across the region of interest. This analysis was performed during the months where the AL feature is more pronounced (i.e., December, January, and February). In this way, as explained in subsection 2.5, Niño3.4 and SIOD monthly indexes were computed using monthly ERA5 SST data over the Indian Ocean. With ERA5's gh800 monthly field (for the period of 1980-2020), local minima searching methodology (subsection 2.3) was performed, in order to collect the AL latitude in each month, as well as its gh800 intensity and anomaly. Monthly ERA5 rainfall data for SW Africa was also used. Then, Figure 3.13 was produced.

In fact, both modes of variability do not act individually, but combined with each other. Due to this, the impacts of ENSO and SIOD needed to be analysed together, using combinations of both indexes (Niño3.4 and SIOD). Figure 3.13 illustrates AL latitude displacements and intensities, alongside with the relative frequencies of dry and wet months over the region of interest (percentiles 25 and 75, respectively), for each combination of ENSO and SIOD phases.

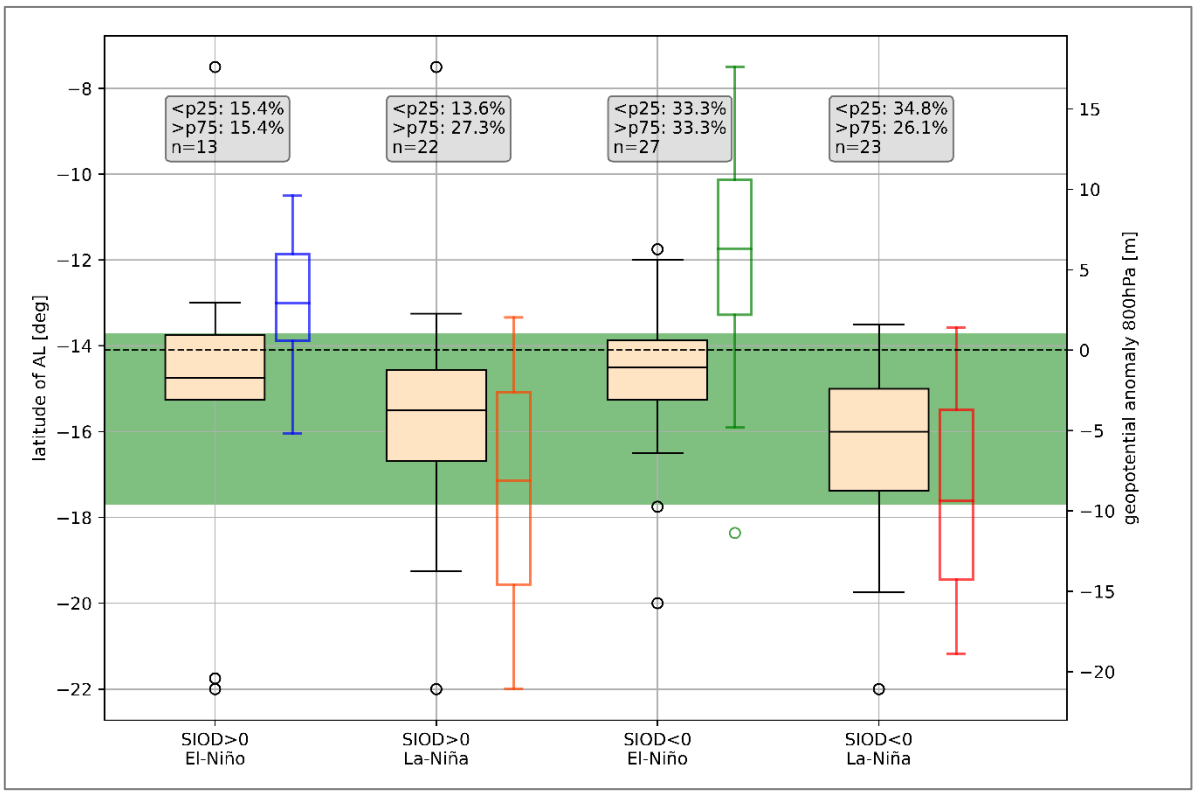

Figure 3.13 – Monthly ERA5 data (for all December, January, and February 1980-2020) of AL latitude and gh800 anomalies, as well as of rainfall over the study region, according to combinations of both modes of variability (SIOD and ENSO), using Niño3.4 and SIOD indexes. All 4 combinations are associated with 2 boxplots: one representing the latitude distribution of the AL (cream colour) and the other one representing gh800 anomaly of the AL (blue, orange, green or red, depending on the aggregation of modes). The relative frequency of months with rainfall below the 25th percentile and above the 75th percentiles, for each combination, is displayed in grey boxes. The *n* stands for the number of months used in each combination. Green area delimits the latitudes of the region of interest (FRESAN project).

It becomes clear, through Figure 3.13, that El-Niño (La-Niña) phases of ENSO are linked with northward (southward) AL shifts and, as well, weaker (stronger) AL intensities, i.e., negative (positive) AL gh800 anomalies. When analysing relative frequencies of precipitation over the region, it may be observed that during El-Niño phases (Niño3.4 > 0.4[°C]), monthly rainfalls over SW Africa are not either below or above normal (percentiles 25 and 75 present equal relative frequencies). However, in La-Niña phases (Niño3.4 < -0.4[°C]), there are great differences between both rainfall percentiles. During La-Niña events, negative (positive) SIOD indexes are related with higher chances of a drier (wetter) period occurrence. This result partially matches the results of Hoell & Cheng (2018), which found out that, during La-Niña (El-Niño) years, when SIOD and Niño3.4 displays opposite signs, rainy (dry) conditions persist over the subcontinent.

Even tough through Figure 3.13 it is possible to verify the implications of ENSO and SIOD on AL intensities and shifts, as well as on rainfall percentiles over the region of interest, a spatial extension of precipitation impacts across the subcontinent was needed. Thus, composites of precipitation anomalies were computed, for Southern Africa subcontinent, using 4 combinations of ENSO and SIOD phases already displayed in Figure 3.13. Composites were produced similarly to the ones of Figure 3.5, Figure 3.8 and Figure 3.10. Results are shown in Figure 3.14.

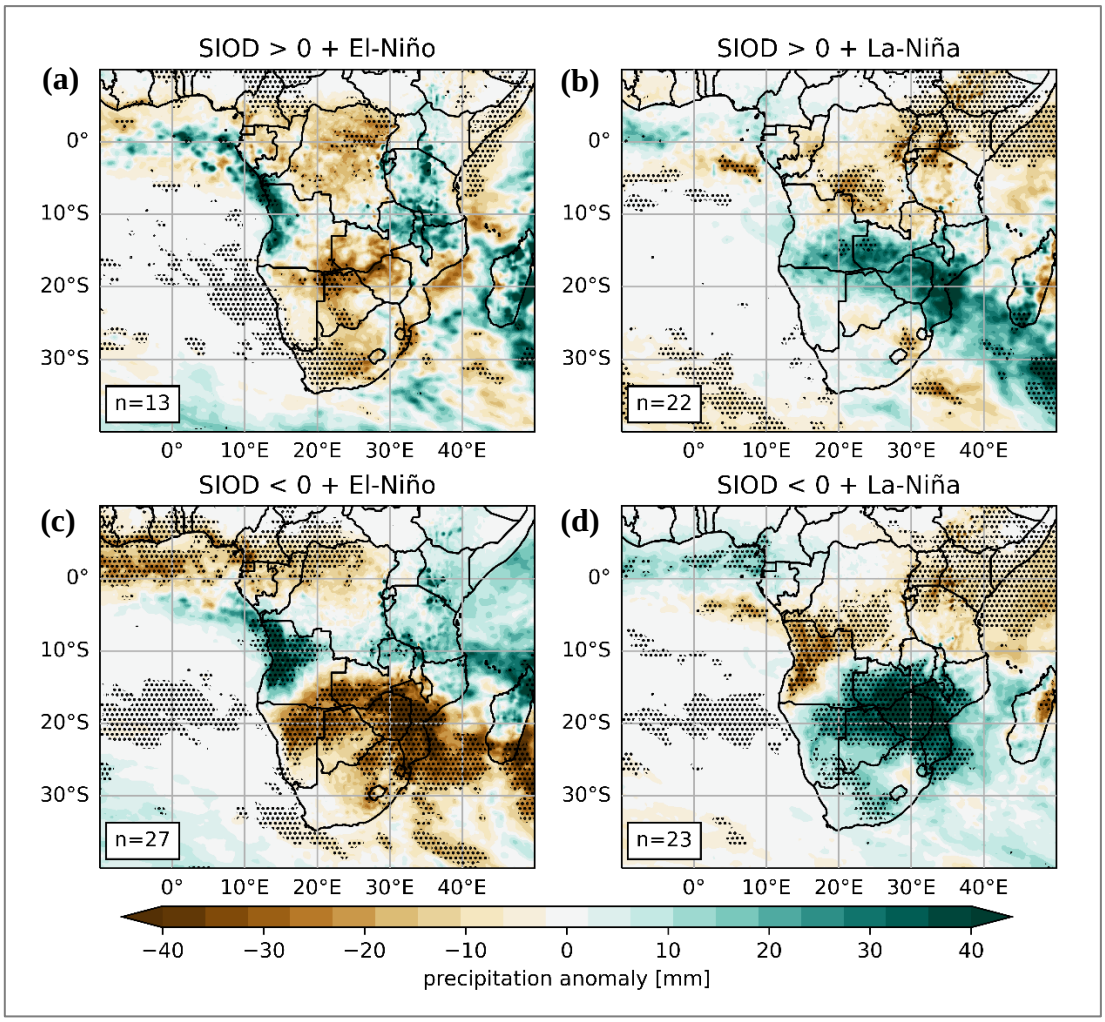

Figure 3.14 - Same as Figure 3.5, but for rainy season months that registered a conjugation of **(a)** positive SIOD and El-Niño conditions (Niño3.4 > 0.4[ºC]); **(b)** positive SIOD and La-Niña conditions (Niño3.4 < -0.4[ºC]); **(c)** negative SIOD and El-Niño conditions (Niño3.4 > 0.4[ºC]) and **(d)** negative SIOD and La-Niña conditions (Niño3.4 < -0.4[ºC]).

The results presented in Figure 3.14a,c showed that, generally, El-Niño years enhance, during the rainy season, drier conditions across the subcontinent, in particular when SIOD is negative, with the exception of western Angolan regions, parts of Madagascar, and some areas north of Lake Malawi, where El-Niño (La-Niña) phases are associated with higher (lower) than normal rainfall values.

La-Niña periods show a relation with wetter conditions across Southern Africa (Figure 3.14b,d), with well-above normal precipitation anomalies. The results converge with Hoell & Cheng (2018), that found a relation between La-Niña (El-Niño) phases and higher probabilities of wet (dry) rainy seasons across the subcontinent, with an anomalous low-tropospheric cyclonic (anticyclonic) circulation dominating Southern Africa countries.

For SW Africa (region of interest), months experiencing La-Niña phases and positive SIOD indexes show a pattern of positive rainfall anomalies, yet not statistically significative (Figure 3.14b). In Figure 3.14a,c,d, ENSO and SIOD conjugations placed the study region within a *border zone* between wetter and drier conditions, not being possible to take robust conclusions regarding both variability modes influence on rainfalls. This situation enhances the vulnerability conditions of this region, as slight changes in any of 2 analysed large-scale patterns can easily induce higher or lower than normal precipitations.

In fact, across the subcontinent, rainfall anomalies (higher or lower) can also be enlarged by orographic effects. In several examples already seen (Figure 3.8c,d; Figure 3.10a or Figure 3.14c,d) precipitation anomaly signals over SW Africa seemed to spatially match the mountainous regions of western Angola (e.g. Bié Plateau and Huíla Highlands). Western Angola/Namibia orographic enhancement of rainfall gradients is also referred in a recent study performed by Thoithi et al. (2021). In subsection 6.3 (Appendix), pictures of observed orographic-induced stormy clouds above Huíla highlands (southern Angola) are presented – see Figure 6.5 and Figure 6.6.

Despite this last analysis on large-scale modes of variability seemed to, in some measure, explain latitudinal shifts and intensity changes of the AL, the drivers of such meridional displacements and changes in geopotential anomalies, are yet still to be fully understood. Rainfall variability across the Southern African subcontinent and its atmospheric and oceanic drivers, represent a recent object of intense study by several researchers. Therefore, most of the physical processes presented in this thesis and its relationship with oceanic-atmospheric interactions and large-scale modes of variability, are still poorly understood by the scientific community, thus warranting further research on the subject.

3.5. Case-studies over SW Africa

Across the previous subsections (3.1 to 3.4), synoptic and climatological analysis were performed on both Zambezi and Limpopo LLJs, and on both AL and MCT low-pressure systems. The way these weather features (and associated circulation patterns) are influenced by large-scale modes of variability and, consequently, affect rainfalls over the region of interest and over the entire Southern African subcontinent, were investigated.

However, some of the identified AL vs. MCT common patterns (e.g., tendency for a weaker AL to be associated with a weaker MCT, and vice-versa) were not verified during some rainy seasons, contradicting the findings of the subsection 3.3. In fact, some of these contradictory rainy seasons corresponded to the most exceptional events occurred in the past 40 years over the region of interest. As an example, 2010/11 was considered an extremely wet hydrological year, and in 2018/19, SW Africa experienced an intense drought (as seen in Figure 6.1 - Appendix). Thus, to comprehend such

extraordinary events, both rainy seasons were analysed in detail. They were studied with respect to anomalies of IVT (magnitude and direction) and zonal specific humidity ($\dot{q_u}$), as well as anomalies of gh800 over the AL and MCT regions. It is very important to recall that positive $\dot{q_u}$ anomalies refer to an anomalous eastward moisture transport (i.e., weaker LLJs, as they normally advect humidity towards the west). The opposite situation, i.e., negative $\dot{q_u}$ anomalies, correspond to stronger LLJ intensities.

3.5.1. Rainy seasons with below-normal precipitation – the case of 2018/19

In fact, the hydrological year of 2018/19 over SW Africa was recorded as one of the driest periods since the beginning of the ERA5 timeseries, i.e., since 1980 (Figure 6.1). This hazardous dry period comes after 7 almost-consecutive years of intense drought, causing an amplification of aridity effects over the region. Even with some periods of sporadic rainfalls and close-to-average hydrological years, it was not enough to surpass the continuous drought across the region. During this period, as stated in various international newsletters (Amnesty International, FAO, UN) and referred by Limones et al. (2020), southern Angola regions were severely affected by agricultural losses, directly associated with livestock deaths, malnutrition, famine, and migrations. Hence, to understand the drivers of these exceptional events, a monthly synoptic analysis for rainy season months of 2018/2019 rainy season, for 3 ERA5 fields' anomalies: precipitation, gh800 and IVT (as seen in Figure 3.15), was performed. The rainy season months of December, January, February, and March were analysed. Cross sections of anomalies of zonal specific humidity transport ($\dot{q_u}$), for these months, were also plotted (Figure 3.16) along the Zambezi and Limpopo river valleys, in order to understand the role played by both LLJs.

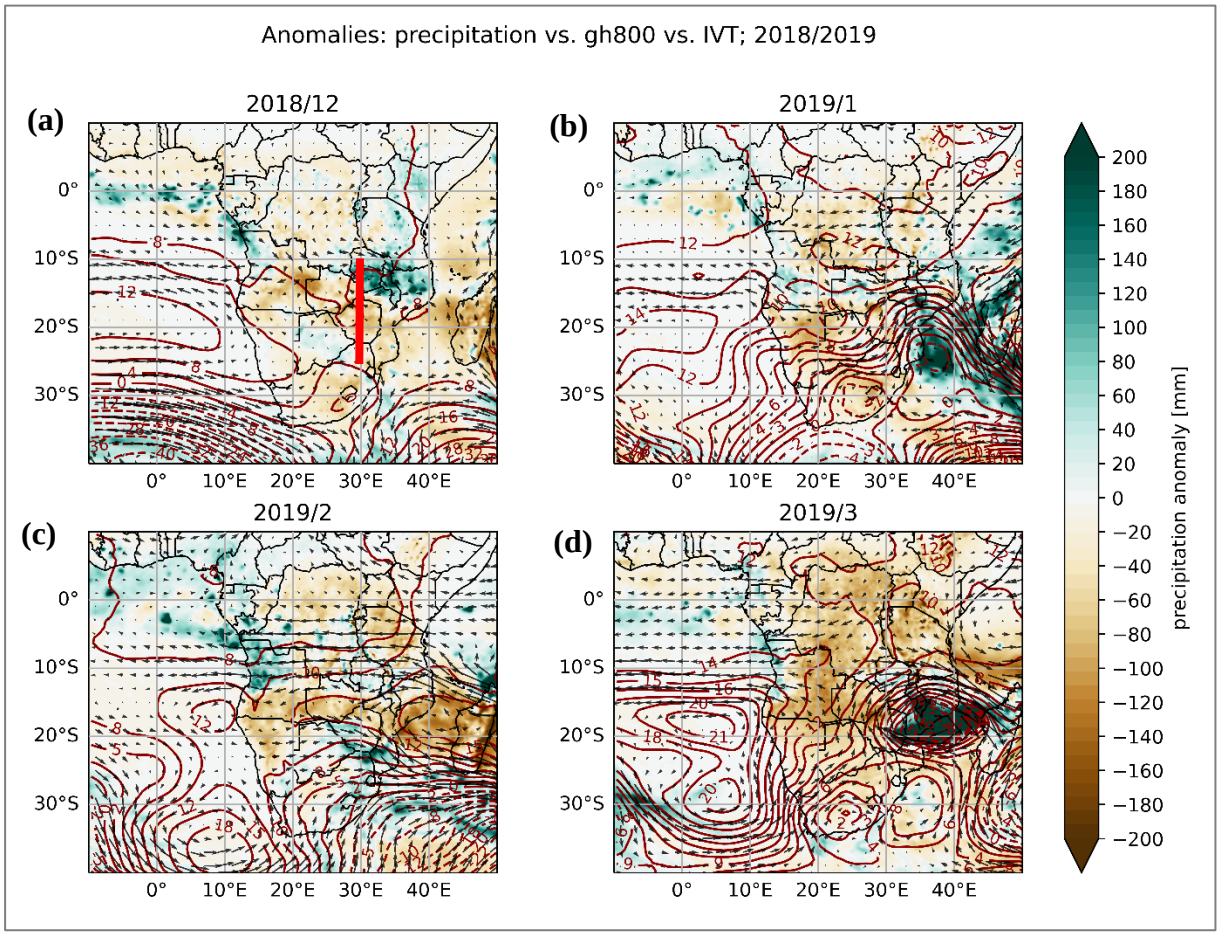

Figure 3.15 - ERA5 monthly anomalies (over the subcontinent) of 3 fields: precipitation (coloured shading), gh800 (dark-red contours) and IVT (dark-grey quivers), for **(a)** December 2018, **(b)** January 2019, **(c)** February 2019 and **(d)** March 2019. Dark-grey quivers are spaced 1.6ºx1.6º and gh800 (black contours) are interpolated across points spaced 0.75ºx0.75º. Dashed contours represent negative gh800 anomalies. Red line on panel (a) represent the section made to produce Figures 3.16 and 3.18.

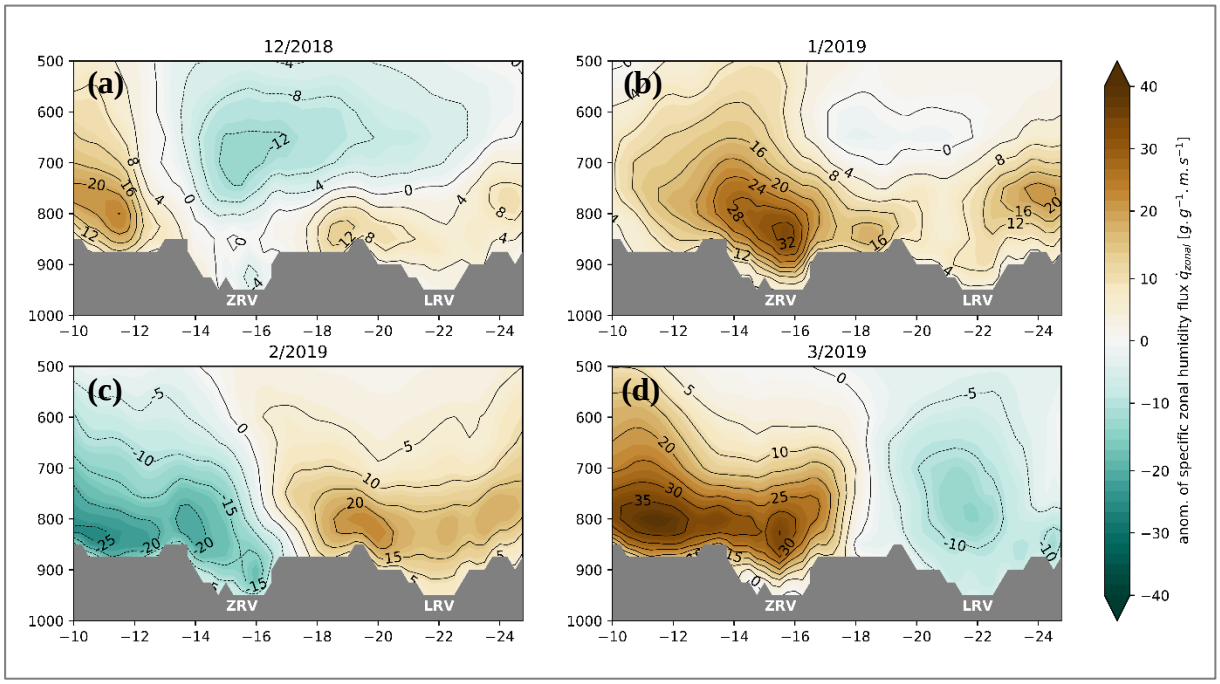

Figure 3.16 - Meridional cross-sections (made at 30ºE, following the red line on Figure 3.15) of ERA5 zonal specific humidity ($\dot{q_u}$) anomalies for **(a)** December 2018, **(b)** January 2019, **(c)** February 2019 and **(d)** March 2019. Positive anomalies of $\dot{q_u}$ mean a reduction of westward humidity transport intensity or even a change of the zonal direction of the LLJs (the transport become eastward). Negative anomalies of $\dot{q_u}$, mean an intensification of the westward humidity transport across the LLJs. Either Zambezi (ZRV) and Limpopo (LRV) river valleys are identified in the figure with white acronyms.

Inspecting Figure 3.15a, it is possible to observe, by the end of 2018 (December), positive (weak) gh800 anomalies over both MCT and AL region, as well as a close-to-normal IVT. Above normal values of gh800 anomalies over AL region didn't allow vigorous moisture convection to occur. Thus, below-normal precipitation was registered, essentially over southern and eastern Angola. This pattern of positive gh800 anomalies over SW Africa, continued in January and February 2019 (Figure 3.15a,b), with most of the humidity not being converted in precipitation. In addition, in January 2019, a small-area of slightly negative gh800 anomalies was observed, causing an anomalous cyclonic motion over the MC, as well as an anomalous eastward IVT towards the MC region, bringing above-average rainfalls to these regions and blocking humidity advection towards SW Africa. Consequently, below-normal precipitations occurred, particularly over northern and central Namibia. Cross-section in Figure 3.16b shows evident positive anomalies of $\dot{q_u}$ over ZRV and LRV (i.e., weaker LLJs).

During February 2019 (Figure 3.15c), positive anomalies of gh800 appeared over the MC region. The appearance of such anomaly at that latitude didn't allow a prominent westward IVT, specially in LRV, where positive anomalies of $\dot{q_u}$ were registered (Figure 3.16c). Therefore, a zonal band of below-normal precipitations appeared in the regions covering the MC, reaching SW Africa, passing through the central parts of the subcontinent.

However, an anomalous synoptic event occurred in March 2019 over the MC (Figure 3.15d), with steeped below normal gh800 values and abnormally high amounts of rainfall, in particular over Mozambique. This cyclonic event was the catastrophic category 3 tropical cyclone Idai, which killed more than 1300 people across these east-African countries and lasted almost 1 month over the MC region (from March 4th to March 21st) (Masters, 2019). This extreme event perturbed the entire synoptic circulation over the MCT region, pulling an anomalous eastward IVT towards the Indian Ocean, and

blocking the humidity advection towards SW Africa. Thus, across southern Angola and northern Namibia, below-normal rainfalls occurred, and a dramatic drought intensification was observed. Cross section for March 2019 (Figure 3.16d) shows a visible positive anomaly of $\dot{q}_u$ in ZRV (weak LLJ).

In short, Figure 3.15b and Figure 3.15d (January and March 2019) demonstrated that local cyclonic circulations over the MC, boosted an anomalous eastward IVT over both ZRV and LRV, not allowing moisture to reach SW Africa and, eventually, precipitate. Thus, a simultaneous westward humidity blocking over the MC (promoted by cyclonic circulations) combined with positive gh800 anomalies over Angola/Namibia (characteristic of weaker AL states), represented the main drivers of significant negative rainfall anomalies across these regions and the enhancement of the ongoing severe drought.

3.5.2. Rainy seasons with above-normal precipitation – the case of 2010/11

Across SW Africa, the rainy season of 2010/11 represented the wettest period since the beginning of timeseries. Extreme floods occurred all over southern Angola and northern Namibia, killing dozens and displacing thousands of people, as well as damaging bridges, roads, houses, and farms (Grobler, 2011; Vieira, 2011). The same way it was done in subsection 3.5.1. for the 2018/19 drought event, 2010/11 rainy season was analysed synoptically (with respect to gh800, rainfall and IVT anomalies) and using cross-sections along Zambezi and Limpopo river valleys (Figure 3.17 and Figure 3.18).

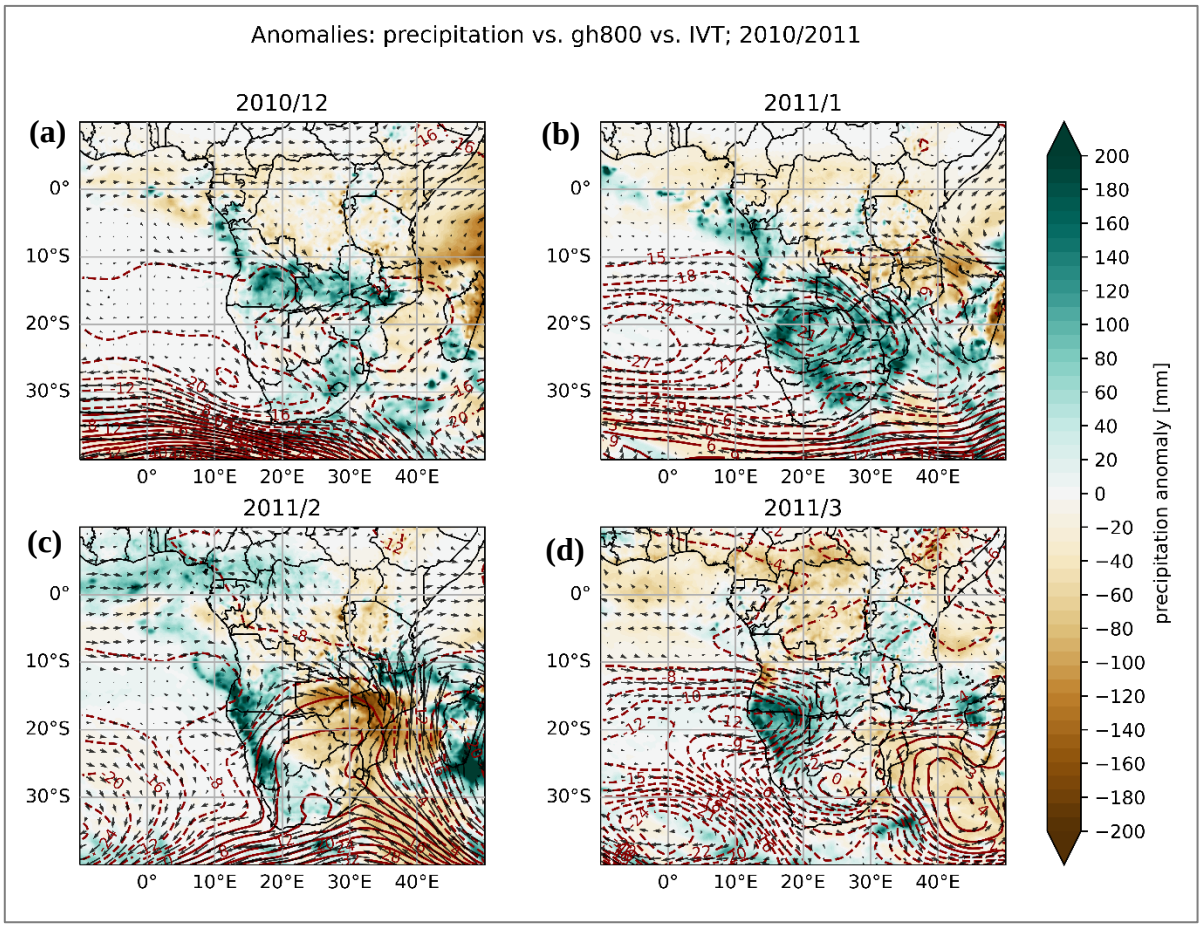

Figure 3.17 – Same as Figure 3.15, but for the 2010/11 rainy season.

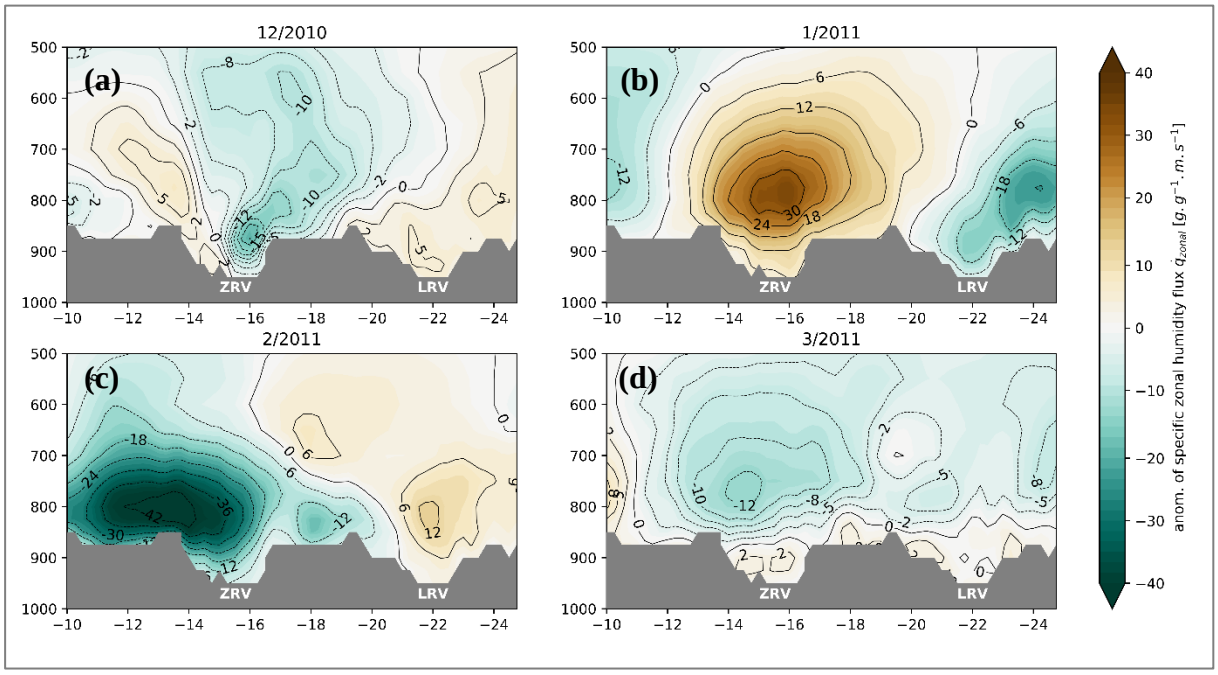

Figure 3.18 – Same as Figure 3.16, but for the 2010/11 rainy season.

Analysing the anomalies of fields displayed by Figure 3.17a (December 2010), on average, over central Angola (AL region) and across the MC, minimums of gh800 anomaly were observed. This anomalous cyclonic circulation generated over Angola, as well as its latitudinal position, was favourable to a greater-than-normal IVT from the Atlantic and Indian Oceans. Thus, over almost all of Angola and Zambia, positive precipitation anomalies occurred, including southern Angola. However, an anomalous anticyclonic circulation was originated over the MC, contributing to inject humidity towards SW Africa, mainly via ZRV. Consequently, Zambezi LLJ registered slightly negative anomalies of $\dot{q_u}$ (see Figure 3.18a).

Along January 2011, over the AL region, negative gh800 anomalies shifted southward (Figure 3.17b). The northern edge of this anomalous cyclonic circulation was responsible for bringing humidity from the Atlantic Ocean and equatorial regions. The southern side of the anomaly pulled, from the Indian Ocean (via Limpopo LLJ), great amounts of humidity, as seen in the IVT anomalies. Therefore, the entrance of moisture via Zambezi LLJ was blocked. This way, as seen in Figure 3.18b, Limpopo LLJ presented negative $\dot{q_u}$ anomalies (stronger LLJ), while Zambezi LLJ displayed a pronounced positive anomaly (weaker LLJ). Therefore, deep convection occurred, and well-above-average precipitations were observed all over the subcontinent.

During February 2011, the MC region and the Kalahari desert assisted to an increasing of gh800 values, with positive anomalies being observed over these regions (see Figure 3.17c). The respective circulation pattern generated an anomalously high IVT transport (from the Indian Ocean), towards SW Africa, which, together with negative gh800 anomalies across this area, originated well-above-normal rainfalls. Anomalously high IVT occurred over Zambezi LLJ, which registered negative anomalies of $\dot{q_u}$ (Figure 3.18c).

Throughout March 2011, a deep gh800 anomaly occurred, once again, over Angola and Namibia, near the border of both countries – see Figure 3.17d, generating a circulation that allowed the entrance of

Atlantic humidity towards SW Africa, specially to southern Angola and northern Namibia. Humidity convergence was also fed by Indian Ocean moisture, as the IVT entrance in the subcontinent was facilitated by the anomalous anticyclonic circulation originated around a positive gh800 anomaly registered over the southern part of MC region. This way, above-average precipitations were also registered across southern Angola and northern Namibia. Close-to-normal values of $\dot{q_u}$ prevailed along the ZRV and LRV (Figure 3.18d). Hence, the 2010/11 rainy season was marked by, at least, 3 consecutive months with well-above-average rainfalls over SW Africa.

To summarize, as seen in Figure 3.17, the AL and MCT region presented persistent negative gh800 anomalies (characteristic of stronger AL and MCT states) which favoured an anomalous IVT from the Atlantic and from the Indian Ocean a swell as widespread convective processes over the subcontinent. Depending on the latitude position of the AL gh800 anomaly, transport of humidity from the Indian Ocean was more vigorous from the LRV (ZRV) with southward (northward) shifts of the anomaly (Figure 3.17 and Figure 3.18). As the strong AL over SW Africa pulled great amounts of humidity from both oceans, conditions for deep convection processes started to occur. Therefore, very high amounts of rainfall were registered in the region of interest.

In this study case, most of the 2010/11 above-normal rainfall across the subcontinent seemed to be caused by the widespread minimums of gh800 anomalies over AL and MCT region. (both AL and MCT presented, in 2010/11 rainy season, strong intensities).

3.5.3. Influence of large-scale modes of variability on the exceptionality of case-studies

As argued earlier in subsection 3.3, MCT and AL usually display the same phase (typically both weak or both strong), and not different phases, as happened with 2018/19 rainy season. Moreover, both weak AL and MCT phases relates with above-normal precipitations over SW Africa and, both strong states, with below-normal rainfalls. This pattern was not observed in any of the case-studies: 2018/19 presented a close-to-normal MCT and a weak AL phase (related with below-normal rainfalls), and 2010/11 presented both strong AL and MCT states (linked with above-normal rainfalls). Thus, as these case-study examples were found to be contradictory when compared to the climatological results of subsection 3.3, it was decided to analyse all the precipitation-related mechanisms (AL, MCT, Zambezi and Limpopo LLJ, SIOD and ENSO) in only one figure, to understand the reasons behind the exceptionality of both events – see Figure 3.19.

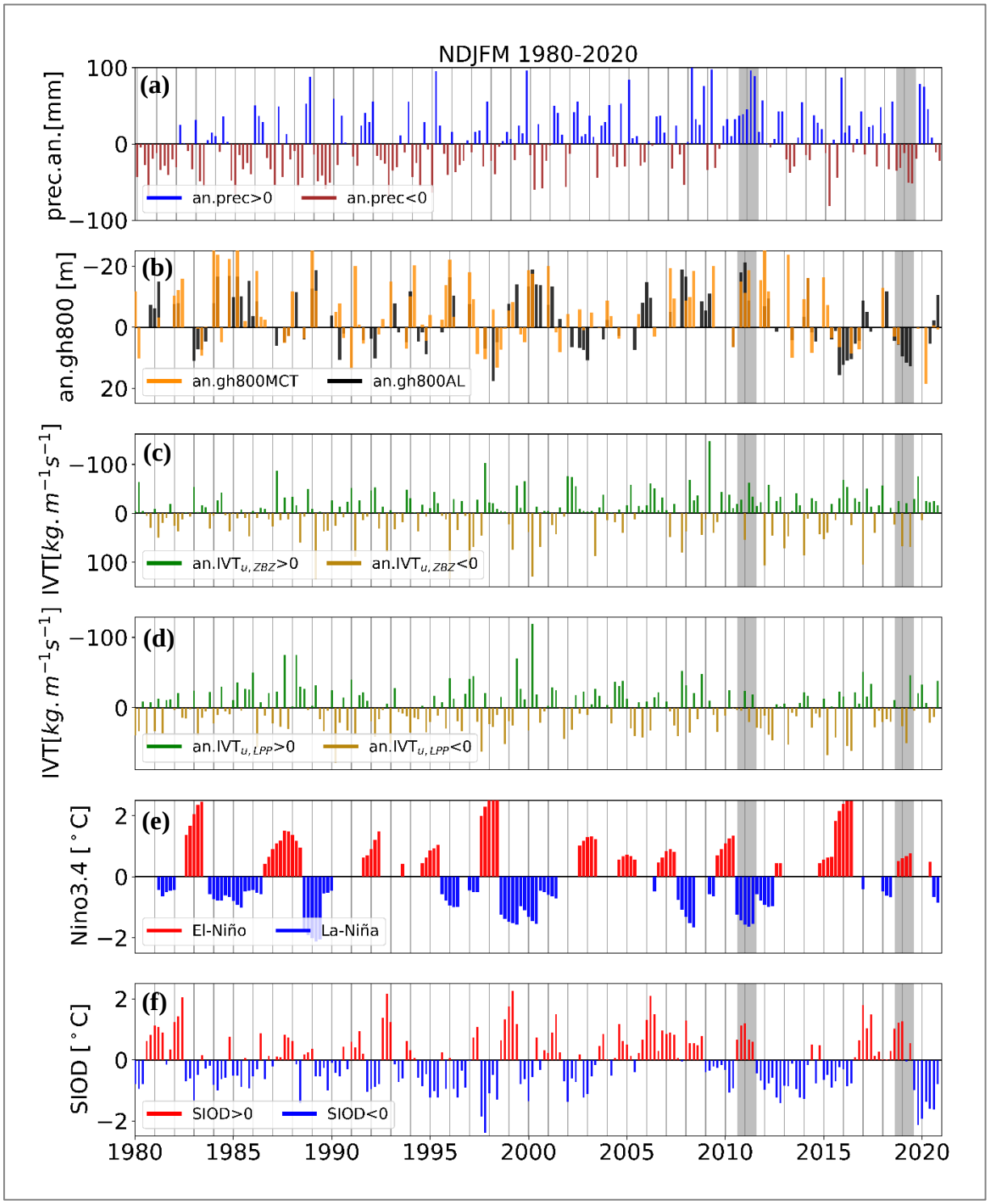

Figure 3.19 – Timeseries of retrieved ERA5 variables, for 1980-2020 rainy season months (Nov-Mar), over the southern African region. In each panel, it is observed timeseries of **(a)** rainfall anomalies over the study region (SW Africa), where brown (blue) bars indicate below (above) normal precipitation months; **(b)** gh800 anomalies for weak and strong AL (black bars), as well as weak and strong MCT (orange bars); **(c)** IVT_u anomalies for Zambezi LLJ; **(d)** same as panel (c) but for Limpopo LLJ; **(e)** Nino3.4 index, where red bars represent El-Niño months (i.e. Niño3.4 > 0.4[ºC]) and blue bars, La-Niña months (i.e. Niño3.4 < -0.4[ºC]); **(f)** SIOD index, where red bars represent positive SIOD months and blue bars, negative SIOD months. The classification criteria used to distinguish strong and weak AL and MCT was the same used previously in subsection 3.3. SIOD and Niño3.4 computations are detailed in subsection 2.5. All anomalies were computed using 1980-2010 normal. Shaded grey areas indicate both case-studies of the present section, i.e., 2010/11 and 2018/19 exceptional rainy seasons.

Therefore, analysing the previous plot, during 2010/11 rainy season months, a strong La-Niña period was registered, as well as positive values of SIOD (Figure 3.19e,f). Recalling Figure 3.14b, a pattern of wetter spells over the subcontinent was identified when this type of large-scale conjugation happens (even though without high statistical confidence). Figure 3.13 also showed tendencies for negative AL anomalies during La-Niña periods. Thus, it is possible to understand that widespread negative gh800 anomalies occurred over the subcontinent in 2010/11 rainy season had, as a main source, a strong La-Niña event. This situation had consequences on AL and MCT intensities, whose gh800 anomalies ended up embedded in the large-scale influence (Figure 3.19b). This might represent a justification for a stronger AL and MCT dominance across the region, during this period. The large-scale pattern enhanced AL and MCT intensities. Consequently, it enhanced Zambezi and Limpopo LLJ moisture advection (Figure 3.19c), as a result of the AL meridional shifts during these months. High SST values over the MC (i.e., positive values of SIOD) also contributed to a prominent moisture availability in the subcontinent's atmosphere.

Along 2018/19 rainy season months, El-Niño conditions and positive SIOD indexes were registered (Figure 3.19e,f), together with a weaker AL. The results match what previous figures showed (Figure 3.13 and Figure 3.14b): El-Niño and positive SIOD conjugations bringing dry spells to central-southwestern parts of the subcontinent and weaker AL states. The MCT presented close-to-normal intensities (Figure 3.19b), whose associated circulation was not favourable to a vigorous humidity advection towards southern African regions, essentially via ZRV or LRV (as seen in Figure 3.19c,d). Thus, a weaker moisture advection within both river valleys and a weaker AL (associated with weaker convective processes), promoted below-normal rainfalls across the region of interest (Figure 3.19a). In addition, higher-than-normal SSTs over the MC (SIOD > 0), created ideal conditions to feed mesoscale powerful cyclonic circulations, as tropical cyclone Idai (which contributed to block humidity towards SW Africa). Idai was clearly a local circulation feature, not representing a full synoptic scale weather system (i.e., in this case, local circulation had a major importance when compared with global circulation). This way, caution is needed when interpreting this type of phenomena, as it did not represent the MCT feature itself.

To finalize, inspecting Figure 6.2 (see Appendix), most of the previously analysed exceptional rainy season months (marked as blue and red dots) corresponded, generally, to values relatively away from the regression line. 2010/11 rainy season months were even more exceptional than 2018/19, with a higher displacement from the regression line.

A schematization of what was learned throughout section 3 (from subsection 3.1 to 3.5), is presented in Figure 3.20. The latter resumes the main ideas retrieved from the analysis and discussions of the results previously displayed.

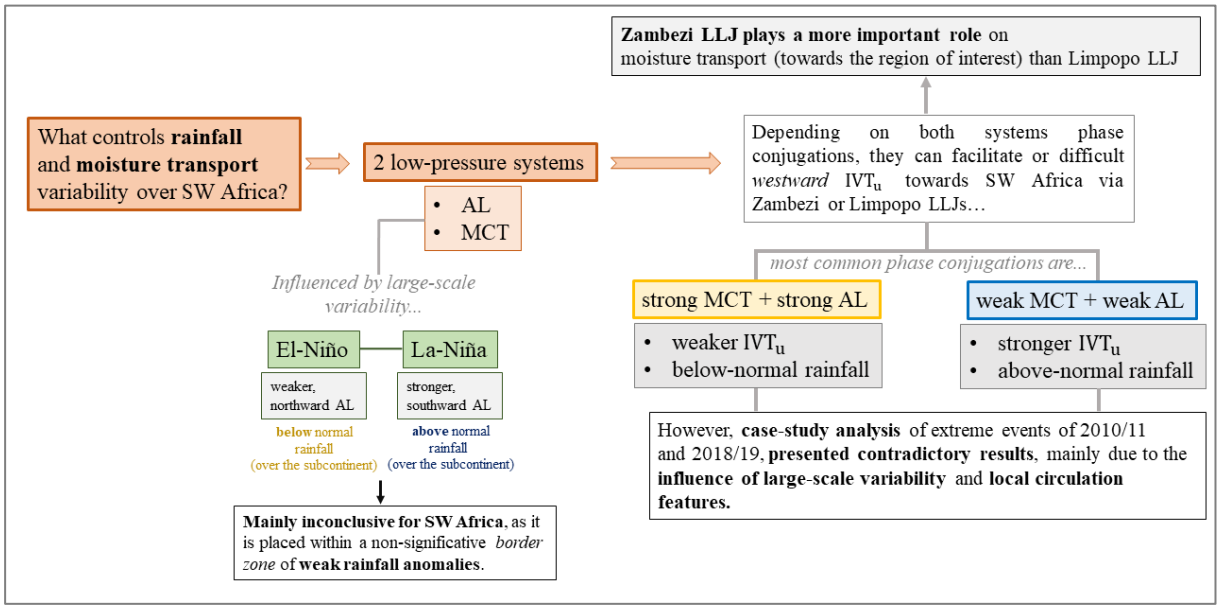

Figure 3.20 – Schematization of what was learned from the section 3.

4. Conclusions

Using ERA5 reanalysis and 10 WS data (located over SW Africa), this work highlighted the importance and the role played by atmospheric synoptic features on rainfalls over the Southern African subcontinent, particularly on austral summer and across the region of interest, southern Angola and northern Namibia (SW Africa). These identified features were two low-pressure systems: the Angola Low (AL) and the Mozambique Channel Trough (MCT), and two orographic-induced low-level jets (LLJs), located over both the Limpopo and Zambezi River Valleys (LRV and ZRV, respectively). Therefore, LLJs variability are mainly explained by the conjugation and interactions between both low-pressure systems' phases (MCT and AL).

In fact, most of atmospheric moisture that reaches SW Africa comes from the Indian Ocean, which is placed more than 2000[km] east of SW Angola. The seasonal shifts of the ITCZ (southward during austral summer and northward during austral winter), together with a westward circulation promoted by the semipermanent Mascarene HP (placed in SW Indian Ocean) and perturbations induced by Madagascar island's landmass, explain the alternance of westward humidity transport (IVT_u) within both ZRV and LRV. The genesis of the MCT over the Mozambique Channel (MC), by adjustment of the mean westward flow to Madagascar's topography, together with the existence of the AL, typically placed over Angola and originated by surface-heating and low-level moisture convergence, controls the humidity advection (via both river valleys' LLJs) towards the interior of subcontinent (including SW Africa). Therefore, most of precipitation variability over the region is explained by phase conjugations (weaker or stronger) between the MCT and the AL. In subsection 3.3, where MCT and AL phase conjugations are studied, main results showed that MCT and AL very often present the same phase (either both weak, or both strong). Weak (strong) MCT and AL are usually related with above (below) normal rainfalls over SW Africa.

The analysis of the correlation of both MCT and AL intensities with both LLJs humidity transports, showed that AL and MCT have more impact on Zambezi LLJ than on Limpopo LLJ, as ZRV LLJ presents a better IVT_u correlation value than LRV LLJ. The results also showed that a weaker MCT and AL are linked with a stronger ZRV LLJ and, consequently, with higher precipitation values over the region of interest (and vice-versa). The same analysis performed with LRV LLJ was not conclusive, as it was not possible to establish a good correlation between both AL and MCT intensities and Limpopo LLJ IVT_u. Hence, the comparative analysis on both LLJs concluded that Zambezi LLJ is more relevant for humidity transport towards SW Africa (and consequent rainfalls), than Limpopo LLJ.

This work also demonstrated the impact of large-scale modes of variability on interannual precipitation anomalies. Essentially, 2 modes of variability control the subcontinent rainfall variability: El-Niño Southern Oscillation (ENSO) and Subtropical Indian Ocean Dipole (SIOD). It was verified that El-Niño (La-Niña) phases of ENSO were associated with stronger (weaker) AL phases and northward (southward) shifts of this system, bringing drier (wetter) spells over the subcontinent. For SW Africa, when La-Niña phase was active, positive (negative) signals of SIOD index were linked with wet (dry) spells over the region, even though with limited statistical significance. Nonetheless, it was concluded that SW Africa regions are placed in a kind of *border zone* between drier and wetter regimes originated by both large-scale variability modes, enhancing the vulnerability of the region to this type of weather patterns' oscillations. In addition, it is important to highlight that AL meridional position is also a key feature on rainfall variability, as northward AL shifts allow more moisture to be advected towards the study-region than southward shifts.

In fact, an analysis performed on 2 extreme events occurred in SW Africa (associated with catastrophic economic and humanitarian consequences), showed that both exceptional events were originated by phase conjugations between AL and MCT regions that do not fit the circulation patterns identified in this thesis. It was discussed that large-scale modes of variability played a major role on both study-cases rainfall exceptionalities, but local circulation features perturbed the mean weather circulation pattern, enhancing catastrophic events across the subcontinent.

In the context of the FRESAN project activities, it became evident that more investment in scientific research across the region is needed, namely by installing weather stations and organizing field campaigns (e.g., to study vertical atmospheric profiles over both Zambezi and Limpopo river valleys), not only to understand regional dynamics of both LLJs, but also to comprehend their effects on rainfall across the subcontinent. The lack of WS (and, consequently, the inexistence of long timeseries of atmospheric data over the region) contributes to a significant lack of scientific knowledge about the weather dynamics of Southern Africa. FRESAN project and its associated missions to southern Angola are trying to compensate this lack of weather-recording instruments by installing and fixing existing WS across the country, but it is still not enough to provide an acceptable coverage of the entire subcontinent, whose precipitation variabilities play key roles on the agricultural-based economies of most of the sub-Saharan countries. Thus, a better understating on rainfall variability drivers and a development of efficient methods to improve rainfall forecasts over the region is one of the best ways to prepare these populations to hazardous agricultural seasons (either due to intense droughts or devastating floods). This way, Southern African countries might be able to predict and work on plans to mitigate the consequences of such calamities.

More research involving future multi-model climate scenarios is also recommended to understand the implications of the ongoing widespread global warming on precipitations across the region. It is crucial to comprehend changes on large-scale modes of variability (ENSO and SIOD), responsible for most of the AL and MCT variability, dynamics, and intensities (and consequent strength of both Zambezi and Limpopo LLJs), in order realize the impacts of mean global temperature increases in Southern African regional rainfalls.

5. References

Algarra, I., Eiras-Barca, J., Nieto, R., & Gimeno, L. (2019). Global climatology of nocturnal low-level jets and associated moisture sources and sinks. In *Atmospheric Research* (Vol. 229, pp. 39–59). Elsevier Ltd. https://doi.org/10.1016/j.atmosres.2019.06.016

Banda Gerald, A Brief Review of Independent, Dependent and One Sample t-test. (2018). International *Journal of Applied Mathematics and Theoretical Physics*. 4(2) 2, 50-54. doi: 10.11648/j.ijamtp.20180402.13

Barimalala, R., Blamey, R. C., Desbiolles, F., & Reason, C. J. C. (2019). Variability in the Mozambique Channel Trough and Impacts on Southeast African Rainfall. *American Meteorological Society*, *33*, 749–765. https://doi.org/10.1175/JCLI-D-19

Barimalala, R., Blamey, R. C., Desbiolles, F., & Reason, C. J. C. (2021). The influence of southeastern African river valley jets on regional rainfall. *Climate Dynamics*, *57*(9–10), 2905–2920. https://doi.org/10.1007/s00382-021-05846-1

Barimalala, R., Desbiolles, F., Blamey, R. C., & Reason, C. (2018). Madagascar Influence on the South Indian Ocean Convergence Zone, the Mozambique Channel Trough and Southern African Rainfall. *Geophysical Research Letters*, *45*(20), 11,380-11,389. https://doi.org/10.1029/2018GL079964

Barry, R., & Chorley, R. (2003). *Atmosphere, Weather and Climate* (Routledge, Vol. 8). Routledge.

Behera, S. K., & Yamagata, T. (2001). Subtropical SST dipole events in the southern Indian Ocean. *Geophysical Research Letters*, *28*(2), 327–330. https://doi.org/10.1029/2000GL011451

Blackadar, A. K. (1957). Boundary Layer Wind Maxima and Their Significance for the Growth of Nocturnal Inversions. *Bulletin of the American Meteorological Society*, 38(5), 283-290. https://doi.org/10.1175/1520-0477-38.5.283

Branca, G., Lipper, L., McCarthy, N., & Jolejole, M. C. (2013). Food security, climate change, and sustainable land management. A review. In *Agronomy for Sustainable Development*. 33(4). 635–650. https://doi.org/10.1007/s13593-013-0133-1

Burk, S. D., & Thompson, W. T. (1996). The Summertime Low-Level Jet and Marine Boundary Layer Structure along the California Coast. *Monthly Weather Review*, *124*(4), 668–686. https://doi.org/10.1175/1520-0493(1996)124<0668:TSLLJA>2.0.CO;2

Cain, A., Tiago, J., & Domingos, J. (2015). Climate-adaptive planning for Angola's coastal cities. *International Development Research Centre*.

Caldeirinha, A. (2017). *Coastal low-level jet and El Niño-like phenomenon at the Benguela coast*. Master Thesis. Faculdade de Ciências da Universidade de Lisboa. Lisboa.

Cimbala, J., & Çengel, Y. (2007). *Fluid Mechanics: Fundamentals and Applications, 1st edition* (Y. Canguel & J. Cimbala, Eds.). McGraw Hill.

Collins, M., R. Knutti, J. Arblaster, J.-L. Dufresne, T. Fichefet, P. Friedlingstein, X. Gao, W.J. Gutowski, T. Johns, G., Krinner, M. Shongwe, C. Tebaldi, A.J. Weaver and M. Wehner, 2013: Long-term Climate Change: Projections, Commitments and Irreversibility. In: Climate Change 2013: The Physical Science Basis. Contribution of Working Group I to the Fifth Assessment Report of the Intergovernmental Panel on Climate Change [Stocker, T.F., D. Qin, G.-K., Plattner,

M. Tignor, S.K. Allen, J. Boschung, A. Nauels, Y. Xia, V. Bex and P.M. Midgley (eds.)]. Cambridge University Press, Cambridge, United Kingdom and New York, NY, USA.

Cook, K. H. (2000). The South Indian Convergence Zone and Interannual Rainfall Variability over Southern Africa. *Journal of Climate*, *13*(21), 3789–3804. https://doi.org/10.1175/1520-0442(2000)013<3789:TSICZA>2.0.CO;2

Crétat, J., Pohl, B., Dieppois, B., Berthou, S., & Pergaud, J. (2019). The Angola Low: relationship with southern African rainfall and ENSO. *Climate Dynamics*, *52*(3–4), 1783–1803. https://doi.org/10.1007/s00382-018-4222-3

Desbiolles, F., Howard, E., Blamey, R. C., Barimalala, R., Hart, N. C. G., & Reason, C. J. C. (2020). Role of ocean mesoscale structures in shaping the Angola-Low pressure system and the southern Africa rainfall. *Climate Dynamics*, *54*(7–8), 3685–3704. https://doi.org/10.1007/s00382-020-05199-1

Douglas, M. W. (1995). The Summertime Low-Level Jet over the Gulf of California. *Monthly Weather Review*, *123*(8), 2334–2347. https://doi.org/10.1175/1520-0493(1995)123<2334:TSLLJO>2.0.CO;2

Garreaud, RenéD., & Muñoz, R. C. (2005). The Low-Level Jet off the West Coast of Subtropical South America: Structure and Variability. *Monthly Weather Review*, *133*(8), 2246–2261. https://doi.org/10.1175/MWR2972.1

Grobler, J. (2011). Namibia in flood after heaviest rain in 120 years. *Mali & Guardian*.

Guedes do Nascimento, M., Herdies, D. L., & Oliveira de Souza, D. (2016). The South American Water Balance: The Influence of Low-Level Jets. *Journal of Climate*, *29*(4), 1429–1449. https://doi.org/10.1175/JCLI-D-15-0065.1

Hart, N. C. G., Reason, C. J. C., & Fauchereau, N. (2013). Cloud bands over southern Africa: Seasonality, contribution to rainfall variability and modulation by the MJO. *Climate Dynamics*, *41*(5–6), 1199–1212. https://doi.org/10.1007/s00382-012-1589-4

Hersbach, H, Bell, B, Berrisford, P, et al. The ERA5 global reanalysis. *Q J R Meteorol Soc*. 2020; 146: 1999– 2049. https://doi.org/10.1002/qj.3803

Hoell, A., & Cheng, L. (2018). Austral summer Southern Africa precipitation extremes forced by the El Niño-Southern oscillation and the subtropical Indian Ocean dipole. *Climate Dynamics*, *50*(9–10), 3219–3236. https://doi.org/10.1007/s00382-017-3801-z

Holton, J. (2004). *An Introduction to Dynamic Meteorology, 4th edition*. Elsevier. https://doi.org/10.1016/C2009-0-63394-8

Howard, E., & Washington, R. (2018). Characterizing the Synoptic Expression of the Angola Low. *American Meteorological Society*, 7147–7165. https://doi.org/10.1175/JCLI-D-18

Howard, E., & Washington, R. (2019). Drylines in southern Africa: Rediscovering the Congo air boundary. *Journal of Climate*, *32*(23), 8223–8242. https://doi.org/10.1175/JCLI-D-19-0437.1

Huntley, B. J., Russo, V., Lages, F., & Ferrand, N. (2019). *Biodiversity of Angola* (Springer, Vol. 1). Springer Nature Switzerland AG.

Imbol Koungue, R. A., Rouault, M., Illig, S., Brandt, P., & Jouanno, J. (2019). Benguela Niños and Benguela Niñas in Forced Ocean Simulation From 1958 to 2015. *Journal of Geophysical Research: Oceans*, *124*(8), 5923–5951. https://doi.org/10.1029/2019JC015013

IPCC, 2021: Climate Change 2021: The Physical Science Basis. Contribution of Working Group I to the Sixth Assessment Report of the Intergovernmental Panel on Climate Change [Masson-Delmotte, V., P. Zhai, A. Pirani, S.L., Connors, C. Péan, S. Berger, N. Caud, Y. Chen, L. Goldfarb, M.I. Gomis, M. Huang, K. Leitzell, E. Lonnoy, J.B.R., Matthews, T.K. Maycock, T. Waterfield, O. Yelekçi, R. Yu, and B. Zhou (eds.)]. Cambridge University Press, Cambridge, United Kingdom and New York, NY, USA, In press, doi:10.1017/9781009157896.

Jaffrés, J. B. D., Cuff, C., Rasmussen, C., & Hesson, A. S. (2018). Teleconnection of atmospheric and oceanic climate anomalies with Australian weather patterns: a review of data availability. *Earth-Science Reviews*, *176*, 117–146. https://doi.org/10.1016/j.earscirev.2017.08.010

James, R., Hart, N. C. G., Munday, C., Reason, C. J. C., & Washington, R. (2020). Coupled Climate Model Simulation of Tropical–Extratropical Cloud Bands over Southern Africa. *Journal of Climate*, *33*(19), 8579–8602. https://doi.org/10.1175/JCLI-D-19-0731.1

Kim, T. K. (2015). T test as a parametric statistic. *Korean Journal of Anesthesiology*, *68*(6), 540. https://doi.org/10.4097/kjae.2015.68.6.540

Lima, D. (2019). *The Benguela Coastal Low-Level Jet in a Changing Climate*. PhD Thesis. Faculdade de Ciências da Universidade de Lisboa. Lisboa.

Lima, D. C. A., Soares, P. M. M., Semedo, A., Cardoso, R. M., Cabos, W., & Sein, D. v. (2019). A Climatological Analysis of the Benguela Coastal Low-Level Jet. *Journal of Geophysical Research: Atmospheres*, *124*(7), 3960–3978. https://doi.org/10.1029/2018JD028944

Limones, N., Marzo-Artigas, J., Wijnen, M., & Serrat-Capdevila, A. (2020). Evaluating drought risk in data-scarce contexts. The case of southern Angola. *Journal of Water and Climate Change*, *11*(S1), 44–67. https://doi.org/10.2166/wcc.2020.101

Liu, J., Hertel, T. W., Diffenbaugh, N. S., Delgado, M. S., & Ashfaq, M. (2015). Future property damage from flooding: sensitivities to economy and climate change. *Climatic Change*, *132*(4), 741–749. https://doi.org/10.1007/s10584-015-1478-z

Luetkemeier, R., Stein, L., Drees, L., Müller, H., & Liehr, S. (2018). Uncertainty of Rainfall Products: Impact on Modelling Household Nutrition from Rain-Fed Agriculture in Southern Africa. *Water*, *10*(4), 499. https://doi.org/10.3390/w10040499

Lyon, B., & Mason, S. J. (2007). The 1997–98 Summer Rainfall Season in Southern Africa. Part I: Observations. *Journal of Climate*, *20*(20), 5134–5148. https://doi.org/10.1175/JCLI4225.1

Macron, C., Pohl, B., Richard, Y., & Bessafi, M. (2014). How do Tropical Temperate Troughs Form and Develop over Southern Africa? *Journal of Climate*, *27*(4), 1633–1647. https://doi.org/10.1175/JCLI-D-13-00175.1

Masters, J. (2019). Africa's Hurricane Katrina: Tropical Cyclone Idai Causes an Extreme Catastrophe. *Weather Underground*.

Mawren, D., Hermes, J., & Reason, C. J. C. (2022). Marine heatwaves in the Mozambique Channel. *Climate Dynamics*, *58*(1–2), 305–327. https://doi.org/10.1007/s00382-021-05909-3

MEANS, L. L. (1952). ON THUNDERSTORM FORECASTING IN THE CENTRAL UNITED STATES. *Monthly Weather Review*, *80*(10), 165–189. https://doi.org/10.1175/1520-0493(1952)080<0165:OTFITC>2.0.CO;2

Miao, Y., Guo, J., Liu, S., Wei, W., Zhang, G., Lin, Y., & Zhai, P. (2018). The Climatology of Low-Level Jet in Beijing and Guangzhou, China. *Journal of Geophysical Research: Atmospheres*, *123*(5), 2816–2830. https://doi.org/10.1002/2017JD027321

Mulenga, H., Rouault, M., & Reason, C. (2003). Dry summers over northeastern South Africa and associated circulation anomalies. *Climate Research*, *25*, 29–41. https://doi.org/10.3354/cr025029

Munday, C., & Washington, R. (2017). Circulation controls on southern African precipitation in coupled models: The role of the Angola Low. *Journal of Geophysical Research*, *122*(2), 861–877. https://doi.org/10.1002/2016JD025736

Munday, C., & Washington, R. (2019). Controls on the diversity in climate model projections of early summer drying over southern Africa. *Journal of Climate*, *32*(12), 3707–3725. https://doi.org/10.1175/JCLI-D-18-0463.1

Munday, C., Washington, R., & Hart, N. (2021). African Low-Level Jets and Their Importance for Water Vapor Transport and Rainfall. *Geophysical Research Letters*, *48*(1). https://doi.org/10.1029/2020GL090999

Oliveira, M. I., Nascimento, E. L., & Kannenberg, C. (2018). A New Look at the Identification of Low-Level Jets in South America. *Monthly Weather Review*, *146*(7), 2315–2334. https://doi.org/10.1175/MWR-D-17-0237.1

Pascale, S., Pohl, B., Kapnick, S. B., & Zhang, H. (2019). On the Angola Low Interannual Variability and Its Role in Modulating ENSO Effects in Southern Africa. *American Meteorological Society*, *32*, 4783–4802. https://doi.org/10.1175/JCLI-D-18

Patricola, C. M., & Chang, P. (2017). Structure and dynamics of the Benguela low-level coastal jet. *Climate Dynamics*, *49*(7–8), 2765–2788. https://doi.org/10.1007/s00382-016-3479-7

Payne, A. E., Demory, M.-E., Leung, L. R., Ramos, A. M., Shields, C. A., Rutz, J. J., Siler, N., Villarini, G., Hall, A., & Ralph, F. M. (2020). Responses and impacts of atmospheric rivers to climate change. *Nature Reviews Earth & Environment*, *1*(3), 143–157. https://doi.org/10.1038/s43017-020-0030-5

Peel, M. C., Finlayson, B. L., & McMahon, T. A. (2007). Updated world map of the Köppen-Geiger climate classification. *Hydrology and Earth System Sciences*, *11*(5), 1633–1644. https://doi.org/10.5194/hess-11-1633-2007

Posada, R., Nascimento, D., Neto, F. O. S., Riede, J., & Kaspar, F. (2016). Improving the climate data management in the meteorological service of Angola: experience from SASSCAL. *Advances in Science and Research*, *13*, 97–105. https://doi.org/10.5194/asr-13-97-2016

Ramos, A. M., Blamey, R. C., Algarra, I., Nieto, R., Gimeno, L., Tomé, R., Reason, C. J. C., & Trigo, R. M. (2019). From Amazonia to southern Africa: atmospheric moisture transport through low-level jets and atmospheric rivers. *Annals of the New York Academy of Sciences*, *1436*(1), 217–230. https://doi.org/10.1111/nyas.13960

Ramos, A. M., Tomé, R., Trigo, R. M., Liberato, M. L. R., & Pinto, J. G. (2016). Projected changes in atmospheric rivers affecting Europe in CMIP5 models. *Geophysical Research Letters*, *43*(17), 9315–9323. https://doi.org/10.1002/2016GL070634

Ranjha, R., Svensson, G., Tjernström, M., & Semedo, A. (2013). Global distribution and seasonal variability of coastal low-level jets derived from ERA-Interim reanalysis. *Tellus A: Dynamic Meteorology and Oceanography*, *65*(1), 20412. https://doi.org/10.3402/tellusa.v65i0.20412

Ranjha, R., Tjernström, M., Semedo, A., Svensson, G., & Cardoso, R. M. (2015). Structure and variability of the Oman coastal low-level jet. *Tellus A: Dynamic Meteorology and Oceanography*, *67*(1), 25285. https://doi.org/10.3402/tellusa.v67.25285

Rapolaki, R. S., Blamey, R. C., Hermes, J. C., & Reason, C. J. C. (2020). Moisture sources associated with heavy rainfall over the Limpopo River Basin, southern Africa. *Climate Dynamics*, *55*(5–6), 1473–1487. https://doi.org/10.1007/s00382-020-05336-w

Reason, C. J. C. (1996). Topography and the dynamical response to easterly flow in Southern Hemisphere subtropical West Coast regions. *Meteorology and Atmospheric Physics*, *61*(3–4), 187–199. https://doi.org/10.1007/BF01025704

Reason, C. J. C. (2002). ENSO-like decadal variability and South African rainfall. *Geophysical Research Letters*, *29*(13), 1638. https://doi.org/10.1029/2002GL014663

Reason, C. J. C., & Smart, S. (2015). Tropical south east Atlantic warm events and associated rainfall anomalies over Southern Africa. *Frontiers in Environmental Science*, *3*(MAY). https://doi.org/10.3389/fenvs.2015.00024

Richter, I. (2004). Orographic influences on the annual cycle of Namibian stratocumulus clouds. *Geophysical Research Letters*, *31*(24), L24108. https://doi.org/10.1029/2004GL020814

Rijo, N., Semedo, A., Miranda, P. M. A., Lima, D., Cardoso, R. M., & Soares, P. M. M. (2018). Spatial and temporal variability of the Iberian Peninsula coastal low-level jet. *International Journal of Climatology*, *38*(4), 1605–1622. https://doi.org/10.1002/joc.5303

Rouault, M., Florenchie, P., Fauchereau, N., & Reason, C. J. C. (2003). South East tropical Atlantic warm events and southern African rainfall. *Geophysical Research Letters*, *30*(5). https://doi.org/10.1029/2002GL014840

Sáenz, F., & Durán-Quesada, A. M. (2015). A climatology of low level wind regimes over Central America using a weather type classification approach. *Frontiers in Earth Science*, *3*. https://doi.org/10.3389/feart.2015.00015

Sarr, B. (2012). Present and future climate change in the semi-arid region of West Africa: A crucial input for practical adaptation in agriculture. *Atmospheric Science Letters*, *13*(2), 108–112. https://doi.org/10.1002/asl.368

Schneider, T., Bischoff, T., & Haug, G. H. (2014). Migrations and dynamics of the intertropical convergence zone. *Nature*, 513(7516), 45–53. https://doi.org/10.1038/nature13636

Senior, C. A., Marsham, J. H., Berthou, S., Burgin, L. E., Folwell, S. S., Kendon, E. J., Klein, C. M., Jones, R. G., Mittal, N., Rowell, D. P., Tomassini, L., Vischel, T., Becker, B., Birch, C. E., Crook, J., Dougill, A. J., Finney, D. L., Graham, R. J., Hart, N. C. G., … Willet, M. R. (2021). Convection-permitting regional climate change simulations for understanding future climate and informing

decision-making in Africa. *Bulletin of the American Meteorological Society*, *102*(6), E1206–E1223. https://doi.org/10.1175/BAMS-D-20-0020.1

Soares, P. M. M., Lima, D. C. A., Cardoso, R. M., & Semedo, A. (2017). High resolution projections for the western Iberian coastal low level jet in a changing climate. *Climate Dynamics*, *49*(5–6), 1547–1566. https://doi.org/10.1007/s00382-016-3397-8

Spavins-Hicks, Z. D., Washington, R., & Munday, C. (2021). The Limpopo Low-Level Jet: Mean Climatology and Role in Water Vapor Transport. *Journal of Geophysical Research: Atmospheres*, *126*(16). https://doi.org/10.1029/2020JD034364

Stull, R. (1988). *An Introduction to Boundary Layer Meteorology* (Vol. 1). Kluwer Academic Publishers.

Sultan, B., & Gaetani, M. (2016). Agriculture in West Africa in the twenty-first century: Climate change and impacts scenarios, and potential for adaptation. In *Frontiers in Plant Science* (Vol. 7, Issue AUG2016). Frontiers Media S.A. https://doi.org/10.3389/fpls.2016.01262

Thoithi, W., Blamey, R. C., & Reason, C. J. C. (2021). Dry Spells, Wet Days, and Their Trends Across Southern Africa During the Summer Rainy Season. *Geophysical Research Letters*, *48*(5). https://doi.org/10.1029/2020GL091041

Trenberth, K. E. (1997). The Definition of El Niño. *Bulletin of the American Meteorological Society* 78, 12, 2771-2778. https://doi.org/10.1175/1520-0477(1997)078<2771:TDOENO>2.0.CO;2>

Tyson, P. D., & Crimp, S. J. (1998). THE CLIMATE OF THE KALAHARI TRANSECT. *Transactions of the Royal Society of South Africa*, *53*(2), 93–112. https://doi.org/10.1080/00359199809520380

Vieira, A. (2011). Chuvas deixam 255 famílias desalojadas na capital da província angolana do Cunene. *Lusa*.

Wheeler, T., & von Braun, J. (2013). Climate Change Impacts on Global Food Security. *Science*, *341*(6145), 508–513. https://doi.org/10.1126/science.1239402

Wilks, D. S. (1995). Chapter 5 hypothesis testing. In *International Geophysics*: Vol. 59. Statistical methods in the atmospheric sciences (pp. 114e158). Academic Press.

6. Appendix

6.1. Precipitation values of hydrological years since 1980/81

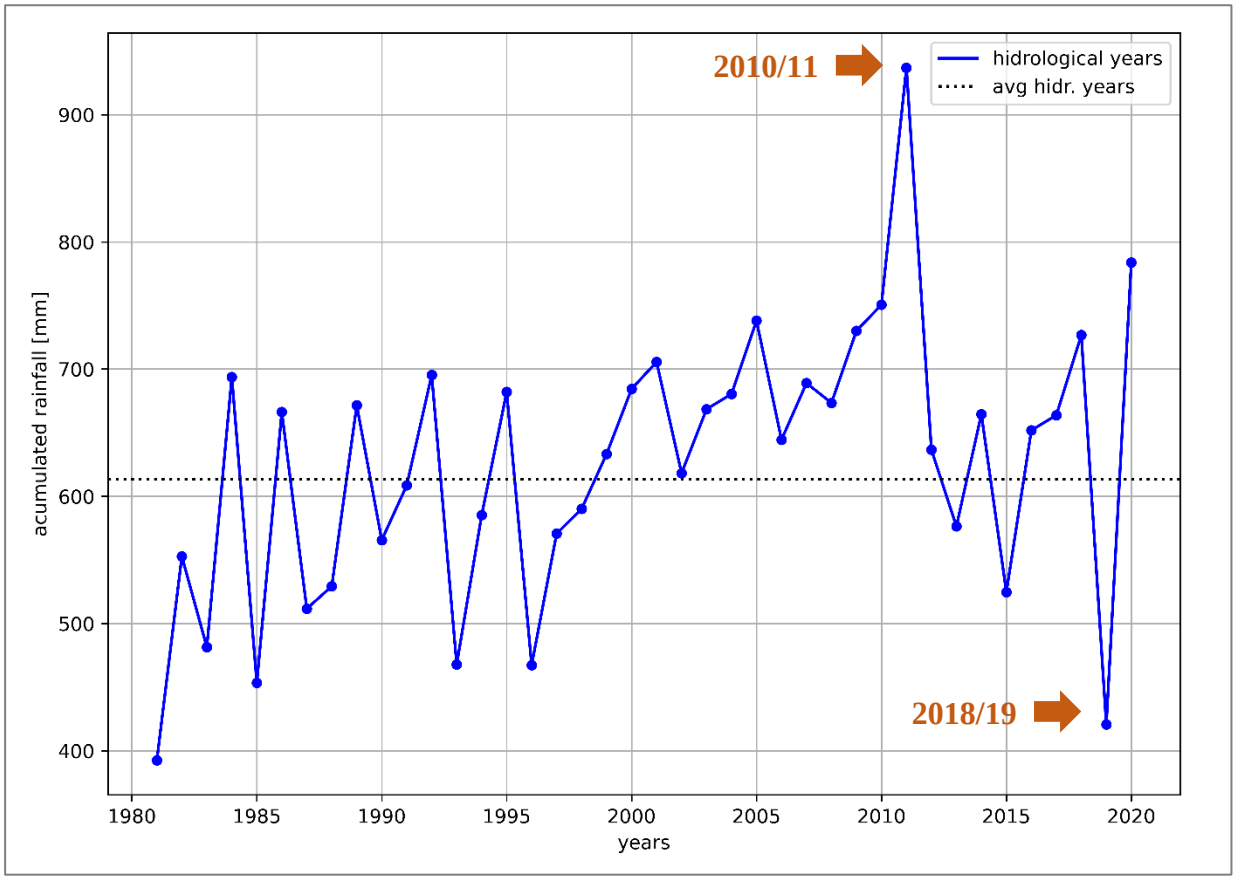

Figure 6.1 – Timeseries of accumulated precipitation (from ERA5), for every hydrological year, since 1980/81 (blue line). A hydrological year was defined as starting in each October 1st of the previous year and ending on September 30th of the actual year (e.g., in 1990/91 season, the hydrological year started in October 1st 1990 and ended in September 30th 1991). Rainfall data was retrieved for the area of interest (dark-red square in Figure 2.3). Dotted black line indicates the average value (1980-2010) of accumulated precipitation. Orange arrows corresponds to case-study years, analysed in subsection 3.5 of this thesis.

6.2. Geopotential height intensities: Mozambique Channel Trough vs. the Angola Low

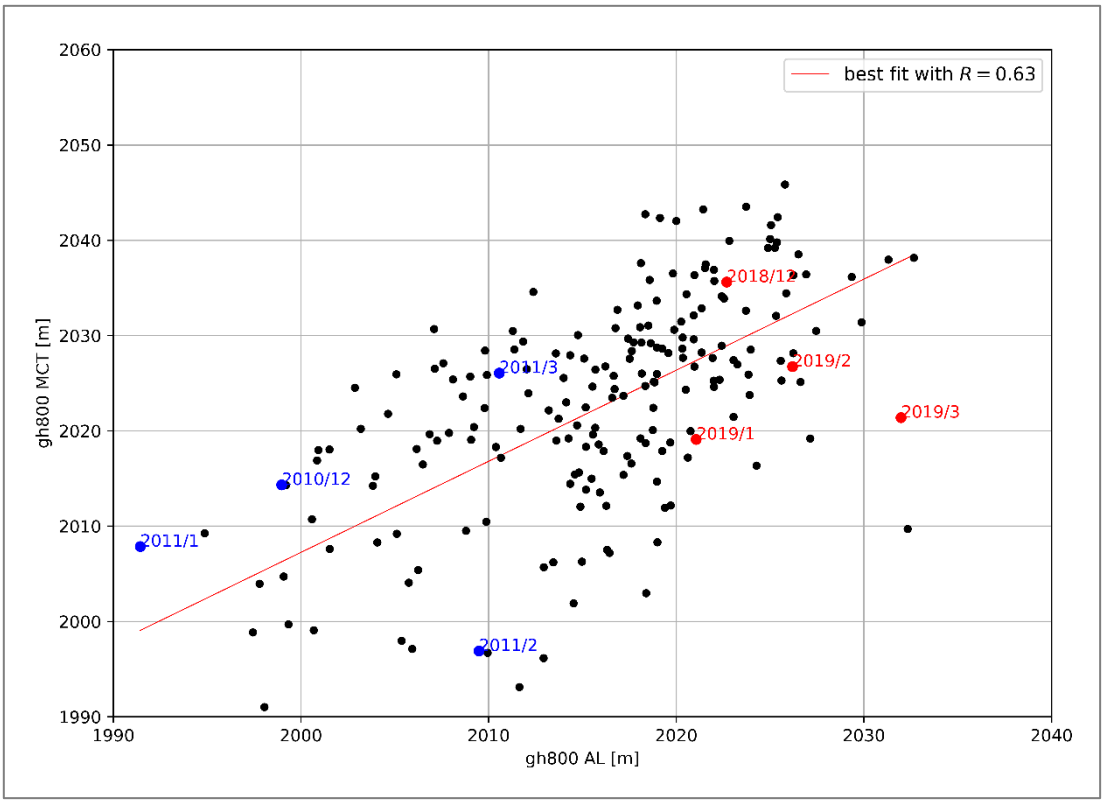

Figure 6.2 – Similar description to Figure 3.9. Red dots correspond to the exceptionally dry rainy season of 2018/19, analysed in subsection 3.5.1. Blue dots are related with the abnormally wet rainy season of 2010/11, studied in subsection 3.5.2.

6.3. Photographic records of FRESAN missions across southern Angola

Figure 6.3 – Panoramic view of a meeting between FRESAN team and native populations of Onkokwa (south of Angola). This meeting took place in a "meeting room" named *Jambo*. These local communities are part of a predominant southwestern Africa ethnic group named *Hereros*. The tribe shown in the picture is named *Macahones* (a subgroup of *Herero* ethnicity). Photo taken by the author, in April 2022.

Figure 6.4 – Picture of a meeting between FRESAN team and *Macahones* tribe (similar to Figure 6.3), but in an experimental agricultural field located in Onkokwa (southern Angola). Photo taken by the author, in April 2022.

Figure 6.5 – Picture of Huíla plateau's big cliffs (where altitudes reach ~2000[m]). Orographic-induced cumulus and cumulonimbus clouds above the plateau are depicted, which are responsible for significant rainfalls over this region, essentially in the rainy season. This image was taken in a West-to-East perspective (i.e., the mountain range is in the East, and, behind this perspective, there is the arid Namib desert and the Atlantic Ocean, where these stormy-cloud developments do not occur). Location: Namibe (southern Angola). Photo taken by the author, in April 2022.

Figure 6.6 – Similar description as Figure 6.5. This picture shows a better perspective of the aridity and dominance of clear skies over the desert region, contrasting with the cumulonimbus clouds development down in the mountains placed in the background. This photo was taken in the Namib desert, on the way to the mountains (temperate and rainier region). Location: Namibe (southern Angola). Photo taken by the author, in April 2022.

Figure 6.7 – Weather station located in the Namib desert, near the village of Tombwa, in Angola. This WS was installed and is managed by the FRESAN team. Photo taken by the author, in April 2022.